A STUDY OF NON-ADIABATIC BAROCLINIC INSTABILITY

by

MAURIZIO FANTINI

SUBMITTED TO THE DEPARTMENT OF
EARTH ATMOSPHERIC AND PLANETARY SCIENCES
IN PARTIAL FULFILLMENT OF THE REQUIREMENTS
FOR THE DEGREE OF

DOCTOR OF PHILOSOPHY IN METEOROLOGY

at the

MASSACHUSETTS INSTITUTE OF TECHNOLOGY

September 1988

© Massachusetts Institute of Technology 1988

Signature of Author_____
Dept. of Earth, Atmospheric and Planetary Sciences

Certified by_____
Kerry A. Emanuel - Thesis Supervisor

Accepted by_____
Thomas H. Jordan - Chairman
Departmental Committee on Graduate Students

WITHDRAWN FROM MIT LIBRARIES

A STUDY OF NON-ADIABATIC BAROCLINIC INSTABILITY

by

Maurizio Fantini

Submitted to the Department of Earth Atmospheric and Planetary Sciences

in partial fulfillment of the requirements for the degree of

Doctor of Philosophy in Meteorology

ABSTRACT

Observations of explosively deepening oceanic cyclones show the coincidence of an essentially baroclinic structure, deep convective activity and associated latent heat release, and air-sea exchanges of sensible and latent heat. In order to establish the role of these effects in a possible explanation of the unusual features of those storms a study is performed of the normal modes of non-adiabatic baroclinic instability.

The effect of convection alone is considered first, by assuming that a slantwise convective adjustment takes place on a short time scale so as to 'prepare' a moist symmetrically neutral environment for growing baroclinic waves. A hierarchy of two-dimensional models that incorporate this assumption (i.e. a base state of zero equivalent potential vorticity) is then used: a two-level semi-geostrophic, and a two-level primitive equations model are solved analytically and a multi-level non-hydrostatic PE numerical model is integrated in time to examine the structure of the unstable perturbations to an Eady-like base state. An increase in growth rate of about 70% (in the more realistic model) is found, with a most unstable wavelength about half that of the dry case, and composed of a strong narrow updraft and a large weak downdraft. Another important aspect of the solutions is that frontal collapse occurs only at the surface and not at both top and bottom boundaries as it is usual in dry models.

The increase in growth rate is not sufficient, however, to explain explosive cyclones and sensible and latent heat fluxes from the bottom boundary are then added to the models. For the 2-level this is done with a linearized drag law for equivalent potential temperature, in which the flux is proportional to an air-sea entropy difference in the base state and to the perturbation meridional velocity. This is applied to the updraft region only, under the assumption that only there will the heat be transported effectively outside the boundary layer. The results show a further increase of the growth rate, linearly proportional to the air-sea temperature difference, but the drastic simplifications involved in the formulation of the model leave uncertainties as to the uniqueness of the solution.

The numerical model is run with heat and moisture fluxes and momentum drag at the surface. In a realistic range of parameters the most favorable cases reach a deepening rate of the surface low-pressure center of 24 mb in 24 hrs, which is the conventional threshold for explosive cyclones. The evolution often begins with a shallow hurricane-like structure that gives way to a deep baroclinic mode after several hours (i.e. 10-20 hrs). The thermal structure in the presence of heating from the bottom boundary displays a narrow warm core that expands as the storm intensifies. The phase speed of the disturbance is reduced as the shallow early state is advected by the low-level wind and tends to stabilize when the 'moist baroclinic' mode takes over.

Some limitations related to the two-dimensionality of the models used here need to be removed in the future, but it seems possible to conclude that the most striking features of explosive cyclones can be attributed to the presence of surface fluxes of sensible and latent heat, redistributed upward by moist convective activity.

Thesis supervisor: Kerry A. Emanuel

Title: Professor of Meteorology

ACKNOWLEDGMENTS

I am grateful to my advisor Kerry Emanuel for his constant interest in this work. Rich Rotunno, of NCAR, provided the numerical model. I was supported through my graduate studies by grants NSF/g 82-14582 ATM, AF/ESD F19628-86-K-0001 and ONR/c N00014-87-K-0291. The numerical experiments were performed on the CRAY-X/MP at NCAR. I also wish to thank Diana Spiegel for help with the CMPO computer and Jane McNabb for running the department.

Ben sai come nell'aere si raccoglie
quell'umido vapor, che in acqua riede
tosto che sale dove il freddo il coglie

Purgatorio,V,109-111

Table of Contents

Abstract ...pag.2

Acknowledgments ...pag.4

Table of contents ...pag.6

1. Introduction

1.1 Observational background ...pag.7

1.2 Theoretical background ...pag.15

2.Baroclinic instability in a saturated environment

2.1 A 2-level semi-geostophic model ...pag.21

2.2 A 2-level primitive-equation model ...pag.50

2.3 A primitive-equation numerical model ...pag.63

Appendixes to chapter 2

2.A Matching conditions for the linearized system ...pag.98

2.B Proof that σ^2 is real for the 2L SG model ...pag.100

2.C QG and GM non-dimensional quantities ...pag.101

2.D σ^2 for the 2L PE model ...pag.102

3. Air-sea interaction

3.1 A 2-level semi-geostophic model ...pag.104

3.2 A primitive-equation numerical model ...pag.119

4. Conclusion ...pag.151

Bibliography ...pag.156

List of figures ...pag.165

List of tables ...pag.171

1.1

The role of heat sources in the atmosphere has traditionally been considered significant but not dominant in the development of extratropical cyclones. The Norwegian cyclone model (J.Bjerknes,1919 etc.) and the classical theory of baroclinic instability (Charney,1947;Eady,1949) emphasized the conversion of planetary scale gravitational potential energy into cyclone scale energy by adiabatic processes alone. Non-adiabatic effects are obviously responsible for the mean meridional temperature gradient (differential solar heating) that drives the general circulation, and for small-scale convective systems (latent heat release), so that their influence on mid-latitude synoptic scale motions is a natural subject of investigation.

The release of latent heat of condensation was first recognized in early numerical models as crucial for a correct computation of vertical velocities (Smagorinsky,1956) and vorticity and pressure fields (Manabe,1956) and has been since then the subject of diagnostic studies of observed or numerically simulated cyclones, beginning with Aubert,1957 and Danard,1964. Comparision of moist and dry-adiabatic runs of Global Circulation Models (Manabe et al., 1965; Gall,1976) have shown, among other features, a tendency of 'moist' cyclones to develop faster and with a shorter horizontal scale.

For storms that develop in a maritime environment another likely source is the flux of heat from the lower boundary. After examination of several cases of North Atlantic cyclones at different stages of

evolution Pettersen et al.,1962 conclude that the inclusion of heat fluxes and release of latent heat 'led to improvement' of the computed tendencies and state:

> "It is evident, therefore, that the effect of heat sources and sinks on cyclone development are essentially complex and need not be small. In the absence of direct information it has been customary to assume that the effects of heat and cold sources are unimportant except in regard to changes over extended periods of time. Though this is true for the general circulation of the atmosphere, it need not be so for individual systems" (pag.261)

In this and later works (Pettersen and Smebye,1971) two distinct types of cyclones were identified. A Type A (predominantly maritime) in which the development is initiated in a highly baroclinic zone at low levels, with little or no vorticity advection aloft; and a Type B (prevalent over the North American continent) in which low-level cyclogenesis is induced by a strong pre-existing vorticity center in the upper troposphere. By geographic location and mode of initiation Type A is obviously more sensitive to fluxes of heat and humidity from the lower boundary in the early stages, and subsequent release of latent heat by synoptic or convective scale updrafts. On the other hand Tracton,1973 identified the outbreak of convection near the low center as an alternative initiator of the development also for cyclones over the continental U.S., east of the Rocky Mountains, in the presence of moist low-level air from the Gulf of Mexico.

A parallel line of investigation has identified a different class of marine cyclones that are characterized by small horizontal scale, rapid growth, 'warm core' thermal structure, and active presence of

non-adiabatic processes - latent heat release and sensible and latent heat fluxes from the lower boundary, that are prevalent during the explosive phase of growth. The first detailed description of such an event is probably that of Winston,1955, relative to a cyclone that occurred in the Gulf of Alaska in February 1950. The explosive deepening coincided with an outbreak of extremely cold air over the ocean. Diagnostic calculations show the vertical velocities obtained in the assumption of adiabatic motion to be largely in error (including the wrong sign at the time of maximum growth) and the heating of low-level air to be an order of magnitude larger than the climatological average. Although this paper mentions only sensible heat as the source, a later study (Pyke,1965) reveals the latent heat fluxes to be at least of the same magnitude. Cyclones of this family, that occur at high latitudes, north of the main baroclinic zone, often near the ice edge, are termed 'polar lows' and often compared to tropical cyclones for the importance that non-adiabatic processes have in their development. Some works on polar lows have identified an essentially baroclinic structure in the mature stage (Harrold and Browning,1969; Mansfield,1974; Reed,1979) while others chose to emphasize the hurricane-like features (Rasmussen,1979). A combination of the two is generally agreed upon, because the 'pure' mechanisms, dry-baroclinic or moist processes with no baroclinity, are certainly unable to explain all of the observed features. A recent review is given in Rasmussen and Lystad,1987.

In contrast to the often insignificant baroclinicity present in the environment at the early stages of development of polar lows, mid-latitude events on a small spatial and short temporal scale are observed to develop in strong baroclinic zones, e.g. the 'Baiu' front near Japan (Matsumoto et al.,1970). Nitta and Ogura,1972 summarize the observed features:

> "... warm-core type structure in the upper portion of the cyclone ... The particular features of these intermediate-scale cyclones in general, aside from their smallness in size, are that these disturbances do not appear to be associated with an upper tropospheric trough and their kinetic energy is confined to the lower portions of the troposphere ... In many cases a low-level jet is observed (at a level around 700 mb), the air in the lower troposphere is moist, the thermal stratification is less stable, and heavy rainfall takes place ... The characteristic time scale is short compared to that of a baroclinic wave. These cyclones also appear quite suddenly and are stationary or move slowly. When an upper trough approaches, these cyclones often appear to interact with it and develop into mature extratropical cyclones."(pag. 1011,1012)

They attempt a numerical simulation with a moist model that allows evaporation from the sea surface and in fact reproduces some of the observed characteristics, including the small size and the warm core, and the evolution into a more clearly baroclinic structure in the mature stage. A 'dry' run of the model appears unable to maintain the 'intermediate scale' cyclone.

The first systematic study of explosive cyclones is to be found in Sanders and Gyakum,1980. A cut-off criterion was established - the central pressure at low level falling by at least 1 mb per hour for 24 hrs at 60 N. Since the time and space scales of baroclinic instability are known to be proportional to f , this effect was eliminated by

allowing the cut-off deepening rate to vary with the sine of latitude - in other words the selection was made in terms of relative vorticity normalized with the local value of planetary vorticity. They found, among other results, that most of the deepest cyclones that occur in middle latitudes deepen explosively. They are predominantly maritime, cold season events, with hurricane-like features in the wind and cloud fields. The geographic areas of most frequent occurrence are the western Atlantic and Pacific Oceans, in association with the warm currents of the Gulf Stream and the Kuroshio. The maximum frequency actually occurs at the northern edge of these currents, where the SST gradient is maximum, but this correlation is believed not to be critical for the phenomenon since another relative maximum of frequency occurs in the northeastern Pacific where it can be associated with a flow of polar air over warmer waters, but where the SST is almost uniform. The authors conclude that

> "The circumstances point to the importance of both large-scale horizontal temperature contrasts and transfer of latent and sensible heat from the winter ocean into relatively cold air... Explosive cyclones seem likely to be mainly baroclinic events, strongly, and perhaps crucially, aided by diabatic heating."(pag. 1595)

This conclusion is confirmed in successive works, at least for the explosive events that occur off the East coast of the U.S., for which both detailed individual case studies (Bosart,1981; Gyakum,1983a,b) and average properties over a significant number of cases (Sanders,1986) are available. The phase of explosive growth is always associated with a vorticity maximum at 500 mb, which is often independent of the surface low in the early stages of development and comes to interact

with it at the beginning of the explosive growth (Sanders,1986). The position of the upper-level trough is consistent with deepening baroclinic waves, and positive vorticity advection at 500 mb is highly correlated with the simultaneous rate of deepening (Sanders,1986). Numerical simulations of one of these storms (Anthes et al.,1983) have shown that baroclinic instability was the primary mechanism of early intensification but that latent heating played a greater role in enhancing the development at later stages.

A further statistical study (Roebber,1984) examines the maximum 24-hrs deepening rates of all Northern Hemisphere mid-latitude cyclones during one year and shows deviations from a normal distribution at the largest values, beginning with a deepening rate that, when normalized as in Sanders and Gyakum,1980, is of the order of 1 mb per hour, thus supporting the choice of the cut-off value of Sanders and Gyakum,1980 and the conclusion that a physical mechanism different from ordinary baroclinic instability is at work.

Several mechanisms have been suggested that may enhance the development of oceanic cyclones:

> The release of latent heat by large-scale motion generates stronger vertical velocities, reinforces the convergence-divergence pattern and therefore the generation of vorticity by the vortex stretching mechanism.

Cumulus convection may activate a self-sustaining large scale circulation by means of a CISK mechanism.

Surface heating may act to increase baroclinicity and reduce static stability in the lower troposphere, thus accounting for a stronger growth rate of baroclinic disturbances.

The effective static stability of upward saturated motions is given by the gradient of equivalent potential temperature, which is always less than the 'dry' static stability.

Replenishment of moisture from the ocean may feed any of the above mechanisms.

The relative smoothness of the sea surface compared to land surface reduces the frictional dissipation of kinetic energy.

More recent diagnostic studies (Reed and Albright,1986; Chang et al.,1987; Liou and Elsberry,1987; Wash at al.,1988) depict other individual cases in which the different ingredients (large-scale baroclinic forcing, high low-level baroclinicity, low static stability, latent heat release, heat fluxes from the sea) are all present but their relative importance and time of appearance vary. As already noted for the 'polar low' subset of explosive cyclones no single 'pure' mechanism can account for all of the observed features. In much the same way the time evolution from early to mature stage seems to follow a path in which elements of both of Pettersen's type A and type B are present to a different degree.

In order to understand how much of the observed features of explosive oceanic cyclones are general and related to the stability properties of the environment, as opposed to a transient (but not necessarily insignificant from the point of view of the weather) behavior due to the peculiar initial state of each individual case it seems necessary to identify the 'normal modes' of an atmosphere that is baroclinically unstable and, at the same time, is subject to non-adiabatic influences. Of the above-listed mechanisms we will consider only the effects of release of latent heat, which may be active for ordinary land cyclones as well, and the air-sea exchange of sensible and latent heat. This is done in Chapters 2 and 3 respectively. In view of the observational evidence we mainly look for a higher growth rate than dry baroclinic instability, smaller horizontal scale, 'warm core' thermal structure, and alterations in the phase speed of the wave. The way we approach the problem of the representation of the effects of condensation of water vapor on the large-scale flow in a simple analytic model is explained in the next section. A full explanation of the phenomenon we consider, including the role of the interaction with a pre-existing mid-tropospheric high vorticity center, would require the study of an initial value problem - this is not within the scope of this investigation. We use a numerical model, in Chapters 2 and 3, only for the purpose of examining the normal modes of the system in a less approximate context.

1.2

Attempts at a theoretical explanation of sub-synoptic scale, fast growing cyclones have included either 'dry' or 'moist' models. The 'dry' models included non-geostrophic baroclinic instability (uniformly small Richardson number), for possible application to the disturbances on the 'Baiu' front (e.g.,Tokioka,1970), where high wind shear and low static stability are observed, or to 'frontal waves' in general (Orlanski,1968), but they were mostly indirect representations of the effects of surface heating through reduced low-level static stability. Staley and Gall,1977 used a 4-level quasi-geostrophic model to show that baroclinic waves are only weakly affected by changes of static stability or vertical shear in the middle and upper troposphere, but that such modifications in the lower troposphere produce instead a destabilisation of the short waves. These are shallow modes, with the amplitudes of both the geopotential and the temperature perturbation maximum at the surface and rapidly decreasing with height. This explains their sensitivity to low-level environmental parameters, and the inability of either the two-level models (Phillips,1951; Pedlosky,1964) or the continuous models with simple wind and temperature profiles (Charney,1947; Eady,1949; Green,1960) to adequately represent their behavior. In Staley and Gall's model the most unstable wavelength becomes shorter and its growth rate modestly higher when the low-level static stability is reduced. This mechanism can be useful for the early 'shallow low' phase of the phenomenon mentioned in the previous section, but it seems inadequate to describe

the explosive phase of growth. Similar results are obtained by Blumen,1981 in a two-layer model with different depth of the two layers and different static stability in each, extended by Hyun,1981 to include differences in both lapse rate and shear between the two layers ; and by Satyamurty et al.,1982 in a high vertical resolution, two dimensional primitive equation model with 'curved' wind profiles (i.e. non uniform shear).

The latter study also considered an explicit heating effect by including a representation of latent heat release via a wave-CISK mechanism and concludes that low-level heating is also capable of generating instability in the sub-synoptic scales. This treatment belongs to the 'moist' line of models seemingly initiated by Nitta,1964 (with reference to an unpublished work by Ooyama and to Charney and Eliassen,1964 for the representation of condensational heating as proportional to the frictionally induced vertical velocity at the top of the boundary layer). The CISK models have been proposed in various forms (Mak,1982; Sardie and Warner,1983; Wang and Barcilon,1986) and they generally conclude that the increase in maximum growth rate is not large enough to account for the explosive growth. Wang and Barcilon,1986 point out however that:

> "besides the destabilisation of increased moisture content, there are a number of favorable factors for rapid development of the disturbances, such as reduced static stability, increased vertical shear, higher latitude, shallower convection, and deeper moist convergence layer with its top above cloud base... The cooperative interaction between favorable factors listed earlier may create large growth which substantially exceeds the linear combination of their individual effects."(pag. 716)

Orlanski,1986 uses a numerical model to study the development of meso-alpha cyclones and shows that localized (sensible) surface heating can produce a more intense development of short baroclinic waves. He suggests that the weak stability of the moist atmosphere and release of latent heat are the primary causes for the explosive growth but the instability of the dry, pre-storm environment can be responsible for the scale selection and position of the storm. He proposes a mechanism for the rapid development of winter storms over ocean surfaces as follows:

> "With the passage of a cold front or a land-sea contrast, cold air can be advected over the rather warm ocean surface; the heat fluxes from the ocean will then rapidly reduce the static stability of the atmosphere in the first kilometer, increasing the baroclinicity and thereby allowing meso-baroclinic waves to develop. These waves are shallow, having a depth of the boundary layer and horizontal scales of a few hundred kilometers. They can organize convergence of surface moisture in those scales. With this addition of moisture, the wave will explosively develop into an intense meso-alpha cyclone."(pag. 2882)

Lastly, Weng and Barcilon,1987 shift the attention back to 'dry' models by including sensible heating and Ekman dissipation into Blumen's (1979) two-layer model and conclude that explosive cyclogenesis occurs in a complex environment in which many conditions must be met.

All the models that we labeled 'moist', above, are based on a CISK hypothesis, that is they assume that in a conditionally unstable environment the convective activity initiated by the large-scale flow (either through Ekman pumping or by the secondary circulation associated with the baroclinic wave itself) can have a 'collective' positive feed-back effect on the large-scale vorticity. The one exception is the work by Tang and Fichtl,1983: since the static stability for upward saturated motions

is given by the environmental lapse rate of equivalent potential temperature, and for downward motion by the 'dry' potential temperature, they treat separately the upward and downward branches of the secondary circulation of a baroclinic wave, using a different value of the stability parameter in each region. Then the effect of release of latent heat is represented by the use of a smaller static stability for upward compared to downward motion. The normal modes of the problem, which have to amplify at the same rate everywhere to be so called, have then a different wavelength in the two regions, and have to be matched at an intermediate point. This procedure is similar to the way we solve the problem in the following chapter, and some comments on the technical differences are made there. The physical approach is different, however. Tang and Fichtl,1983 consider a stable saturated atmosphere - no consideration is given to the effect of convection. Instead we assume that a convective adjustment has taken place, and continues to take place, whenever the atmosphere becomes conditionally unstable, on a time scale much faster than the synoptic motion, so as to 'prepare' a conditionally neutral environment for the large scale flow. On the basis of theoretical results on conditional symmetric instability (e.g. Bennetts and Hoskins,1979) and observational evidence from recent field experiments (Emanuel,1985a;1988) we assume that a slantwise convective adjustment occurs, i.e., after the lapse rate has been reduced to vertical neutrality (zero moist static stability) by upright convection, the atmosphere is still unstable to slantwise convection (along absolute angular momentum surfaces), which is then active until the equivalent potential vorticity (, which is the stability parameter for this form of instability) is reduced to zero. The value of

the 'vertical' static stability in the state of conditional symmetric neutrality is determined by other environmental factors, but it is anyhow positive. The features of the large-scale flow are determined by the 'dry' environmental parameters where there is downward motion, and by the 'moist' parameters, which include zero equivalent potential vorticity, in the updraft region. This assumption has been previously applied to the study of frontal circulations by Emanuel,1985b and Thorpe and Emanuel,1985, in association with the semi-geostophic equations, because of the role that potential vorticity plays in that approximation (see Hoskins,1975) and it is extended here (in sect.2.1) to the study of baroclinic instability. Suspicions of a breakdown of the approximation in the limit lead to reformulate the model from the primitive equations, in sect.2.2. The last section of chapter 2 presents simulations with a multi-level PE numerical model aimed at a more detailed look at the solutions found with the 2-level analytic models of sect.s 2.1 and 2.2.

As we noted in the previous section, there is a similarity between some of the observed features of mid-latitude explosive events and those of tropical cyclones. The role of air-sea exchanges of heat (especially latent heat) has been shown to be crucial for the intensification of tropical cyclones (e.g. Ooyama,1969), and even suggested (Emanuel,1986) to be their sole cause. A recent study (Davis and Emanuel,1988) finds a strong correlation between the potential for atmospheric heating due to air-sea temperature and moisture contrast and the amount of pressure fall in mid-latitude explosive oceanic cyclones. In Chapter 3 we introduce this source of heat into the models of chapter 2 and examine its consequences on

the development of 'moist' baroclinic waves.

2.1

We begin the investigation of this problem with a 2-D 2-level model formulated in the semi-geostrophic approximation. We consider an Eady-like model (uniform shear and static stability; Boussinesq approximation; f-plane) that we will solve only on two levels in the vertical: the minimal discretisation that retains baroclinic instability. The perturbations are assumed to have infinite meridional scale, so that all the y-derivatives are zero, except for the basic state temperature gradient that balances the vertical shear. The use of the SG approximation is suggested by the form of convective parameterisation chosen, because potential vorticity appears naturally in the equations in place of static stability. It also allows a study of finite amplitude effects (for 2-D perturbations only) since the equations transformed in 'geostrophic space' become linear without the need of any 'small amplitude' assumption (with one exception to be mentioned later).

We then start with the equations in the geostrophic momentum approximation, that we write

$$\begin{cases} (\partial_t + u\partial_x + v\partial_y + w\partial_z)\, u_g - f_0 v_a = 0 \\ (\partial_t + u\partial_x + v\partial_y + w\partial_z)\, v_g + f_0 u_a = 0 \\ (\partial_t + u\partial_x + v\partial_y + w\partial_z)\, \vartheta = 0 \\ f_0 v_{gz} = (g/\vartheta_0)\, \theta_x \\ u_x + v_y + w_z = 0 \end{cases} \qquad (2.1)$$

where the symbols have their usual meteorological meaning and thermal wind has been used in place of the hydrostatic relation to avoid explicit reference to pressure.

Consider a steady solution $\bar{u}(z), \bar{\theta}(y,z)$ satisfying $f_0 \bar{u}_z = -(g/\theta_0)\bar{\theta}_y$ and y-independent perturbations to this mean state (which implies $u_g' = 0$). The equations for the perturbations are:

$$\begin{cases} \bar{u}_z w = f_0 v_a \\ (\partial_t + u\partial_x + w\partial_z) v_g + f_0 u_e = 0 \\ (\partial_t + u\partial_x)\theta' + v\bar{\theta}_y + w\theta_z = 0 \\ f_0 v_{gz} = (g/\theta_0)\theta_x \\ u_{ex} + w_z = 0 \end{cases} \qquad (2.2)$$

We here derive the linearized equations first, and then we will show that the coordinate transformation to geostrophic space leads to the same result. If we linearize at this point we get

$$(\partial_t + \bar{u}\partial_x) v_g + f_0 u_e = 0 \qquad (2.3)$$

for the momentum equation, and

$$(\partial_t + \bar{u}\partial_x)\theta' + (v_g + v_e)\bar{\theta}_y + w\bar{\theta}_z = 0 \qquad (2.4)$$

for the thermodynamics. Using the first of (2.2) this can be written

$$(\partial_t + \bar{u}\partial_x)\theta' + v_g\bar{\theta}_y + w\left(\bar{\theta}_z + \bar{\theta}_y \frac{\bar{u}_z}{f_0}\right) = 0 \qquad (2.5)$$

or, recalling the definition of potential vorticity

$$q_d = (\vec{\nabla} \times \vec{u}_g + f_0 \hat{k}) \cdot \vec{\nabla}\theta / \theta_0 \qquad (2.6)$$

so that $\bar{q}_d = (\bar{u}_z \bar{\theta}_y + f_0 \bar{\theta}_z)/\theta_0$ is the potential vorticity of the mean state

$$(\partial_t + \bar{u}\partial_x)\theta' + v_g \bar{\theta}_y + w \frac{\theta_0}{f_0} \bar{q}_d = 0 \qquad (2.7)$$

From the continuity equation we can define a streamfunction for the secondary circulation ψ, such that $w = \psi_x$ and $u_a = -\psi_z$; system (2.2) reduces to

$$\begin{cases} (\partial_t + \bar{u}\partial_x) v_g - f_0 \psi_z = 0 \\ (\partial_t + \bar{u}\partial_x)\theta' + v_g \bar{\theta}_y + \psi_x (\theta_0/f_0) \bar{q}_d = 0 \\ f_0 v_{gz} = (g/\theta_0)\theta_x' \end{cases} \qquad (2.8)$$

which is a closed system for the unknowns v_g, ψ, θ, with $v_a = (\bar{u}_z/f_0)\psi_x$ as a diagnostic relation for the ageostrophic component of meridional velocity.

On the other hand we could apply to (2.2) the transformation

$$\begin{cases} X = x + v_g/f_0 \\ Y = y - \bar{u}/f_0 \\ Z = z \\ T = t \end{cases} \Longrightarrow \begin{cases} \partial_x \equiv \dfrac{1}{1 - v_{gx}/f_0}\partial_X \; ; \; \partial_y \equiv \partial_Y \\ \partial_z \equiv \dfrac{v_{gz}/f_0}{1 - v_{gx}/f_0}\partial_X - \dfrac{\bar{u}_z}{f_0}\partial_Y + \partial_Z \\ \partial_t \equiv \dfrac{v_{gT}/f_0}{1 - v_{gx}/f_0}\partial_X + \partial_T \end{cases}$$

which immediately gives

$$\begin{cases} v_{gT} + \bar{u} v_{gX} - f_0 \psi_Z = 0 \\ \theta_T + \bar{u} \vartheta_X + v_g \bar{\vartheta}_Y + \psi_X \dfrac{\theta_Z}{1 - v_{gX}/f_0} = 0 \\ f_0 v_{gZ} = (g/\theta_0)\, \theta_X \end{cases} \tag{2.9}$$

It is easy to see that these equations imply

$$\left(\vartheta_T + u \vartheta_X + \frac{\psi_X}{1 - v_{gX}/f_0} \vartheta_Z \right) \frac{\theta_Z}{1 - v_{gX}/f_0} = 0$$

so we identify the quantity

$$q_d = \frac{\theta_Z}{1 - v_{gX}/f_0} \frac{f_0}{\theta_0}$$

as the potential vorticity; this definition coincides with (2.6) to o(Ro) (see McWilliams and Gent, 1980) and it is then consistent with the GM approximation. To recover the physical quantities the non-linear inverse transformation from 'geostrophic' to physical space shall have to be applied. Equations (2.9) are formally identical to (2.8); in particular they are linear, because q_d is conserved, if q_d is chosen to be uniform at some initial time (if q_d is not uniform then $q_d(X, Z, T)$ depends on the solution itself, although it is conserved following individual parcels of fluid). The diagnostic relation for v_a assumes the form

$$v_a = \frac{\bar{u}_Z}{f_0} \frac{\psi_X}{1 - v_{gX}/f_0} \tag{2.10}$$

We derived the above set of equations for an adiabatic system, in which the dry entropy $c_p \ln\theta$ is conserved following the motion of individual parcels of fluid: $(d/dt)\ln\theta = 0$ or (within the Boussinesq approximation) $(d/dt)\theta = 0$; this is still true of moist air as long as no changes of phase occur (strictly we should substitute θ_v for θ but the difference is of order one percent for realistic atmospheric values of potential temperature and mixing ratio). When condensation occurs the source term that appears in the thermodynamic equation $\frac{d\theta}{dt} = -\frac{L}{c_p \pi_0}\frac{dq_{vs}}{dt}$ (*) can be accounted for by defining an equivalent potential temperature $\theta_e = \theta + \frac{L}{c_p \pi_0} q_v$ (*) that is conserved for all motions in which the only heat source is the release of latent heat of condensation; for all ascending motions in our model, that we assume saturated, we then use the equation of conservation of θ_e : $d\theta_e/dt = 0$ instead of $d\theta/dt = 0$. Therefore the thermodynamic equation in regions of ascending motion is written:

$$\theta_{eT} + \bar{u}\,\theta_{eX} + v_g\,\overline{\theta_e}_Y + \eta/f_0\,\Psi_X\,\theta_{eZ} = 0 \qquad (2.11)$$

where

$$\eta/f_0 = \frac{1}{1 - v_{gX}/f_0} = 1 + v_{gx}/f_0$$

so that η is the absolute vorticity. The equivalent potential temperature has with the moist entropy the same relation that θ has

---

(*) Both these definitions use the approximation in which π is replaced by a constant π_0.

with dry entropy; and there exists a relation

$$\Gamma_m \left(d \ln \theta_e\right)_p = \Gamma_d \left(d \ln \theta\right)_p$$

between the differentials at constant pressure of dry and moist entropy for a saturated parcel of air (see Emanuel,1986). The above is exactly true at constant pressure - we assume that it holds at constant height and write $\Gamma_m (d\theta_e)_z \simeq \Gamma_d (d\theta)_z$. Here $\Gamma_d = -g/c_p$ is the dry adiabatic lapse rate and Γ_m the moist adiabatic lapse rate. We can then rewrite the equation of conservation of θ_e (2.11) as

$$\frac{\Gamma_d}{\Gamma_m}\left(\theta_T + \bar{u}\,\theta_X + v_g \bar{\theta}_Y\right) + \eta/f_0\, \psi_X\, \theta_{eZ} = 0$$

or

$$\theta_T + \bar{u}\,\theta_X + v_g \bar{\theta}_Y + \psi_X \frac{\eta}{f_0}\frac{\Gamma_m}{\Gamma_d}\theta_{eZ} = 0 \qquad (2.12)$$

As the quantity

$$q_e = \frac{f_0}{\theta_{e_0}}\,\frac{\theta_{eZ}}{1 - v_{gX}/f_0} \simeq \left(\vec{\nabla} \times \vec{u}_g + f_0 \hat{k}\right)\cdot\frac{\vec{\nabla}\theta_e}{\theta_{e_0}}$$

(equivalent potential vorticity) is conserved by the flow this equation is entirely similar to the thermodynamic equation in (2.9) and we can write the two of them as

$$\theta_T + \bar{u}\,\theta_X + v_g \bar{\theta}_Y + \psi_X\, q^* = 0 \qquad (2.13)$$

where $q^* = (\theta_{e_0}/f_0)(\Gamma_m/\Gamma_d)\, q_e$ in updraft regions and $q^* = (\theta_0/f_0)\, q_d$ in regions of descending motion.

Two observations have to be made concerning the similarity of treatment of saturated and unsaturated motions. First, the moist adiabatic lapse rate is in general a function of the thermodynamic variables, and so a function of position, even though the main variability is with height. In the two-level model below we will solve the thermodynamic equation only at mid-level, so we ignore all variability of Γ_m and give it a constant value. Second, q_d is not conserved where condensation occurs - the effect of release of latent heat is to create an anomaly of q_d that is of no concern in the updraft region itself, because there q_e is the dynamically relevant parameter; however this anomaly of q_d can be advected out of the region of ascending motion and into the downdraft, where it is dynamically significant. We ignore this effect as small in the following - we can regard this approximation as a linearization of the term $\psi_x q^*$ in (2.13), and this is then the only linearization that we are forced to make in order to derive a linear system of equations. On the other hand, by writing (2.12) as

$$\theta_T + \bar{u}\,\theta_x + v_g\,\bar{\theta}_y + \psi_x\,\eta/f_0\,\theta_z = \psi_x\,\eta/f_0\left(\theta_z - \frac{\Gamma_m}{\Gamma_d}\,\theta_{ez}\right)$$

and deriving the potential vorticity equation from here, we get (e.g. Thorpe and Emanuel, 1985)

$$\frac{dq_d}{dt} = \frac{\eta}{f_0}\,\partial_z\left(\psi_x\left(q_d - \frac{\Gamma_m}{\Gamma_d}\,q_e\right)\right) \qquad (2.14)$$

Now, again, in the 2-level discretisation the thermodynamic equation is solved only at mid-level; q_d is initially uniform by assumption, and so is q_e; the z-dependence of Γ_m has already been neglected and its

contribution is anyhow small as $q_e \to 0$; the only remaining term on the r.h.s. of (2.14) is ψ_{xz}, but if ψ is taken equal to zero at top and bottom boundaries (where the physical boundary condition is w = 0, i.e. $\psi_x = 0$ or ψ = const.) then $\psi_z = 0$ at mid- level (*) is the only value consistent with the two level discretisation, and q_d at mid-level is conserved even in the presence of condensation, because the use of only one level as representative of the thermodynamics is equivalent to the assumption that heating is vertically uniform - a condition that does not change potential vorticity. For all purposes we can therefore consider the 2-level solutions derived below as finite amplitude solutions in geostrophic space. We get exponential growth at finite amplitude because the infinite meridional temperature gradient provides an infinite reservoir of APE and the perturbations do not interact with the basic state: they are added to the mean flow and do not modify it (**). In any system with a finite meridional scale the amplitude of the perturbation would of course be bounded as $t \to \infty$ and not grow indefinitely.

Taking the basic wind to be zero at mid level, so that the

(*) Note that this is true in geostrophic space. When the inverse transformation is applied vertical lines become M lines, so the derivative of ψ along M surfaces will have a maximum at mid-level, but not necessarily so the vertical derivative. However the absolute extrema, where both ψ_X and ψ_Z, or ψ_x and ψ_z are zero are at mid-level in both coordinate systems.

unstable Eady waves are stationary, we write the equations for the 2-level (shown in fig. 2.1) as

$$\begin{cases} (\sigma+\bar{u}\partial_x)\nu_1 + \dfrac{f_0}{h}\psi = 0 \\ (\sigma-\bar{u}\partial_x)\nu_2 - \dfrac{f_0}{h}\psi = 0 \\ \sigma\vartheta + \dfrac{\nu_1+\nu_2}{2}\bar{\vartheta}_y + \psi_x q^* = 0 \\ \vartheta_x - \dfrac{f_0\theta_0}{g}\dfrac{\nu_1-\nu_2}{h} = 0 \end{cases} \qquad (2.15)$$

where it has been assumed that the time dependence of the solution is $\sim e^{\sigma T}$, the boundary condition $\psi = 0$ at top and bottom boundaries has been applied, $\bar{\vartheta}_y = -\frac{f_0\theta_0}{g}\frac{2\bar{u}}{h}$ is the thermal wind relation for the base state, and

$$q^* = \begin{cases} q_d\, \theta_0/f_0 & \text{where } w<0 \\ q_e \dfrac{\theta_{e0}}{f_0}\dfrac{\Gamma_m}{\Gamma_d} & \text{" } w>0 \end{cases}$$

(**) Notice however that this is so in geostrophic space only. In physical space the self-advection of the perturbation, represented by the transformation of coordinates, introduces an algebraically growing term that leads to the frontal collapse, after which the transformation is no longer valid (and the GM approximation itself breaks down before this occurs)

We will solve the system for the unknowns $v_1, v_2, \psi, \vartheta$ separately in regions of ascending and descending motion: in each of them the system is linear with constant coefficients, but one of the coefficients (q^*) has different values in the two regions. The solutions will then be matched at the interfaces to insure continuity of the relevant physical quantities. The use of a zero (or small) q_e in the region of ascending motion constitutes the parameterization of the effects of slantwise convection on the large scale flow that we discussed in Ch.1. System (2.15) can be written in non-dimensional form as

$$\begin{cases} (\sigma + \partial_X) v_1 + \psi = 0 \\ (\sigma - \partial_X) v_2 - \psi = 0 \\ \vartheta_X = v_1 - v_2 \\ \sigma \vartheta - (v_1 + v_2) + q \psi_X = 0 \end{cases} \tag{2.16}$$

where (denoting dimensional variables with an *)

$$X = \frac{f_0}{h} \frac{1}{\sqrt{g q_d / f_0}} X^* \; ; \; \sigma = \frac{h}{f_0 \bar{u}} \sqrt{\frac{g q_d}{f_0}} \sigma^* \; ; \; \psi = \frac{\psi^*}{\bar{u} h}$$

$$v = \frac{1}{h} \frac{1}{\sqrt{\frac{g q_d}{f_0}}} v^* \; ; \; \vartheta = \frac{f_0}{h q_d} \frac{\theta^*}{\theta_0} \; ; \; q = \frac{f_0}{\theta_0 q_d} q^*$$

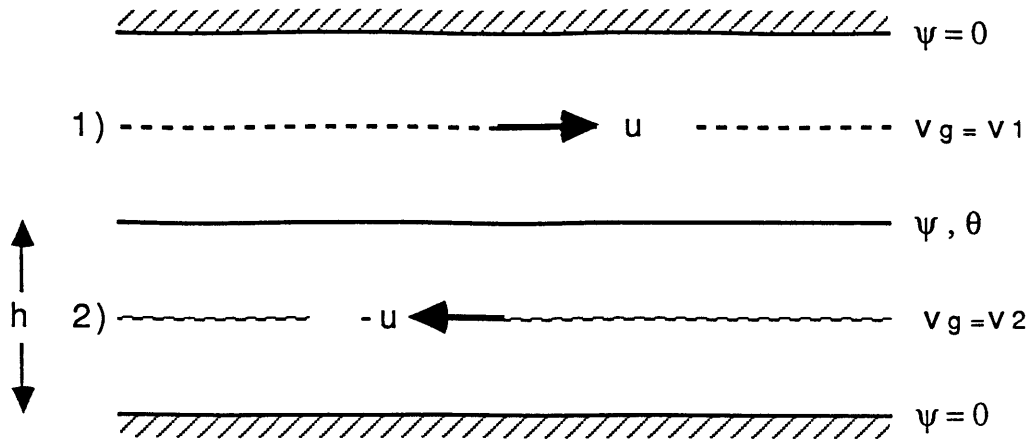


Fig.2.1 - Structure of the 2-level model , and levels where variables are defined.

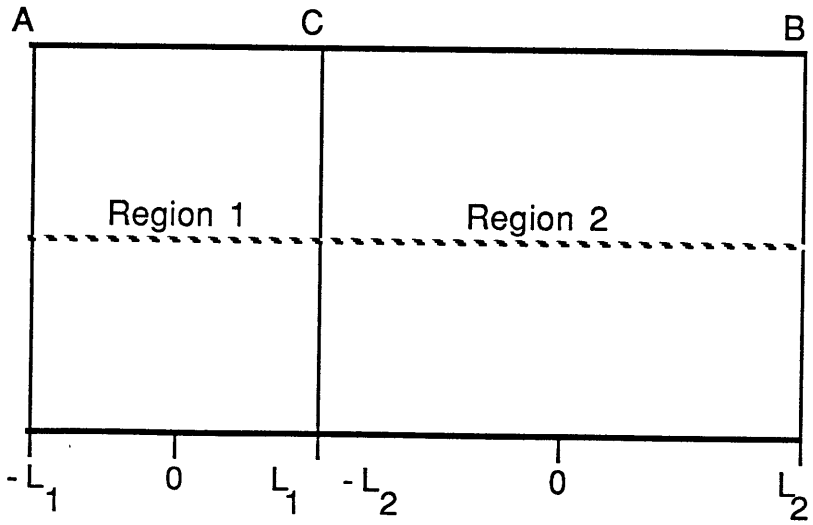


Fig. 2.2 - Subdivision of the model in a 'moist' and a 'dry' region . Horizontal coordinate X is defined separately in each region. Solutions are matched at points A=B and C.

Note that the horizontal length scale is $(h/f_0)\sqrt{g q_d / f_0}$, or the Rossby radius of deformation in the SG approximation, where the static stability has been replaced by potential vorticity. The non dimensional quantity q is the ratio of the stability parameter in the region of ascending motion to the dry potential vorticity. Its value is

$$q = \begin{cases} 1 & \text{where } \psi_x < 0 \\ r & \text{" } \psi_x > 0 \end{cases} ; \quad r \equiv \frac{\sigma_{e0}}{\sigma_0} \frac{\Gamma_m}{\Gamma_d} \frac{q_e}{q_d} < 1$$

From (2.16) an equation for ψ can be derived

$$2(\sigma^2 + D_x^2)\psi - (\sigma^2 - D_x^2)(q\psi_x)_x = 0 \tag{2.17}$$

and the other variables are given in terms of ψ by

$$\begin{cases} 2\sigma(v_1 - v_2) + 2\psi + (q\psi_x)_x = 0 \\ 2\sigma^2(v_1 + v_2) - 2\psi_x - (q\psi_x)_{xx} = 0 \\ \sigma\theta - (v_1 + v_2) + q\psi_x = 0 \end{cases} \tag{2.18}$$

Equation (2.17) is valid everywhere, for a general $q(x)$. We now assume that the solution is periodic over a length 2L and divide the domain in two regions as in fig. 2.2, and we require the solution to have positive vertical velocity in region 1 and negative in region 2.We then specialize (2.17) to q = const. to get

$$q\psi_{xxxx} + (2 - \sigma^2 q)\psi_{xx} + 2\sigma^2\psi = 0 \tag{2.19}$$

that is valid in the interior of the two regions, with q = 1 in region 2 and q = r in region 1. The solutions have to be matched at points C and A (=B) of fig. 2.2. The appropriate matching conditions will now be derived.

The derivation of the matching conditions is slightly different in physical space, for the linearized system, or in geostrophic space for the full system, although the resulting conditions are identical. We show here the argument for the finite amplitude model in geostrophic space that we study in this section (see Appendix 2.A for the linearized version). First we require the transformation to be continuous, which implies v continuous, or v_1 and v_2 continuous in the 2-level. Since we will solve the equation (2.19) for ψ we want to write those conditions in terms of ψ and its derivatives: (2.18) gives that $2\psi + (q\psi_x)_x$ and $2\psi_x + (q\psi_x)_{xx}$ have to be continuous at the interface. The usual approach to the kinematic matching condition in this kind of problems is to require the displacement of the interface to be the same in the two regions. This is right if the interface is a material surface, so that the fluid cannot go through it (e.g., Lamb, 1932), but this is not the case in our system. We adopt a different argument based on the equation of continuity, i.e. that the velocity normal to the interface has to be continuous - if this were not so the requirement of mass conservation would generate a jump of the tangential velocity along the original interface, and so generate a new surface of discontinuity, orthogonal to the first one, in the interior of the regions where the solutions are supposed to be well

behaved. Since we are thinking of a vertical interface in geostrophic space, it will be an M line in physical space; we can write the unit vector normal to an M line as

$$\frac{1}{\left((v_{gx}+f_0)^2+v_{gz}^2\right)^{1/2}}\left[(v_{gx}+f_0)\hat{i}+v_{gz}\hat{k}\right]$$

in physical coordinates, so that

$$\vec{u}\cdot\hat{n}=\frac{1}{\sqrt{1+v_{gz}^2/f_0^2}}(\bar{u}-\psi_z) \tag{2.20}$$

in geostrophic coordinates. We have already required the continuity of v_g in geostrophic space, and we note that the continuity of a function across a vertical line implies that all its derivatives along that line are continuous too. Therefore v_{gz} is continuous and (2.20) reduces to the continuity of ψ_z, or ψ itself in the 2-level. Finally we need the pressures at the two sides of the interface to be the same: since $v_g=p_x=\frac{p_X}{1-v_{gX}}$ (in non-dimensional form) we multiply the first of (2.16) by $(1-v_{iX})$ to get

$$\sigma v_i(1-v_{iX})+(v_{iX}+\psi)(1-v_{iX})=0$$

and integrate across the discontinuity in geostrophic space

$$\sigma p_i\Big|_{-\varepsilon}^{+\varepsilon}+\int_{-\varepsilon}^{+\varepsilon}(v_{iX}+\psi)(1-v_{iX})\,dX=0$$

Now we make use again of $v_{iX}=-\sigma v_i-\psi$ to write

$$\sigma p_i\Big|_{-\varepsilon}^{+\varepsilon}+\int_{-\varepsilon}^{+\varepsilon}(v_{iX}+\sigma v_i v_{iX}+v_{iX}\psi+\psi-\psi v_{iX})\,dX=0$$

or

$$\left[\sigma p_i+v_i+\sigma v_i^2/2\right]_{-\varepsilon}^{+\varepsilon}+\int_{-\varepsilon}^{+\varepsilon}\psi\,dX=0$$

Therefore the continuity of p_1 is equivalent to the requirement $\int_{-\varepsilon}^{+\varepsilon} \psi \, dX = 0$, because we have already imposed ψ_1 to be continuous. The same result is obtained for p_2 from the second of eq.s (2.16)(*). We can now express this condition in terms of ψ and its derivatives by integration of 2.17 across the interface:

$$2\sigma^2 \int_{-\varepsilon}^{+\varepsilon} \psi \, dX + \left[2\psi_X + (q\psi_X)_X\right]_{-\varepsilon}^{+\varepsilon} - \left[\sigma^2 q \psi_X\right]_{-\varepsilon}^{+\varepsilon} = 0$$

The term in the first square bracket is zero because it is equal to $2\sigma(\psi_1 - \psi_2)$ (see eq. 2.18) and so we are left with the requirement of continuity of $q\psi_X$. To summarize, the four matching conditions are on

$$\psi, \; q\psi_X, \; (q\psi_X)_X, \; 2\psi_X + (q\psi_X)_{XX} \qquad (2.21)$$

The next step is to consider that we have a requirement on the structure of the solution, namely that $w > 0$ in region 1 and $w < 0$ in region 2, that is not included in either the equation (2.19) or the interface conditions (2.20). We assume that w has a definite sign when we choose to apply the 'moist' thermodynamic equation to region 1 and

---

(*) note that while we always write 'continuity', what we really mean is that the value of the function evaluated on one side of the interface is equal to the value on the other side. This does not guarantee that the function does not have a singularity right at the interface, like a δ-function, that is not detected by the function itself but results in a finite jump of its primitive. Therefore, if we have physical reasons to require the primitive to be continuous, we have to impose it as an added condition.

the 'dry' one to region 2, but if we solve the problem in the form it has been posed up to this point we will get solutions that do not in general satisfy this requirement. We would have then to look at the structure of the solutions and retain only those that are acceptable from this point of view

. . . We can however filter out some of the unwanted modes with the following argument. We want ψ_x to change sign at the interfaces, so $q\psi_x$ has to change sign as well, because q is positive; but the second interface condition guarantees that $q\psi_x$ is continuous too, so it has to be zero at the interface - again $q \neq 0$ everywhere so $\psi_x = 0$ at the interfaces (*).We then replace the condition $q\psi_x|_{-\varepsilon}^{+\varepsilon} = 0$ with $\psi_x^{(1,2)} = 0$. When this condition is imposed we know that the solutions for r=1, i.e. the 'dry' 2-level model, will be $w \sim \sin \frac{\pi}{2L} n$, n=1,2,... (4L being the wavelength and L1=L2 in fig 2.2). The only solution that we consider acceptable is the one with n=1, that does not have any zeroes in the interior of each region, but only one at the interface between the two regions. We will then proceed from this solution at r=1 with small decrements of r, using the solution at each step as an initial guess for the next one, down to values of r close to zero. Another observation that helps in the numerical solution is that both eq. 2.1 and the conditions 2.2 imply either odd or even derivatives of the streamfunction, but not both kinds

---

(*) in other words the jump in q conserves the sign, then for $q\psi_x$ to be continuous the jump in ψ_x must conserve the sign as well, unless it is zero. And we discard the former.

together. In this situation, and using two different coordinate systems in the two regions as shown in fig 2.2, we can write two separate problems for the symmetric (ψ_S) and antisymmetric (ψ_A) part of the solution, defined as $2\psi_S = \psi(x) + \psi(-x)$; $2\psi_A = \psi(x) - \psi(-x)$. A purely symmetric solution will have a zero of w in the interior, and so cannot be used. We cannot exclude solutions with a small (not large enough to change the sign of w) symmetric part superposed on the antisymmetric one but we note that ψ_S and ψ_A will have two different dispersion relations: combined solutions are then possible (if they exist at all) only at a discrete set of points in parameter space, where the two dispersion relations intersect. We will consider in the following only $\psi = \psi_A$: this will give all the eigenvalues; the possible degeneration in the form of the eigenfunctions for some values of the parameters would probably have to be resolved invoking some other constraint not included in this model.

We are now ready to proceed from a general solution (*) to (2.19) in the form $w^{(1,2)} = a_+^{(1,2)} e^{\alpha^{(1,2)} x} + a_-^{(1,2)} e^{-\alpha^{(1,2)} x} + b_+^{(1,2)} e^{\beta^{(1,2)} x} + b_-^{(1,2)} e^{-\beta^{(1,2)} x}$

$$\left(\alpha^{(1,2)}, \beta^{(1,2)}\right)^2 = \frac{1}{2}\left[\sigma^2 - \frac{2}{q^{(1,2)}} \pm \left(\left(\sigma^2 - \frac{2}{q^{(1,2)}}\right)^2 - \frac{8\sigma^2}{q^{(1,2)}}\right)^{1/2}\right]$$

(*) There are a few degenerate cases in which this is not the general solution. The only case of practical interest is $\sigma = 2 - \sqrt{2}$, which is the maximum growth rate of the dry (r=1) model, because the dispersion relation found numerically takes this value at two points. While the solution , exists anyway at these two points, we did not examine the consequences of adding the extra terms $x e^{\pm\alpha x}$.

Here we allow the wave numbers α and β to be complex, while σ^2 can be shown to be real (see Appendix 2.B). Now the requirement of antisymmetry reduces this to

$$\psi^{(1,2)} = a^{(1,2)}\left(e^{\alpha^{(1,2)}x} - e^{-\alpha^{(1,2)}x}\right) + b^{(1,2)}\left(e^{\beta^{(1,2)}x} - e^{-\beta^{(1,2)}x}\right)$$

and the conditions w = 0 give

$$\frac{a^{(1,2)}}{b^{(1,2)}} = -\frac{\beta^{(1,2)}}{\alpha^{(1,2)}}\,\frac{e^{\beta^{(1,2)}L_{1,2}} + e^{-\beta^{(1,2)}L_{1,2}}}{e^{\alpha^{(1,2)}L_{1,2}} + e^{-\alpha^{(1,2)}L_{1,2}}}$$

so that

$$\psi^{(1,2)} = b^{(1,2)}\left[\left(\frac{a}{b}\right)^{(1,2)}\left(e^{\alpha^{(1,2)}x} - e^{-\alpha^{(1,2)}x}\right) + \left(e^{\beta^{(1,2)}x} - e^{-\beta^{(1,2)}x}\right)\right]$$

and the remaining matching conditions on $\psi, \psi_{xx}, \psi_{xxx}$ (that, because ψ has definite symmetry properties, need to be applied at one interface only) can be written as

$$\begin{bmatrix} -\frac{\beta_1}{\alpha_1}\frac{ch\beta_1L_1}{ch\alpha_1L_1}sh\alpha_1L_1 + sh\beta_1L_1 & -\frac{\beta_2}{\alpha_2}\frac{ch\beta_2L_2}{ch\alpha_2L_2}sh\alpha_2L_2 + sh\beta_2L_2 \\ q\left(-\frac{\beta_1}{\alpha_1}\frac{ch\beta_1L_1}{ch\alpha_1L_1}\alpha_1^2sh\alpha_1L_1 + \beta_1^2sh\beta_1L_1\right) & -\frac{\beta_2}{\alpha_2}\frac{ch\beta_2L_2}{ch\alpha_2L_2}\alpha_2^2sh\alpha_2L_2 + \beta_2^2sh\beta_2L_2 \\ q\left(-\frac{\beta_1}{\alpha_1}\frac{ch\beta_1L_1}{ch\alpha_1L_1}\alpha_1^3ch\alpha_1L_1 + \beta_1^3ch\beta_1L_1\right) & \frac{\beta_2}{\alpha_2}\frac{ch\beta_2L_2}{ch\alpha_2L_2}\alpha_2^3ch\alpha_2L_2 - \beta_2^3ch\beta_2L_2 \end{bmatrix} \begin{bmatrix} b_1 \\ b_2 \end{bmatrix} = 0 \qquad (2.22)$$

This system has non-trivial solutions if the matrix has rank one, which requires that two second order determinants be zero. Having proved

that σ^2 is real the determinants are real or pure imaginary. In either case we have two real conditions that relate the four real parameters $\sigma^2, \lambda \equiv \frac{L_1}{L_2}, L_2, r$. Two of them are then free: we choose L_2 and r , that we treat as independent variables, and solve for the eigenvalues σ and λ .

We begin the presentation of the results with the dry case r=1 (i.e. q=1 everywhere). In this case (2.18) can be solved for plane waves of wavenumber k, giving explicitly the eigenvalue $\sigma^2 = k^2 \frac{2 - k^2}{2 + k^2}$. This is the classic result for an f-plane 2-level model (e.g. Pedlosky, 1979 - eq. (7.11.13)) except that the dimensional quantities involve g_d rather than N^2. This explicit solution was used to test the performance of the numerical procedure. Note that in this case the wavenumber has to be real - if q is uniform there are no vertical boundaries and the solution has to be bounded at infinity. In a model where q = const. < 1 everywhere we would get

$$q\sigma^2 = qk^2 \frac{2 - qk^2}{2 + qk^2} \qquad (2.23)$$

for the dispersion relation. In a σ, k plane this is just a stretching of both axis by a factor $\sqrt{q}$. If we insist on real wavenumbers in a model like the one presented here, with one region of q=1 and one of q=r, each one will have the dispersion relation (2.23) with the appropriate scale factor. We would probably be unable to satisfy all the matching conditions (2.20), but the minimal requirement that σ be the same in both regions will give solutions that have at most the growth rate of the dry model, i.e. the least unstable part of the

domain will determine the properties of the whole solution (see for instance Tang and Fichtl,1983). We are able to overcome this limitation because we are in fact allowed to use complex wavenumbers - when the model is not uniform in x the normal modes are not necessarily plane waves. In this model we solve (2.19) on a bounded domain and we do not have to worry about the behavior at infinity.

Before going to the actual numerical results we can make some a priori considerations on the effect of reducing r. We know from classical baroclinic instability theory that the most unstable mode scales with the Rossby radius of deformation (that in this model is defined with q in place of N^2). We can expect the horizontal structure in each region to be defined by its own q, i.e. $\lambda \sim \sqrt{q_2}/\sqrt{q_1} = \sqrt{r}$. Moreover the growth rate scales with $\frac{\bar{u}_z f_0}{\sqrt{q}}$ when q is uniform (see also 2.23). We could use as a preliminary guess for the growth rate in this model a linear combination of σ at q=1 and σ at q=r, weighted with the relative area of the two regions, i.e.:

$$\sigma_{av.} = \frac{L_1 \sigma_2 + L_2 \sigma_1}{L_1 + L_2} \sim \sigma_1 \frac{2}{1+\sqrt{r}} \qquad (2.24)$$

This crude estimate turns out to be a rather good approximation to the behavior of the actual solutions as long as r >.1, while for smaller r the growth rates obtained numerically (shown in fig. 2.3) are larger than that (table 2.1 gives comparision of solutions of 2.22 and 2.24 for one value of L2). Although (2.19) is singular for $r \to 0$ we can solve (2.22) for very small r - the curve labelled r=0 in fig 2.3 is obtained asymptotically, and confirmed by numerical investigation of

Table 2.1

$L_2 = 1.8$; $\sigma_1 = .59$

r	λ	$\sqrt{r}$	σ_r	$\sigma_1 \frac{2}{1+\sqrt{r}}$
.5	.63	.71	.69	.69
.3	.46	.55	.78	.76
.2	.36	.45	.84	.82
.1	.24	.32	.94	.90
.01	.07	.10	1.24	1.07
0.	0.	0.	1.47	1.18

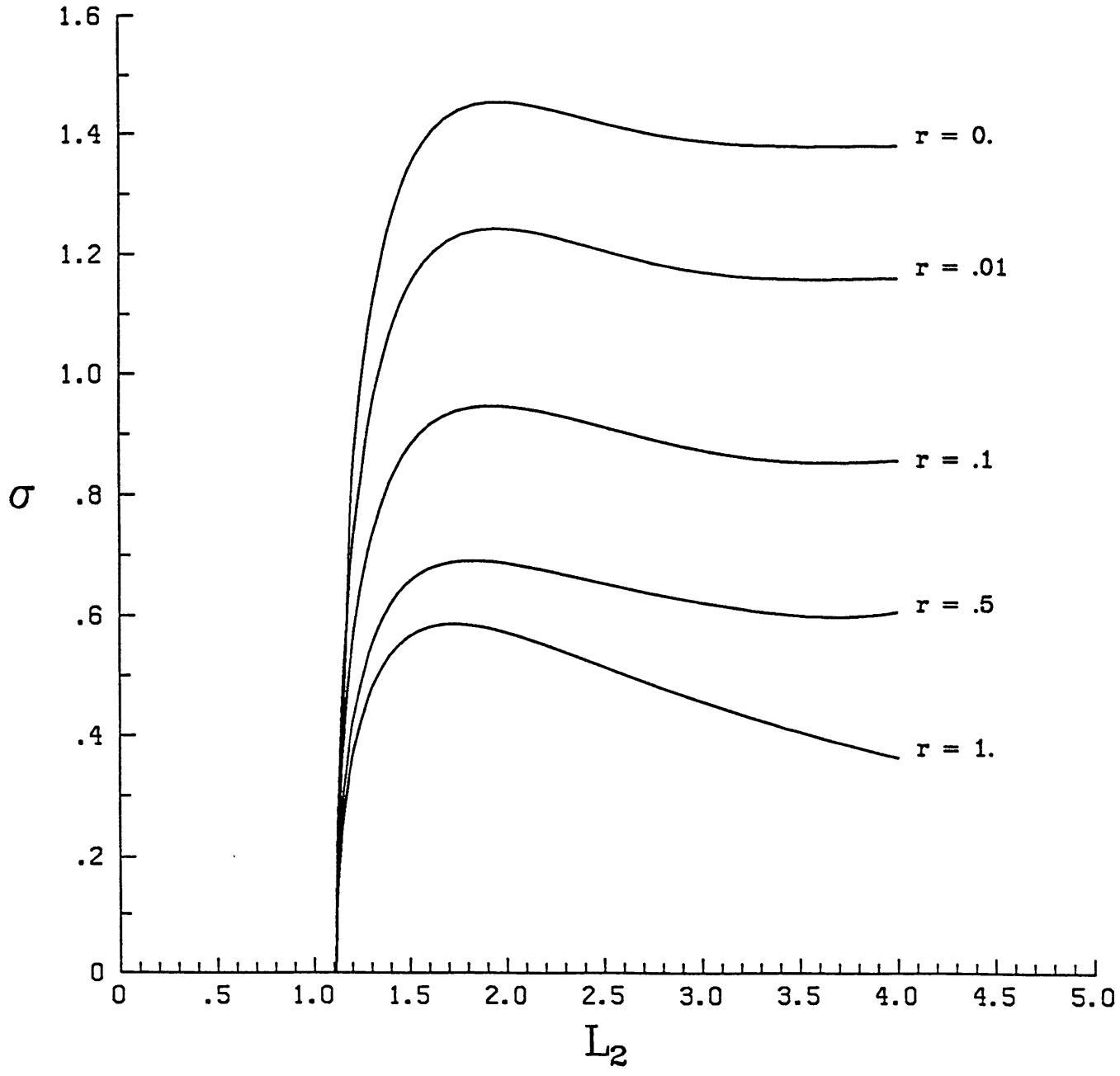


Fig.2.3 - Growth rate σ versus half-width of the downdraft L_2 for different values of r; r=1 is the dry model; r=0 is obtained asymptotically and confirmed numerically for $r \sim 10^{-6}$ (see text)

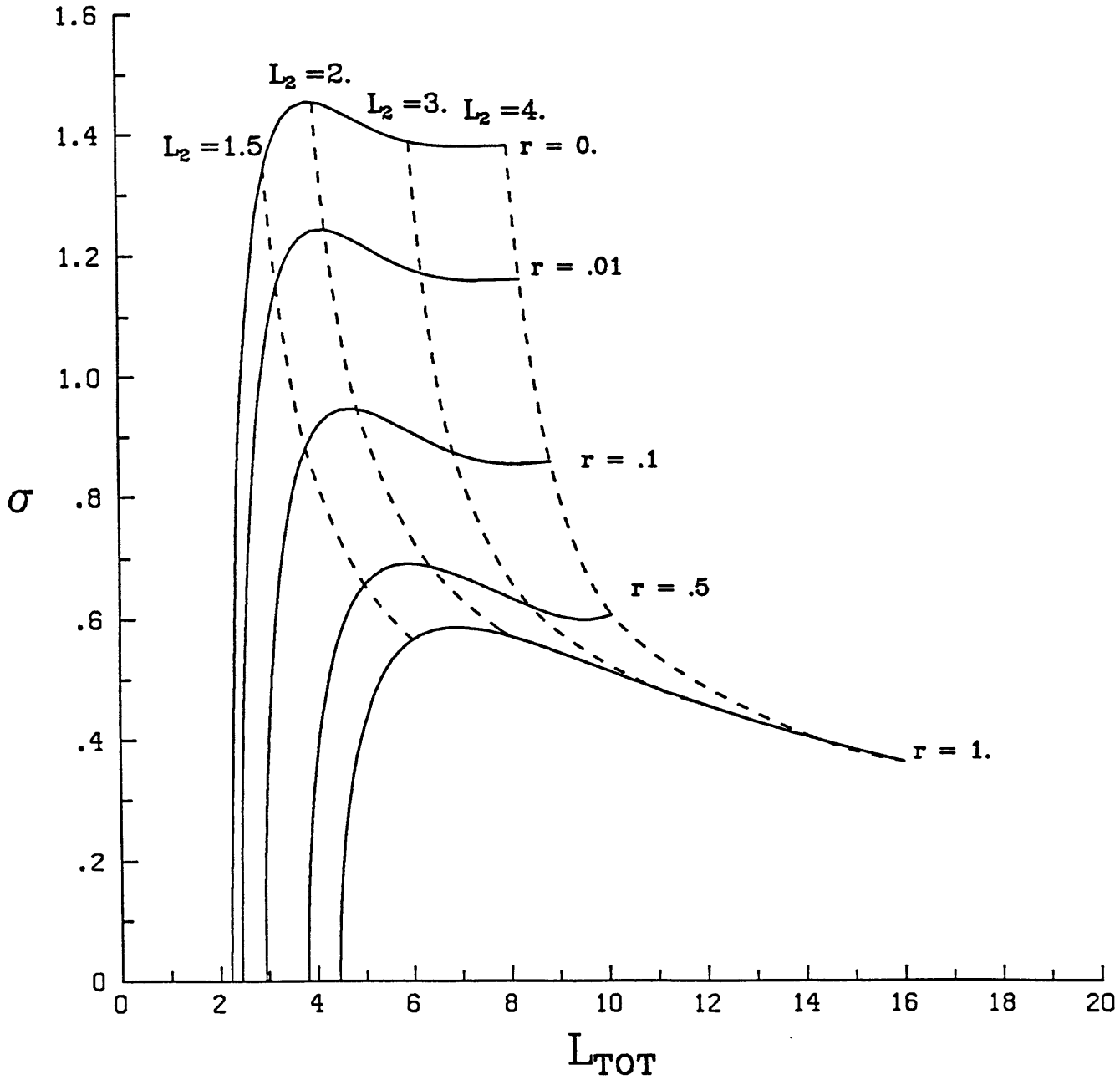


Fig.2.4 - As 2.3 but σ vs. total wavelength $L_{TOT} = 2L_2(1+\lambda)$; dashed lines join points of constant L_2, i.e. points that lay on vertical lines in fig.2.3, thus showing the reduction of total wavelength due to the narrow updraft

(2.22) for r as small as 10^{-6}. The approximate dispersion relation at r=0 is

$$\frac{2+\alpha_2^2}{\alpha_2}\tanh\alpha_2 L_2 = \frac{2+\beta_2^2}{\beta_2}\tanh\beta_2 L_2$$

(see Emanuel et al.,1987, Appendix C for the derivation). An approximate solution of this is

$$\sigma \simeq \sqrt{2}\left(1 - \frac{2\sin 2L_2}{\sin 2L_2 + \sinh 2L_2}\right)$$

valid when the second term in parenthesis is <<1, and so anywhere for L2 > 1.5. This illustrates one of the qualitative differences of fig.2.3 from (2.24) - the growth rate tends to a finite value for $L_2 \to \infty$ and not to zero as σ_d does. The oscillatory part gives a sequence of relative maxima of growth rate for $L_2 \simeq (5/8+2n)\pi$ but the amplitude of the oscillation around $\sqrt{2}$ does not exceed .01 for any L2 > 3. The absolute maximum is the first one, and occurs at L2 = 1.95, which differs from $\frac{5}{8}\pi$ by less that .02.

The abscissa in fig 2.3 is L_2, the half-width of the w<0 region, which is 1/4th of the total wavelength at r=1, but $\frac{1}{2(\lambda+1)}$th $\simeq \frac{1}{2(\sqrt{r}+1)}$th in general, as the width of the updraft decreases with $\sqrt{r}$. Thus the most unstable mode, which has an L_2 slightly increasing as r decreases has a shorter total wavelength, as shown in fig.2.4 where the same curves are redrawn as functions of L_{TOT}.

Fig 2.5 shows the horizontal structure of the solution for r=0.08 and L2 =1.8. The relative amplitude of the various fields are shown, with an arbitrary normalisation. A definite amplitude must be assumed in order to apply the inverse transformation to physical space shown in fig.2.6. The narrowness and strength of the updraft are evident, and so is the net average heating due to release of latent heat. The effect of vortex stretching is already evident in fig.2.5 in the stronger positive vorticity at low level compared to the upper level, that feeds back on itself when the inverse transformation is applied. Since in the inverse transformation from geostrophic to physical space areas of positive vorticity are compressed and areas of negative vorticity are stretched (horizontally) this asymmetry results in frontal collapse occurring at the rear of the updraft at low level, while the upper frontal zone, situated in a weak subsidence region, and thus less reinforced by stretching, is still only a broad horizontal shear zone. The positive vorticity at the rear of the updraft and the negative vorticity ahead of it translate in a very sharp gradient of w at the western edge of the updraft (see fig.2.6 where a large amplitude of the solution is assumed, to emphasize the effect of the transformation). While these results are reasonably satisfying, in that they show more adherence to observed structure and deepening rate, in contrast to dry baroclinic modes, there are a few remarks on the validity of the approximation that should be taken into account. The departure of the computed σ from the estimate (2.24) based on length scales suggests that the scaling itself may be inappropriate at very small r - indeed the model predicts an updraft of zero width at r=0,

and before this occurs the system will not be balanced, and not even hydrostatic, any longer. Previous studies of frontogenesis in an environment similar to this model (Emanuel,1985; Thorpe and Emanuel,1985) conclude that the semi-geostrophic approximation breaks down on the approach to (slantwise convective) neutrality and derive a lower bound on the admissible values of q. A similar argument can be made here, e.g. from eq.s (2.16). Since this is non-dimensional each term is o(1) in region 2; in region 1 however $\partial_x \sim 1/\lambda$ so the following relations apply:

$$D \sim S\lambda \; ; \; S \sim \psi\lambda \; ; \; \tau \sim \lambda^2 \qquad (S \equiv \nu_1 + \nu_2 \; ; \; D \equiv \nu_1 - \nu_2)$$

The ratio of advection of ageostrophic motion to that of geostrophic motion, which has to be small for the validity of the GM approximation is (in a linearized sense):

$$\frac{\nu_{ax}}{\nu_{gx}} = \frac{\nu_a}{\nu_g} \sim \frac{R_o^2 w}{\nu_g}$$

the latter relation being derived from 2.10 and

$$R_o^2 \equiv \frac{\bar{u}^2}{f_o^2 L^2} = \frac{\bar{u}^2 f_o}{h^2 g q_d}$$

Since $w = \psi_x \sim \psi/\lambda$ and $\nu_g \sim S \sim \psi\lambda$ the approximation breaks down when $R_o^2/\lambda^2 \sim 1$ or $\tau \sim R_o^2$. This relation means that the Rossby number of the updraft region, defined either with its width or with its own stability parameter, becomes o(1), so that the inertia of the secondary circulation cannot be consistently neglected. For these reasons, and encouraged by the fact that the

numerical experiments that will be discussed in sect. 2.3 do indeed show a smaller growth rate than predicted here when $\tau \to 0$ we will in the next section extend the present model to include PE dynamics. In a PE model we expect the growth rate of baroclinic modes to become smaller as Ro increases (e.g. Stone,1972) because the available potential energy must be partly used to accelerate the ageostrophic wind: the kinetic energy, that for a balanced model includes only the geostrophic terms will have all the non-geostrophic component as well. In particular we will have a prognostic equation for the zonal wind that is missing here.

As a final observation, this model could have been written, in the linearized version, from the quasi-geostrophic approximation, using N^2 instead of q (e.g. Tang and Fichtl, 1983). However the physical justification for $q_e \to 0$ does not work for N^2 : observations indicate that convective adjustment occurs on M surfaces, not vertically (e.g.Emanuel,1988). The two theories should approach each other asymptotically: indeed v_g' as scaled here is a Rossby number for the perturbation, and when $v_g' \to 0$ the M surfaces become vertical.

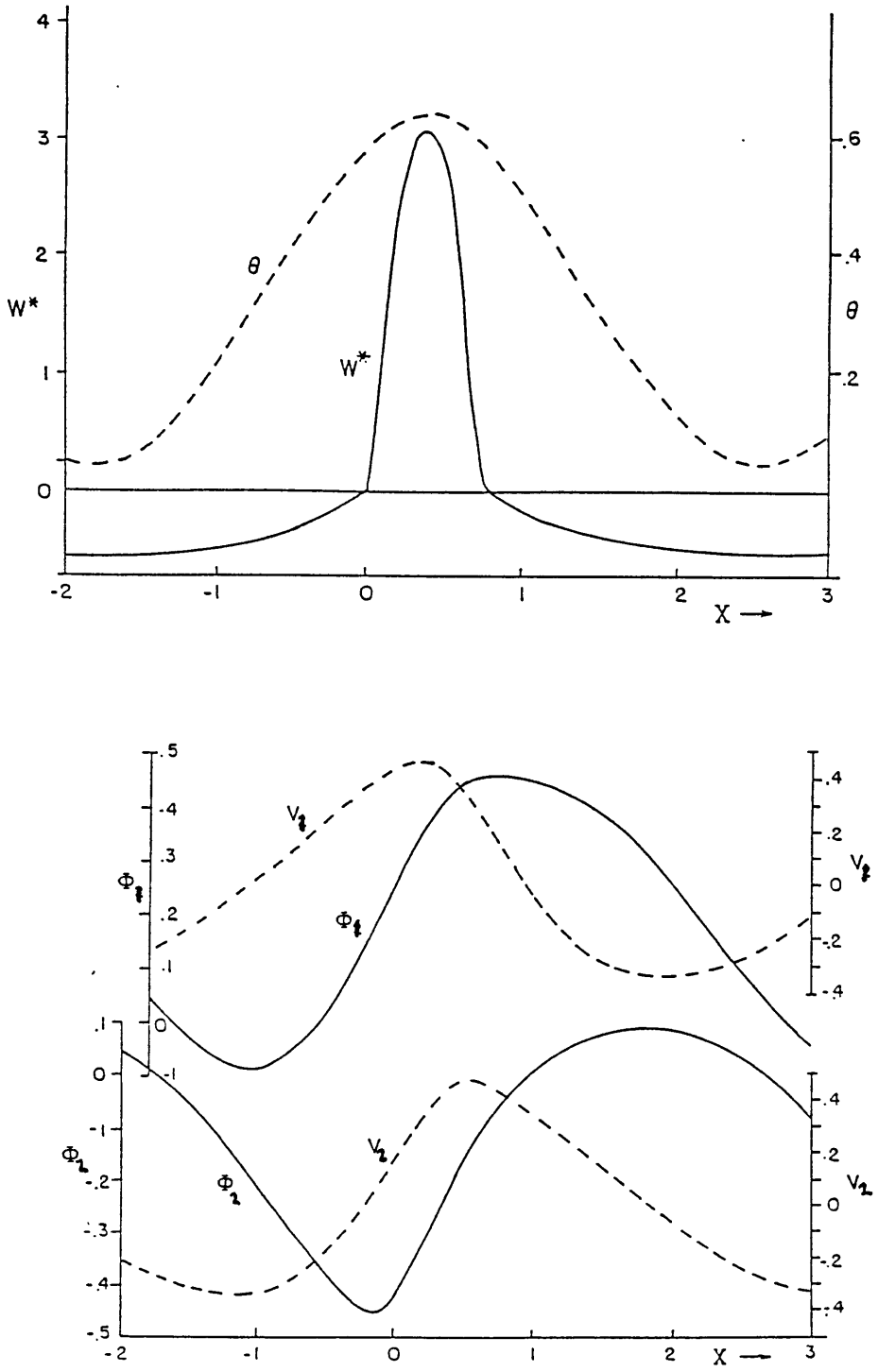


Fig.2.5 - Top: Dimensionless $w^* \equiv \psi_X$ and θ as function of the geostrophic coordinate X, for the most rapidly growing mode when r=0.08. Bottom: same but for meridional velocity v and modified geopotential $\phi \equiv p'/\rho_0 + v^2/2$ at upper and lower level

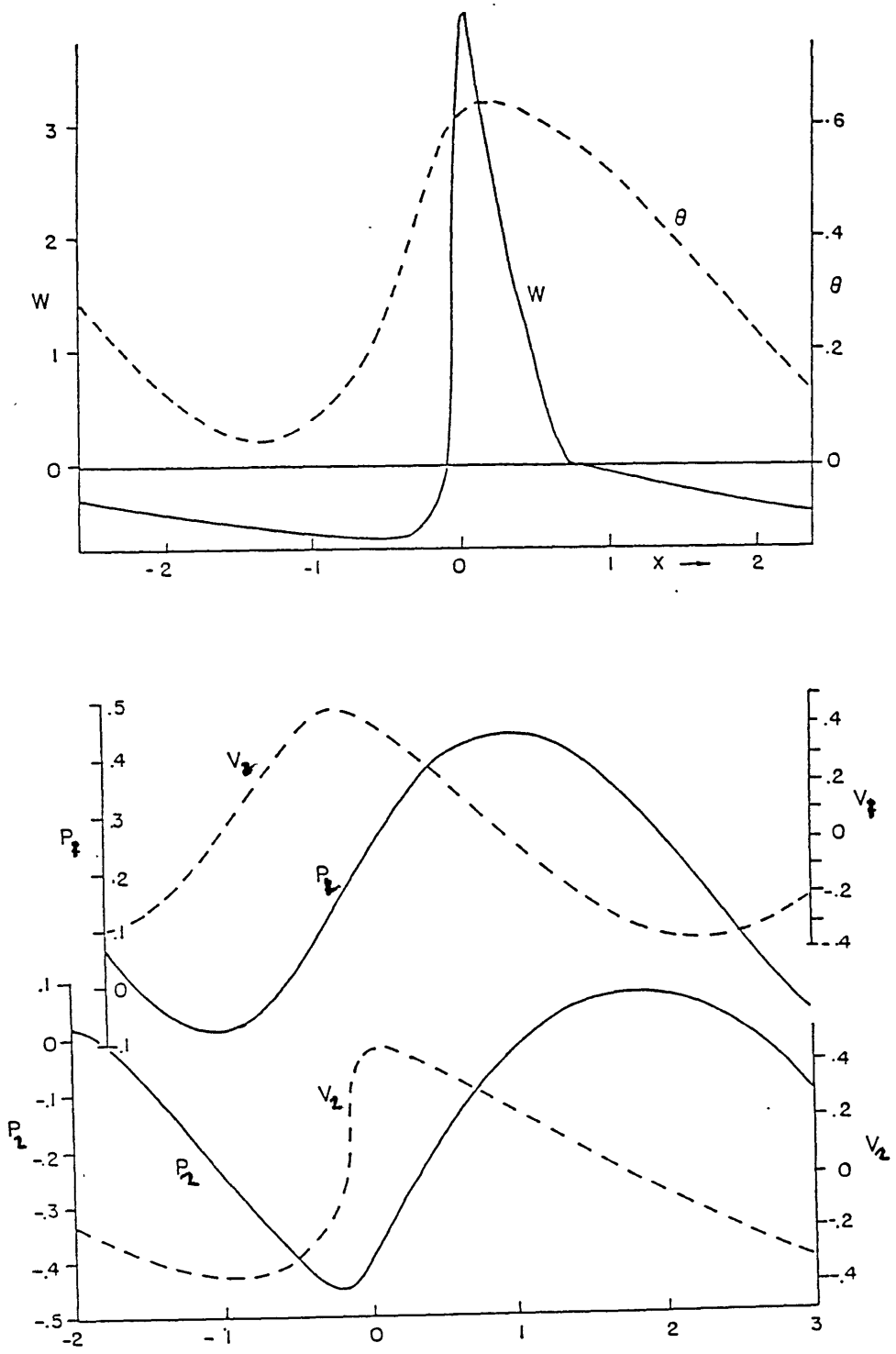


Fig.2.6 - Same as 2.5 but in physical space when the maximum low-level vorticity is $10f_0$

2.2

In this section we reformulate the 2-level model from the primitive equations. The motivations for this step have been discussed at the end of the previous section. The model is now linearized, because there is no transformation comparable to the 'geostrophic coordinates' for the PE (*). The equations for small 2D perturbations to an Eady basic state are

$$\begin{cases} (\partial_t + \bar{u}\partial_x) u_a - f_0 v_a + \bar{u}_z w = 0 \\ (\partial_t + \bar{u}\partial_x)(v_g + v_a) + f_0 u_a = 0 \\ (\partial_t + \bar{u}\partial_x)\theta + w\bar{\theta}_z + (v_g + v_a)\bar{\theta}_y = 0 \\ u_{ax} + w_z = 0 \\ \theta_x = \dfrac{f_0 \theta_0}{g} v_{gz} \end{cases} \qquad (2.25)$$

as in the preceding section $\bar{\theta}_y = -f_0(\theta_0/g)\bar{u}_z = \text{const.}$ and $u_a = -\psi_z$, $w = \psi_x$. Therefore the x-momentum equation becomes

$$-(\partial_t + \bar{u}\partial_x)\psi_z - f_0 v_a + \bar{u}_z \psi_x = 0 \qquad (2.26)$$

(*) The transformation $X = x + v/f_0$, $Y = y - \bar{u}/f_0$ would take care of the y-momentum and thermodynamic equations in the same way as (2.8) does in the GM approximation. The thermal wind and the x-momentum equations however assume a very complex form under this transformation.

that we solve for v_a

$$v_a = \frac{\bar{u}_z}{f_0}\psi_x - \frac{1}{f_0}(\partial_t + \bar{u}\partial_x)\psi_z \qquad (2.27)$$

then

$$\begin{cases} (\partial_t + \bar{u}\partial_x)v_g - f_0\psi_z = (\partial_t + \bar{u}\partial_x)^2\frac{\psi_z}{f_0} - (\partial_t + \bar{u}\partial_x)\frac{\bar{u}_z}{f_0}\psi_x \\ (\partial_t + \bar{u}\partial_x)\theta + \psi_x\left(\bar{\theta}_z + \frac{\bar{u}_z\bar{\theta}_y}{f_0}\right) + v_g\bar{\theta}_y = (\partial_t + \bar{u}\partial_x)\frac{\bar{\theta}_y}{f_0}\psi_z \end{cases} \qquad (2.28)$$

are the counterparts of (2.3) and (2.5) respectively, and the terms written on the r.h.s. are those missing in the GM approximation.

From these two equations we can derive, for the continuous model, an equation for ψ

$$(\sigma + \bar{u}\partial_x)^3\frac{\psi_{zz}}{f_0} + (\sigma + \bar{u}\partial_x)f_0\psi_{zz} + \frac{N^2}{f_0}(\sigma + \bar{u}\partial_x)\psi_{xx} - 2\bar{u}_z f_0\psi_{xz} = 0 \qquad (2.29)$$

(compare Eady, 1949). The corresponding GM equation is

$$(\sigma + \bar{u}\partial_x)f_0\psi_{zz} + \frac{N^2 - \bar{u}_z^2}{f_0}(\sigma + \bar{u}\partial_x)\psi_{xx} - 2\bar{u}_z f_0\psi_{xz} = 0$$

in which $\bar{q}_d = \frac{f_0}{g}(N^2 - \bar{u}_z^2)$ appears as a stability parameter in place of N^2.

The two-level discretisation is done as in the preceding section: this implies $\psi_z = 0$ at mid-level. Therefore the thermodynamic equation assumes the same form as in GM. However, the cancellation of the $\bar{u}_z^2$ in the stability parameter comes not from this term but from the $(\partial_t + \bar{u}\partial_x)\frac{\bar{u}_z}{f_0}\psi_x$ in the momentum equation and we are then preserving this charachteristic of the continuous PE system in the 2-level, as we

will see from (2.32) below.

Using again $\bar{u}_z = 2\bar{u}/h$ we have

$$\begin{cases} (\sigma+\bar{u}\partial_x)v_1 + (\sigma+\bar{u}\partial_x)\dfrac{\bar{u}}{f_0 h}\psi_x + (\sigma+\bar{u}\partial_x)^2\dfrac{\psi}{h f_0} + \dfrac{f_0\psi}{h} = 0 \\ (\sigma-\bar{u}\partial_x)v_2 + (\sigma-\bar{u}\partial_x)\dfrac{\bar{u}}{f_0 h}\psi_x - (\sigma-\bar{u}\partial_x)^2\dfrac{\psi}{h f_0} - \dfrac{f_0\psi}{h} = 0 \\ \sigma\theta + \dfrac{\theta_0}{f_0}q\psi_x - \dfrac{f_0\theta_0}{g}\dfrac{\bar{u}}{h}(v_1+v_2) = 0 \\ \theta_x - \dfrac{f_0\theta_0}{g}\dfrac{v_1-v_2}{h} = 0 \end{cases} \qquad (2.30)$$

where $q = \dfrac{f_0}{g}(N^2 - \bar{u}_z^2)$.

With the same scaling as in sect 2.1, and defining $R_0 = \dfrac{2\bar{u}}{h\sqrt{g q_d}/f_0}$

$$\begin{cases} (\sigma+\partial_x)v_1 + \dfrac{R_0^2}{2}\psi_{xxx} + \dfrac{3}{4}\sigma R_0^2\psi_x + \left(\dfrac{1}{4}R_0^2\sigma^2+1\right)\psi = 0 \\ (\sigma-\partial_x)v_2 - \dfrac{R_0^2}{2}\psi_{xxx} + \dfrac{3}{4}\sigma R_0^2\psi_x - \left(\dfrac{1}{4}R_0^2\sigma^2+1\right)\psi = 0 \\ \sigma\theta - (v_1+v_2) + q\psi_x = 0 \\ \theta_x = v_1 - v_2 \end{cases} \qquad (2.31)$$

and an equation for ψ can be derived as

$$(q+4R_0^2)\psi_{xxxx} + (2-\sigma^2 q - \tfrac{3}{2}R_0^2\sigma^2)\psi_{xx} + 2\sigma^2(1+\tfrac{1}{4}R_0^2\sigma^2)\psi = 0 \qquad (2.32)$$

with the ~~total~~ geostrophic ~~$v_g + v_a$~~ wind field given by

$$\begin{cases} 2\sigma(v_1-v_2) + (q+R_0^2)\psi_{xxx} + 2\left(\dfrac{1}{4}R_0^2\sigma^2+1\right)\psi = 0 \\ 2\sigma^2(v_1+v_2) - (q+R_0^2)\psi_{xxxx} + 2\left(\dfrac{5}{4}R_0^2\sigma^2-1\right)\psi = 0 \end{cases} \qquad (2.33)$$

The term $q+Ro^2$ in (2.32) is the non-dimensionalisation of $\bar{q}+\bar{u}_z^2=N^2$. We use q explicitly for comparision with the results of the preceding section, while a formulation with $Ri \equiv N^2/\bar{u}_z^2$ would be more appropriate to compare with other non-geostrophic baroclinic instability studies (e.g. Stone,1966). In the latter formulation we would have the Richardson numbers in the two regions, say Ri_1 and Ri_2, as non-dimensional parameters; here we use $r=(Ri_1-1)/(Ri_2-1)$ and $Ro=1/\sqrt{Ri_2-1}$. The -1 in the radicand allows us to recover the GM approximation by letting $Ro^2 \to 0$ at fixed r (see Appendix 2.C). When $Ro^2 \neq 0$ the limit $r \to 0$ is not singular any longer: in fact we can find solutions for all $r > -Ro^2$ i.e for $Ri_1 > 0$. We can therefore examine the behavior of baroclinic waves in a saturated environment even when the lapse rate is conditionally symmetrically unstable, as long as it is not vertically unstable. We are not, however, studying symmetric instability; we will use a finite but small Ro, so that the dry region is always stable to symmetric perturbations - also note that the definition of Ro won't allow $Ri_2 < 1$; moreover we only consider perturbations of infinite meridional extent, so, even in region 1, where symmetric instability is possible, we only consider modes on the 'baroclinic axis' in the terminology of Stone,1966.

The same arguments used in Appendix 2.A lead to the interface conditions $\psi_x = 0$ and the quantities

$$\psi_1 \quad (q+Ro^2)\psi_{xx} \quad , (q+Ro^2)\psi_{xxx}$$

being the same at the two sides of the interfaces. Everything then

proceeds as in sect. 2.1 with the exception that we cannot prove that σ^2 is real. It is however found to be real by the numerical calculations (see Appendix 2.D).

Table 2.2 shows the behavior of σ and λ at $L_2 = 1.8$ for various values of r and Ro. Recall that Ro = 0 is the GM model presented in sect. 2.1. It is apparent that the growth rate decreases with Ro, while the updraft becomes larger. This behavior can be understood if we consider that the stability parameter here is again N^2, which then appears both in the time scale and the length scale for the most unstable mode, and increasing the Rossby number (i.e. the shear) at fixed q, actually increases the BV frequency.

When going into the negative r region the g.r. increases again as seen in fig 2.7. The relevance of the 'negative r' solutions is not obvious. The hypothesis on which this work rests is that the time the system spends in a $q<0$ state is much shorter than the time scale of synoptic scale motions. While this is certainly true of $N^2<0$ states, the typical doubling time of symmetric instability is of the order of a few hours (e.g. Bennetts and Hoskins,1979) and this is strictly not 'much shorter than' the time scale of explosive cyclones which, in extreme cases may double in intensity on the order of twelve hours. Therefore it is conceivable that the developing cyclone will, at some time during its growth, have to deal with an environment of slight instability to slantwise convection, especially since the stability parameter q is itself a conserved quantity that can be modified by diabatic or frictional processes only (in a saturated environment).

TABLE 2.2

σ r :	-.08	-.05	-.03	-.01	0.	.01	.1	.5	1.
Ro									
0.	---	---	---	---	(1.41)	1.24	.94	.69	.58
.02	---	---	---	---	1.26	1.23	.94	.69	.58
.1	---	---	---	---	1.23	1.15	.92	.69	.58
.2	---	---	1.19	1.08	1.04	1.01	.87	.67	.57
.3	1.14	1.00	.95	.92	.90	.89	.80	.64	.56

λ r :	-.08	-.05	-.03	-.01	0.	.01	.1	.5	1.
Ro									
0.	---	---	---	---	(0.0)	.07	.24	.63	1.
.02	---	---	---	---	.06	.07	.24	.63	1.
.1	---	---	---	---	.07	.10	.25	.64	1.
.2	---	---	.07	.12	.14	.16	.29	.65	1.
.3	.07	.14	.18	.21	.22	.24	.34	.67	1.

This model does not allow the base state to vary with time on the scale of the perturbation or shorter and so the solutions at negative r do not necessarily represent the behavior of the system when a 'slow' adjustment is taking place. However, the simple fact that the trend to higher growth rates and narrower updrafts continues beyond r = 0 may strengthen our hope that no major qualitative changes occur in that instance. The numerical simulations presented in the next section will confirm this assumption.

The sensitivity of the system is greater near the singular point, so that a change in Ro at r = 0 produces dramatic changes in the eigenvalues, while a similar change at r = .1 has little consequences (see fig. 2.8). Note that the stability parameter is $q + Ro^2$ but q and Ro appear in different combinations in the other coefficients of (2.32), so the PE solutions are not simply a translation in parameter space.

The cut-off wavelength appears to be independent of r, as it was in GM (see fig.2.3) but it depends on Ro. We can derive an analytic expression for this from the r = 1 case. Assuming plane wave solutions and setting $\sigma = 0$ in (2.32) we get $k^2 = 2/(1+Ro^2)$ or $L_2 = \frac{\pi}{2k} = \frac{\pi}{2}\left(\frac{1+Ro^2}{2}\right)^{1/2}$. Table 2.3 gives the values of the cut-off L2 for the Rossby numbers shown in fig. 2.8

This further, although weak, destabilisation of the short waves by reducing Ro can also be seen in fig.2.8. The Rossby number at constant q is proportional to the vertical wind shear so that an increase in

non-dimensional σ for longer waves is easily offset by the smaller scale factor for time. Only the shortest waves, whose σ increases by a large factor (especially those that go from $\sigma \simeq 0$ to a finite value) actually show a larger dimensional growth rate when the Rossby number is reduced

T A B L E 2.3

Ro	cut-off L2
0.	1.1107
.1	1.1163
.2	1.1327
.3	1.1596

This effect is entirely due to keeping q_d constant and changing the shear, which implies a change in the Brunt - Vaisala frequency. The dimensional cut-off L_2 is $(\pi/2\sqrt{2})(hN/f_o)$ and does not depend explicitly on the shear, except in the sense that the BV frequency of a base state with constant potential vorticity increases with increasing vertical shear (*).

As in the GM case of sect. 2.1 there is however a 'true' destabilisation of short waves when the width of the updraft decreases as we move closer to the singularity. Table 2.4 shows L_{TOT} for the

marginally stable wave at two values of r.

From the preceding discussion it is fairly obvious that the natural scales to use with the PE are those defined with N^2 and not with q. In this model we insist on the use of potential vorticity because we want to study the behavior of baroclinic waves in a conditionally symmetrically neutral environment, which is most easily identified by its equivalent potential vorticity rather than by a

---

(*) To accompany this there is a slight shift of the most unstable wave to larger L_2 as Ro increases - both these effects can be understood in terms of the simplest heuristic model of baroclinic instability. The slope of the isentropes in the meridional plane is $f_0 \bar{u}_z / N^2 = f_0 Ro / N$ and the slope of the trajectories of the perturbations (at small enough Ro) is $\sim \frac{H}{L} Ro$. When the Rossby number (i.e. the vertical shear) is increased at fixed N the secondary circulation is reinforced by the same amount as the slope of the isentropes, because $\frac{H}{L} \sim \frac{f_0}{N}$, so that the wedge of instability is unchanged from the 'parcel' point of view. Here we increase Ro at fixed q - in this case the slope of the trajectories is still $\frac{H}{L} Ro \sim \frac{f_0}{\sqrt{q}} Ro$ (with the appropriate definition of Ro) but that of the isentropes goes as $\frac{f_0}{\sqrt{q}} \frac{Ro}{1+Ro^2}$, which is always less than the former. Therefore the wedge of instability is effectively reduced as Ro increases. This takes some of the shortest waves, whose trajectories are closer to the maximum allowed slope, outside the unstable region. It also reduces the most unstable slope, that corresponds then to longer waves.

combination of static stability and vertical shear.

T A B L E 2.4

	Ro	L2	λ	LTOT
r=0.	0.	1.12	0.	1.12
	.1	1.12	.1	1.23
	.2	1.14	.19	1.36
	.3	1.16	.29	1.50
r=.1	0.	1.12	.31	1.47
	.1	1.12	.33	1.49
	.2	1.14	.37	1.56
	.3	1.16	.42	1.65

We now proceed to the next section where we examine how well the two-level model results compare with a (still two dimensional) multi-level PE numerical model.

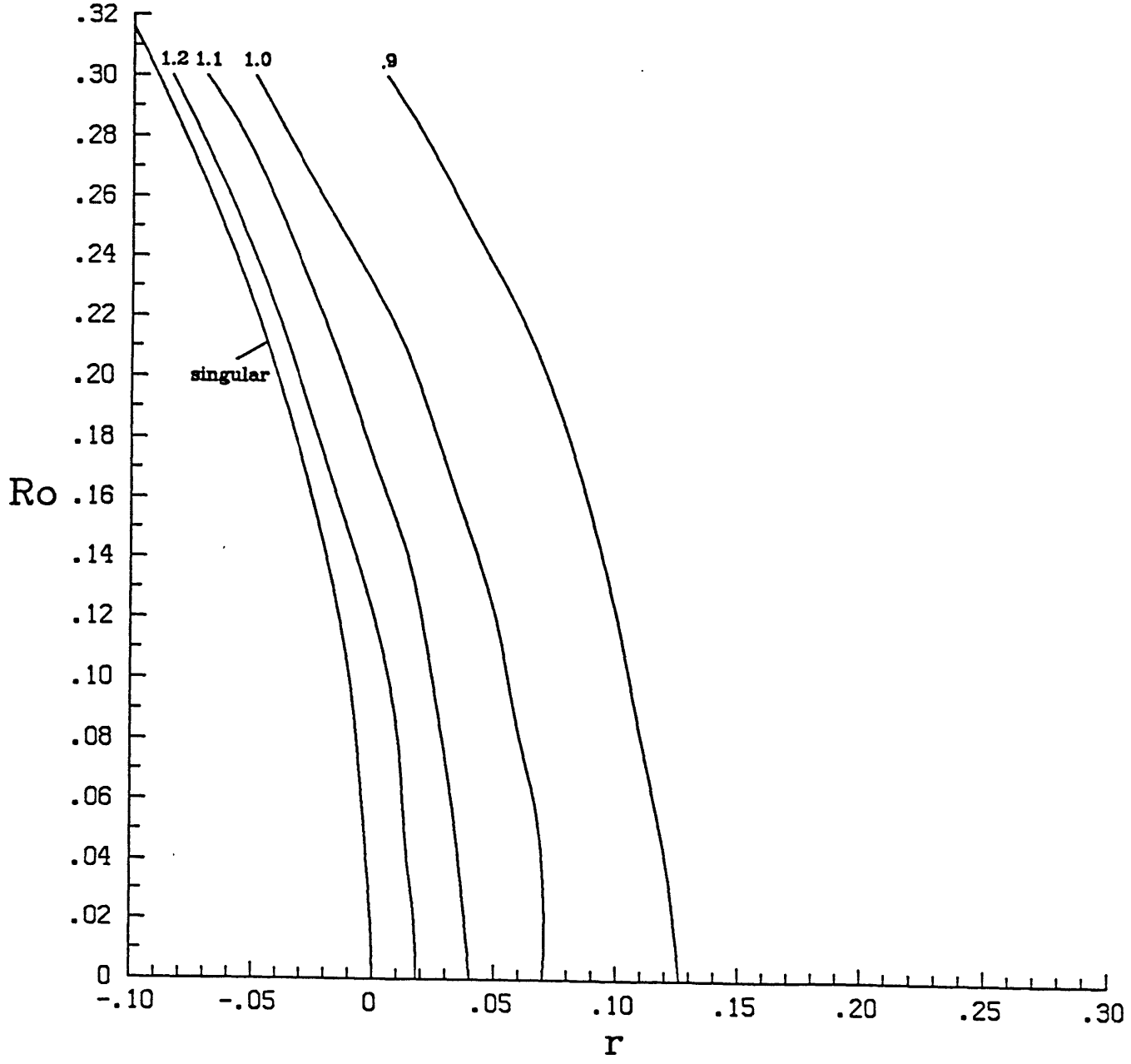


Fig.2.7 - Contours of constant σ on the r - Ro plane for fixed L2 = 1.8

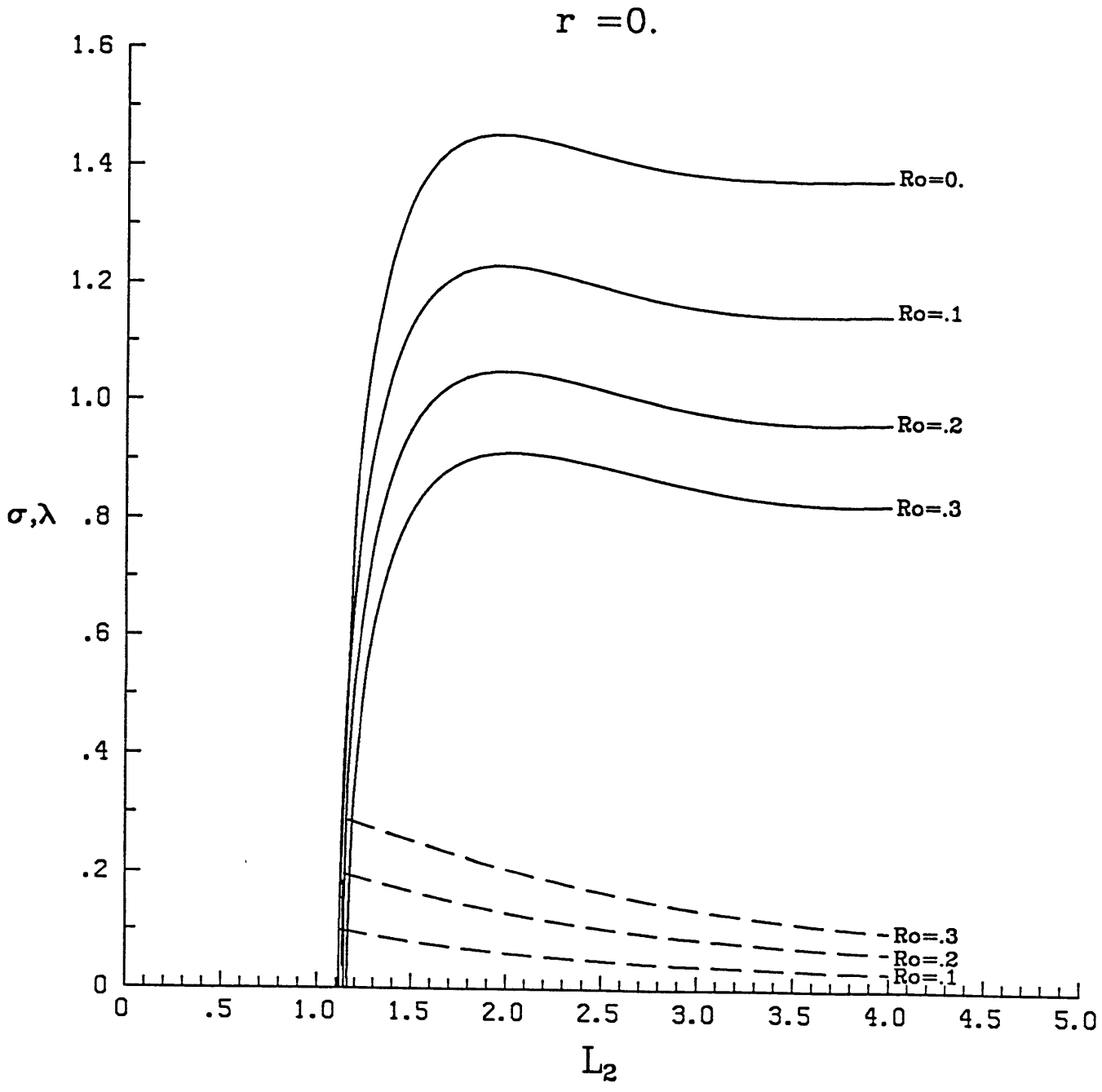


Fig 2.8 a) - Growth rate σ (solid) and ratio of updraft to downdraft width λ (dashed) for various values of Ro at fixed r = 0. Ro = 0 is the GM approximation

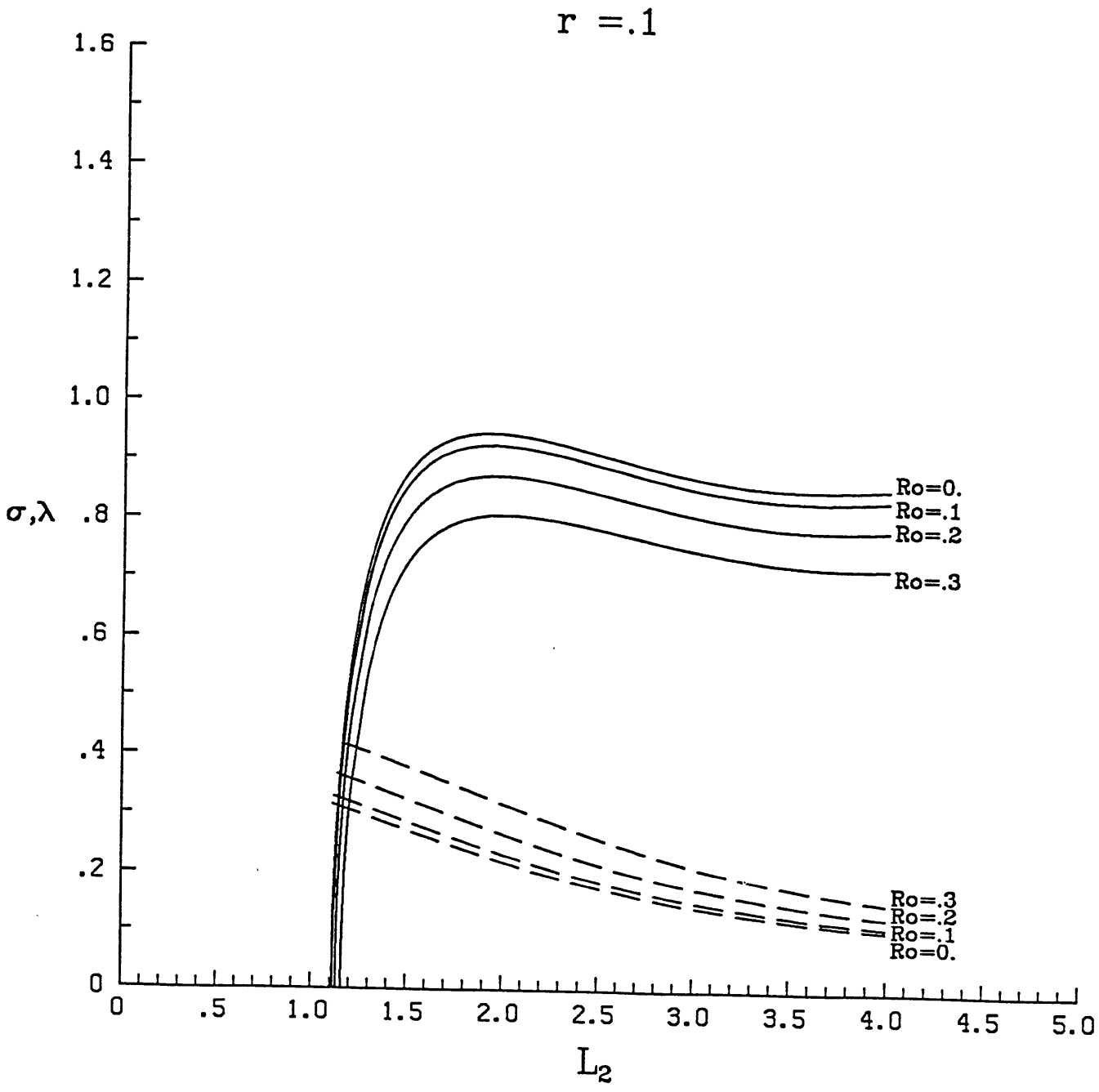


Fig.2.8 b) - same as a) but for r = .1

2.3

In this section we describe the results of numerical experiments performed with a primitive-equation two-dimensional non-hydrostatic model for the purpose of testing the conclusions of the previous sections. The model itself was written by R.Rotunno at NCAR and it is described in Rotunno and Emanuel,1987, where an axisymmetric version of it was used to study tropical cyclones. Only the main characteristics of the model are described here.

The model integrates the PE in a 2-D domain, with a leap-frog time stepping. The compressible terms are integrated separately with a very short time step (1. sec. here) to avoid instabilities due to sound waves, while a longer (20. seconds) time step is used for all other terms (this 'splitting technique' is described in detail in Klemp and Wilhelmson,1978). All experiments are run here in a 10. Km - high troposphere with a rigid lid at the top (*); the boundary condition $w = 0$ is applied at top and bottom, while periodicity is imposed in the x-direction: therefore only waves of the imposed length or its sub-harmonics can grow in the model. The grid has a 1. Km spacing in the vertical; most of the experiments shown in this section have been run with a 50. Km horizontal resolution. Fig. 2.9 (adapted from

---

(*) The option of a sponge layer at the top boundary for the absorption of gravity waves was available in the model but we did not use it because it would also deform the base state wind profile and make comparision with the 2-level and the Eady models more difficult.

Rotunno and Emanuel,1987) shows the arrangement of the variables on the grid. The thermodynamic variables and v are calculated at the same points: there are N=10 points in the vertical, the first one being at 500. m height and the last one at 9,500 m. The vertical velocity w is known at N+1 points displaced half a grid length in the vertical - the first and last of these are on the boundaries and are set equal to zero. The zonal velocity u is known at points at the same height as v, but displaced horizontally half a grid length. Originally the model integrated seven equations for the variables $u, v, w, \theta, \pi, q_v, q_\ell$ (π =Exner) but we did not use the equation for liquid water - when q_v is above saturation condensation occurs and latent heat is added to the θ equation, but we do not keep track of q_ℓ and do not allow re-evaporation. This is done, once again, to make comparision with analytic models more direct.

A linearized saturation law for water vapor is assumed for the following reason. When there is no moisture the only variable that depends on the meridional coordinate is $\bar{\theta}$: we can easily compute $\bar{\theta}_y$ from the thermal wind, and it is uniform in space, so the perturbations remain y-independent if they are such at the initial time. The equation for q_v , however, includes a term $v\bar{q}_{v_y}$. The use of any realistic saturation law gives, for a linearly varying potential temperature $\bar{\theta}_y y$, a highly non-linear behavior of $\bar{q}_v$. Since we cannot keep track of the meridional variation of $\bar{q}_{v_y}$ we are forced to use its value at t=0 for all times. It is easy to see how this leads rapidly to the advection of very high values of moisture in the region

of southerly wind, and of negative values of q_v in the northerly wind. To delay as much as possible the occurrence of this unphysical event we use a linearized $q_{vs} = q_{v_0} + b\bar{\pi}\theta$, where the two coefficients are chosen to give a reasonable value of q_{vs} at the surface (25. g/Kg at 300 K) and a small enough meridional gradient that no negative moisture is advected during the integration. Since we always start the integration with a very small meridional wind perturbation this value is not exceedingly small. We finally choose $q_{v_0} = -.035$ and $b = .2 \cdot 10^{-3}$, which give a $\bar{q}_{v_y}$ of approximately $-1.8 \cdot 10^{-9}\ m^{-1}$ at the surface, and slightly decreasing with height. The dependence of $\bar{q}_{v_y}$ on z would of course imply a y-dependence of $\bar{q}_{v_z}$, that we ignore. The values of the thermodynamic variables for a typical run are given in table 2.5. $\bar{q}_v$ is obviously too high in the upper troposphere, but its absolute value is of little importance - we always run the model for an initially saturated atmosphere, so that supersaturation occurs anywhere there is ascent, and only the derivatives count in the advection terms.

When a grid point is supersaturated after advective and diffusive terms have been computed condensation occurs, and heat and moisture are recalculated isobarically from

$$\Delta\theta = -\frac{L}{c_p\bar{\pi}}\Delta q_v \qquad ; \qquad q_v + \Delta q_v = q_{sat}(\vartheta + \Delta\theta, \bar{\pi})$$

The model of Rotunno and Emanuel,1987 used a more sophisticated scheme (Soong and Ogura,1973) but our saturation law is already idealized enough that we do not worry about this order of inaccuracy.

Turbulence representation is as in Mason and Sykes,1982. Vertical diffusion is switched on only when the Richardson number goes below 1. and eddy viscosity is then

$$\nu = \ell_v^2 \sqrt{1-Ri}\left\{(u_x^2+w_z^2)+(u_z+w_x)^2+v_x^2+v_z^2\right\}^{1/2}$$

where ℓ_v is a vertical mixing length that is here taken equal to 200. m. Horizontal eddy viscosity is

$$\nu_H = \ell_H^2\left\{u_x^2+v_x^2\right\}^{1/2}$$

We experimented with various values of ℓ_H to produce reasonably smooth fields without altering the overall picture and finally chose $\ell_H = \Delta x$, the horizontal grid spacing. Table 2.6 gives a list of the values of the model parameters.

The base state is designed to have uniform equivalent potential vorticity. We choose a constant shear and a surface temperature; the Boussinesq hydrostatic equation is then integrated (from $\pi_0 = 1$)

$$\pi_j = \pi_{j-1} - \frac{g}{c_p}\frac{\Delta z}{\theta_0} \qquad j = 1,2,\ldots,N$$

to give pressure at all levels. Finally θ is obtained from

$$q_e^* f_0 = \bar{u}_z\left(\bar{\theta}_y + \frac{L}{c_p\bar{\pi}}\bar{q}_{vy}\right) + f_0\left(\bar{\theta}_z + \frac{L}{c_p\bar{\pi}}\bar{q}_{vz}\right) \;;\; q_e^* = q_e\theta_0/f_0$$

which gives

$$\theta_j\left(1-\frac{c}{\pi_j}\right) = \left(1-\frac{c}{\pi_{j-1}}\right)\theta_{j-1} + \frac{(\Delta w)^2}{\Delta z}\frac{\theta_0}{g} + \frac{q_e^*\,\Delta z}{\left(1+\frac{L}{c_p}b\right)}$$

with

$$c \equiv \frac{L g b \Delta z}{2 c_p^2 \theta_0 \left(1+\frac{L}{c_p}b\right)}$$

Table 2.7 summarizes the major characteristics of the experiments presented in this section. All the fields are displayed as seen from a reference frame that moves with the base wind at mid-level. w is averaged vertically, and u horizontally, to be shown on the same points as the other variables. Consequently w does not appear to go to zero at the top and bottom of the graphs because those are not the top and bottom of the model.

Fig. 2.10 shows u, v, w, θ at various times for experiment A0. This is a dry run that we show for comparision with the saturated experiments. The dimensional wavelength is 4,000 Km and the average potential vorticity

$$q_d = \frac{(\vec{\nabla} \times \vec{u} + f_0 \hat{k}) \cdot \vec{\nabla}\theta}{\theta_0}$$

is $.1407 \cdot 10^{-8}\ m^{-1} s^{-1}$ (*) We design the basic state for uniform q_e, which means that q_d is not uniform, because the gradients of q_v vary with height. The value at the top is $.17 \cdot 10^{-8}$ and the value at the surface $.12 \cdot 10^{-8}$. The domain average is also the value of q_d at mid-level that we use for scaling purposes to compare with the 2-level. With this q_d the non dimensional length of the channel is 6.81, or $L_2 = 1.70$ in the notation of the preceding sections. For this r and L_2 the 2-L SG eigenvalue is $\sigma_{SG} = .586$ or $.074 \cdot 10^{-4}\ s^{-1}$; the vertical shear

---

(*) The model uses dimensional variables. All quantities in this section are dimensional, unless otherwise explicitly noted, and in MKS units.

is $.3 \cdot 10^{-3} s^{-1}$, which gives a Ro = .255; then the 2-L PE eigenvalue is $\sigma_{PE} = .566$ or $.073 \cdot 10^{-4} s^{-1}$. Fig 2.11 shows the time series of growth rate evaluated from the domain-integrated kinetic energy of the perturbation, every hour, during the time integration. The initial condition for this run is

$$v = v_0 \sin\left(2\pi\left(\frac{x}{L_{TOT}} + \frac{1}{2}\frac{z}{H}\right)\right)$$

i.e. a wave with a westward tilt of π radians between surface and top. v_0 is 1. m/s and pressure and θ fields are geostrophically balanced to this v, while w and u' are equal to zero. This induces a potential vorticity perturbation of order $10^{-12} m^{-1} s^{-1}$, i.e. three orders of magnitude smaller than the base state. As it can be seen in fig. 2.11 the system takes a few hours to readjust to the most unstable Eady mode and then settles to a very steady behavior, with growth rate that is not far from the one predicted by the 2-L PE model of sect 2.2, indicated by the lower straight horizontal line (the other being the 2-L SG growth rate from sect.2.1), the difference being very likely due in large part to the presence of dissipation in the numerical model. The average growth rate of A0 between 100. and 150. hours is $.069 \cdot 10^{-4}$ which corresponds to an e-folding time of approx. 40. hours. We initialize the run with a very small perturbation and by the end of the integration only a slight decline of the growth rate is observed. Examination of Fig.2.10 shows that the structure of the solution closely resembles the most unstable Eady wave with the frontogenetical effects included in semi geostrophic theory. The small asymmetry between top and bottom boundaries is due to non-uniform N^2, while the

asymmetry between northerly and southerly winds at either boundary is a proper effect of ageostrophic advection (S.Garner, personal communication).

Exp. A1 is a replica of A0 in a saturated atmosphere. The base state has r=0., i.e. it is neutral to slantwise convection. All other parameters are as in A0. Fig 2.12 shows the adjustment to the moist normal mode taking place in the first 50. hrs. During this time the growth rate undergoes large oscillations as was the case for A0 readjusting to a dry normal mode. For the non dimensional L_{TOT}=6.81, r=0. and Ro=.255 the 2-L PE eigenvalue is σ_{PE}=.92 corresponding to a dimensional $\sigma^* = .118 \cdot 10^{-4} s^{-1}$ which is a little higher than the actual σ^* at 50. hrs ($\cong .112 \cdot 10^{-4}$, corresponding to an e-folding time of 25. hrs). The second eigenvalue is λ=.11 or a dimensional width of the updraft of 396. Km, which is, within the grid resolution, the same as observed. The SG values would be σ_{SG}=1.38 and λ=0. which are of course greatly off mark. As observed in fig.2.12 at this time the surface cold front is already stronger than the upper-level one, but the symmetry of the updraft generates an equally strong negative anomaly of relative vorticity at the top boundary in correspondence to a warm frontal zone. This phase of the evolution stops before the absolute vorticity becomes negative.

As seen in Fig.2.13 the growth rate declines slowly from this time on and the updraft becomes larger, although the form of the solution remains essentially the same until 100. hrs (see fig.2.14). The estimate of growth rate from the L_2 observed at 100. hrs is still

good ($L_2 = 2.72 \rightarrow \sigma_{BE} = .743 \rightarrow \sigma^* = .95 \cdot 10^{-5}$) but $\lambda = .33$ is larger than observed.

The potential vorticity anomaly, in fig.2.15 shows by this time the expected dipole, but very little change at mid level. q_e itself is not exactly conserved (*) but fig.2.15 shows that its change at the mid point of the updraft is very nearly zero. Since the parameters that determine the solution in the 2-level model are unchanged, the successive evolution of the disturbance must be attributed to finite amplitude effects setting in. Indeed the fields between 100. and 150. hrs. (see fig.2.14) begin to resemble the SG solutions in physical space (i.e. of finite amplitude - see sect.2.1) rather than those in geostrophic space (i.e. of small amplitude). The updraft becomes larger, but with a maximum at the western edge, at a lower level than before. The reduced divergence at the top of the updraft makes the upper anticyclonic region become progressively weaker than the cyclonic one, and an upper level cold front begins to develop, well to the rear of the surface front.

Finally we note that the q_e anomaly has become fairly strong by

---

(*) The considerations in Rotunno and Klemp,1985 (Appendix A) apply, but $J(\beta, \theta_e)$ does not remain small in this 2-D model because the base state is allowed to have meridional gradients of θ and q_v, while the perturbation cannot adjust its meridional structure to keep the Jacobian small. With no baroclinicity $\bar{\theta}_y = \bar{q}_{v_y} = 0$ and the problem would not arise.

150. hrs, increasing r in the updraft region, and there is a negative anomaly on the western edge of the updraft, corresponding to a region that would be slantwise convectively unstable (also see θ_e and M fields and recall that there is a meridional θ gradient, so the most unstable symmetric mode is not on the x-z plane) if it were saturated (which is not, see the relative humidity in fig.2.15).

As an additional check on the 'normal mode' nature of this solution we run a similar experiment (A2) with the same base state and random initial condition. A random field of v with values between + and -.01 is generated, and used as initial condition for the model run. The initial amplitude is very small so as not to create a large perturbation to the base state potential vorticity. A longer integration is then required to reach amplitudes similar to A1. The structure of the expected most unstable mode is already present at 200. hrs. (not shown) although superimposed to small scale oscillations that make it difficult to estimate the true width of the main updraft from the w field. As the moist baroclinic mode keeps growing at a regular pace (see growth rate in fig.2.16) the small scale noise is dissipated away, until only a solution of very similar shape to A1 remains. Fig.2.17 shows the end of the integration of A2, when the amplitude is comparable to that of A1 in fig.2.14. Apart from a shift in the horizontal location due to the randomness of the initialization this is virtually indistinguishable from A1.

An experiment similar to A1 but with momentum drag at the surface (labeled A3) was performed to see the effect of this form of dissipation on the growth rate. A momentum flux is applied at the lower boundary with the form

$$F_{(u,v)} = C_D (u,v) \sqrt{u^2+v^2}$$

where $C_D = .004$ (constant) and the zonal wind is only the perturbation field, i.e. it is assumed that $\bar{u}=0$ at the surface but we are looking from a reference frame that moves with the mid-level wind.The growth rate is shown in fig.2.18 together with the growth rate of A1 for comparision, and selected fields are in fig.2.19. Almost nothing new happens until 50. hrs. In the next 50. hrs. the growth begins to slow down but the structure of the solution is essentially unchanged. After 100. hrs. the tendency of the meridional wind to be reduced to zero at the ground can be seen in the graphs (recall that the lowest point shown is at 500. m height) and the θ surfaces are flattened. The updraft becomes larger and more complex than in A1 at the same time and the maximum of w is at an higher level than before. The effect of surface drag on the structure of the low-level front is similar to that described in previous (dry) studies, e.g. Keyser and Anthes,1982.

Fig.2.20 shows the growth rate for exp. B, which has r=.11. In order to get this value of r we have to change the vertical profile of θ, and consequently q_d, which is here $.155 \cdot 10^{-8}$. Precise numbers are given in Table 2.7, and fig.2.20 shows the SG and PE estimates for the growth rate.

Experiment C is back to r=0. but at a lower Rossby number than A1. The vertical shear is reduced to 10. $m\,s^{-1}$ between top and bottom, from 30. $m\,s^{-1}$ as it was in A1. This reduces the Rossby number to .085. Fig.2.21 shows the growth rate. Since the time scale is three times what it was in A1 the evolution is that much slower and by the end of the run the amplitude is still small and the growth rate constant. Fig.2.22 shows v and w at 160.,180.,200. hrs. The 2-L PE gives for the parameter values of C σ_{PE}=1.18 or σ^{*}=.504·10^{-5} and λ =.03. As seen in fig.2.21 σ_{PE} is higher than the numerical value, as it had been for the previous experiments,and λ observed is larger than expected. Both occurrences can probably be attributed to the presence of horizontal diffusion - even so the updraft appears much narrower in the low-Rossby-number environment than it was in exp. A1.

Several runs have been made reducing the wavelength. Fig.2.23 shows the growth rate of a 3,000. Km wave at high Ro number for three different values of r, namely r=.11, r=0., and r=-.07, from the lowest to the highest curve. The negative value corresponds to a vertically neutral saturated atmosphere, i.e. the parameter value for which the 2-L PE model is singular as discussed in the previous section. For all three cases the 2-L PE growth rates compare fairly well with the numerical values at 30. hrs., that is the time when the adjustment is completed and the solution is the linear normal mode of the previous sections. After this time the updraft begins to spread out and the growth to slow down. All during this phase the σ and λ evaluated numerically are consistent with a solution of the 2-L PE of

approximately the right wavelength and increasing r. However the average q_e in the updraft region does not change much during the integration. The observed solution seems to reach the non-linear stage sooner than at longer wavelength.

At even shorter wavelengths the 'destabilisation' of short waves mentioned in sect.2.2 can be seen when Ro is decreased. Fig 2.24 shows the growth rate of exp.H and fig.s 2.25 and 2.26 selected fields for exp.s G and H. Both have a 2,000.Km-long wave and r=0. but differ for the shear. G has high Ro number (.255) and H low Ro number (.085). The latter is unstable and quickly reaches the normal mode form and follows the usual behavior (see fig.2.24). The wave in exp. G is instead neutral. Its initial condition has a westward tilt with height, so we observe a fast 'non-modal' growth in the first few hours (compare Farrell,1982) reaching in 20. hrs. the same amplitude that H has at 50. hrs.; at this stage the vertical tilt is reduced, however, and soon the wave tips over to the other side, looses coherence and decays. An experiment initialized with random noise (not shown) exhibits only a neutral wave after the small scale noise has been dissipated away. Note that for these two experiments the 2-L SG model, which is insensitive to the Ro number, would give the same, unstable, solution.

The model results presented in this section show, as a dominant characteristic, the asymmetry between the upward and downward branches of the secondary circulation, and the effects it induces on the other fields. This behavior, obtained in a model that explicitly resolves convection, is fairly well described by the analytic models of sect.s 2.1 and 2.2, that used the slantwise convective adjustment hypothesis. This suggests that this form of parameterization might be successfully used in other models that attempt simulations of moist baroclinic cyclones. Previous results from models that use alternative parameterization schemes (e.g. CISK, or a latent heat release given by a combination of convective and stable updrafts) fail to show this asymmetry of the circulation (e.g. Nehrkorn,1985 who shows the structure of Eady waves modified by CISK - most of the other studies only discuss the eigenvalues). It is however possible that this aspect of the analytic solution is more a product of the separate treatment of 'dry' and 'moist' regions in the same wave, rather than of the specific parameterisation chosen. To the author's knowledge the only previous works that treat the updraft and downdraft regions separately are by Lilly,1960, who was only concerned with convection 'per se', and not its influence on a baroclinic flow, and Tang and Fichtl, 1983. The latter model has similarities to the one presented here, that have been discussed in the Introduction, and produces two distinct asymmetric modes - one with a narrow updraft and one with a large updraft (*). The lack of selectivity between the two modes is probably due to different matching conditions.

The moist baroclinic modes found up to this point still do not have a growth rate high enough to compare with the observed 'bombs'. Even more important, the spatial structure of the eigensolutions is observed in both land and sea storms, bombs and non-bombs, and so it does not provide a mean to separate the two classes of phenomena.

(*) This result can be understood if we consider that that model only used real wavenumbers. The dispersion relation in that case gives the same value of σ at two different wavelength (e.g. see curve r=1 in Fig.2.3). For a given wavelength in the 'dry' region, and so a given growth rate, there are two wavelength that correspond to the same σ in the dispersion relation for the 'moist' region, one of which is shorter and the other longer than the 'dry' wavelength (recall that when only real wavenumbers are allowed the dispersion relation $\sigma(k)$ is just stretched by a factor $\sqrt{q}$, or N depending on the scaling, in both axis, i.e. $\sqrt{q}\,\sigma_q = \sigma(\sqrt{q}\,k)$)

TABLE 2.5

z (km)	p (mb)	π	θ (K)	$\bar{q}_v$ (g/kg)	T (K)	θ_e (K)
10.	252.0	.675	345.0	11.6	232.8	387.8
9.5	273.9	.691	342.2	12.3	236.4	386.6
8.5	321.8	.723	336.7	13.7	243.6	384.1
7.5	375.5	.756	331.5	15.1	250.6	381.5
6.5	435.2	.789	326.6	16.5	257.5	378.9
5.5	501.3	.821	322.0	17.9	264.3	376.4
4.5	574.4	.854	317.5	19.2	271.0	373.8
3.5	654.8	.886	313.3	20.5	277.6	371.2
2.5	743.0	.919	309.3	21.8	284.1	368.7
1.5	839.3	.952	305.5	23.1	290.6	366.2
.5	944.2	.984	301.8	24.4	296.9	363.7
0.	1000.0	1.00	300.0	25.0	300.0	362.5

T A B L E 2.6

model parameters

ℓ_v	200. m
ℓ_H	50. km
H	10. km
L	variable 4000. km in exp. A1
Δz	1. km
Δx	variable 50. km in exp A1
Δt	20. sec (long) 1. sec (short)
f_o	10^{-4} s^{-1}

T A B L E 2.7

EXP.	r	Ro	wavel. (Km)	σ(2-L) (s^{-1})	λ(2-L)	comments
A0	1.	.255	4,000	.073E-4	1.	dry reference run
A1	0.	"	"	.118E-4	.11	satur. reference run
A2	same as A1 except with random initial condition					
A3	same as A1 except with surface drag					
B	.11	.243	4,000	.099E-4	.23	as A1 but higher q_e
C	0.	.086	"	.051E-4	.03	as A1 but lower vertical shear
D	0.	.255	3,000	.124E-4	.16	shorter wavelength
E	.11	.243	"	.101E-4	.32	as D but higher q_e
F	-.07	.265	"	.138E-4	.10	as D but negative q_e
G	0.	.255	2,000	0.	1.	neutral normal mode
H	0.	.086	"	.053E-4	.06	as G but lower vertical shear

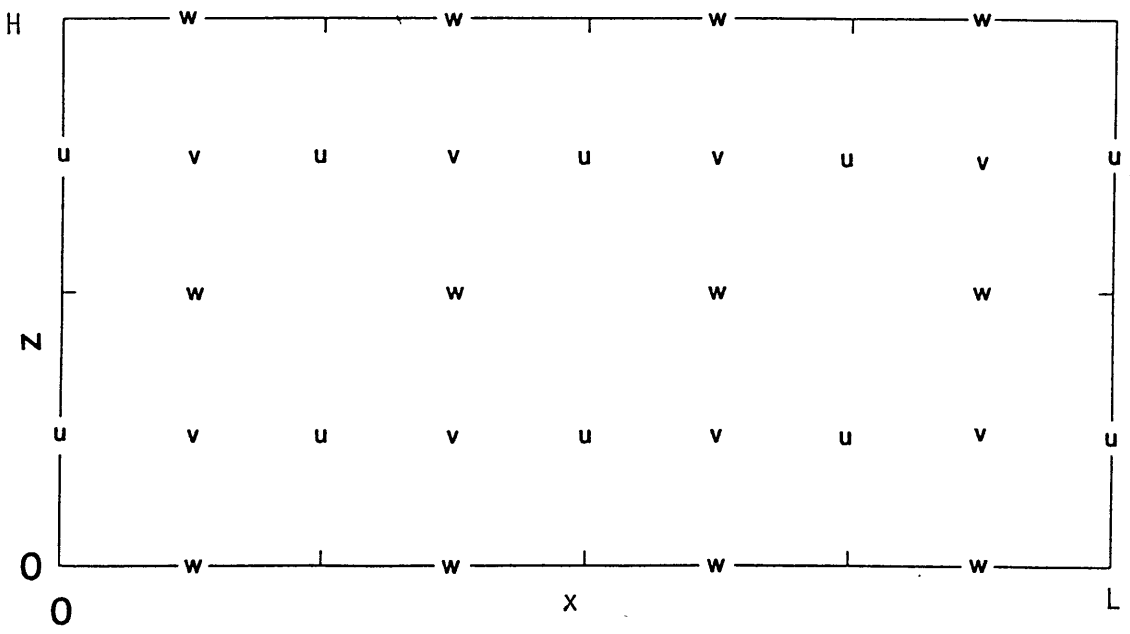


Fig.2.9 - Domain and arrangement of dependent variables on the staggered grid covering the domain. All the thermodynamic variables are located at v points (adapted from Rotunno and Emanuel,1987)

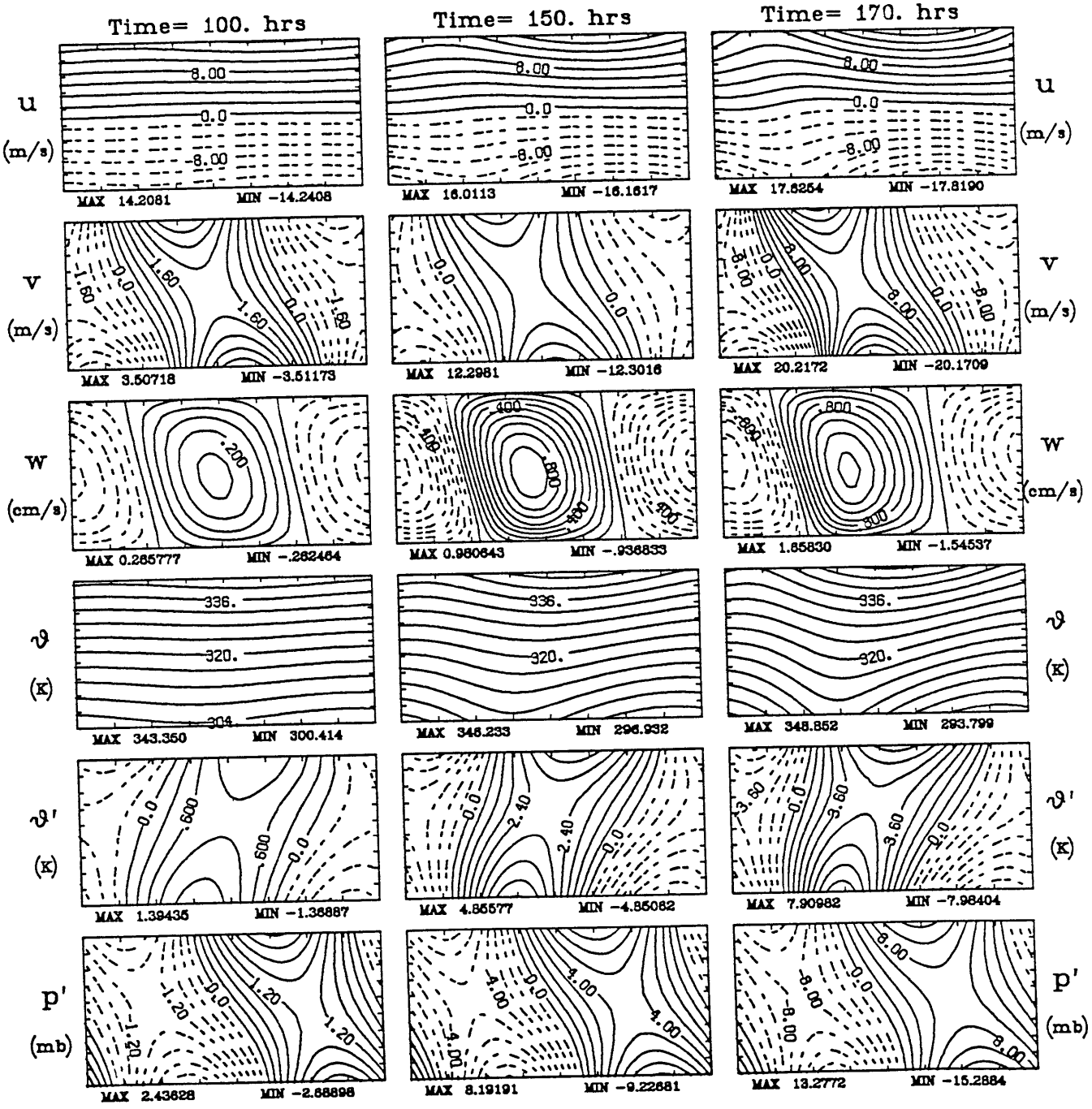


Fig.2.10 - u,v,w, ϑ, ϑ' ,p' fields for exp. A0 at times 100,150,170,180, 190,200 hrs. Note that contour spacing is not the same for perturbation fields at different times

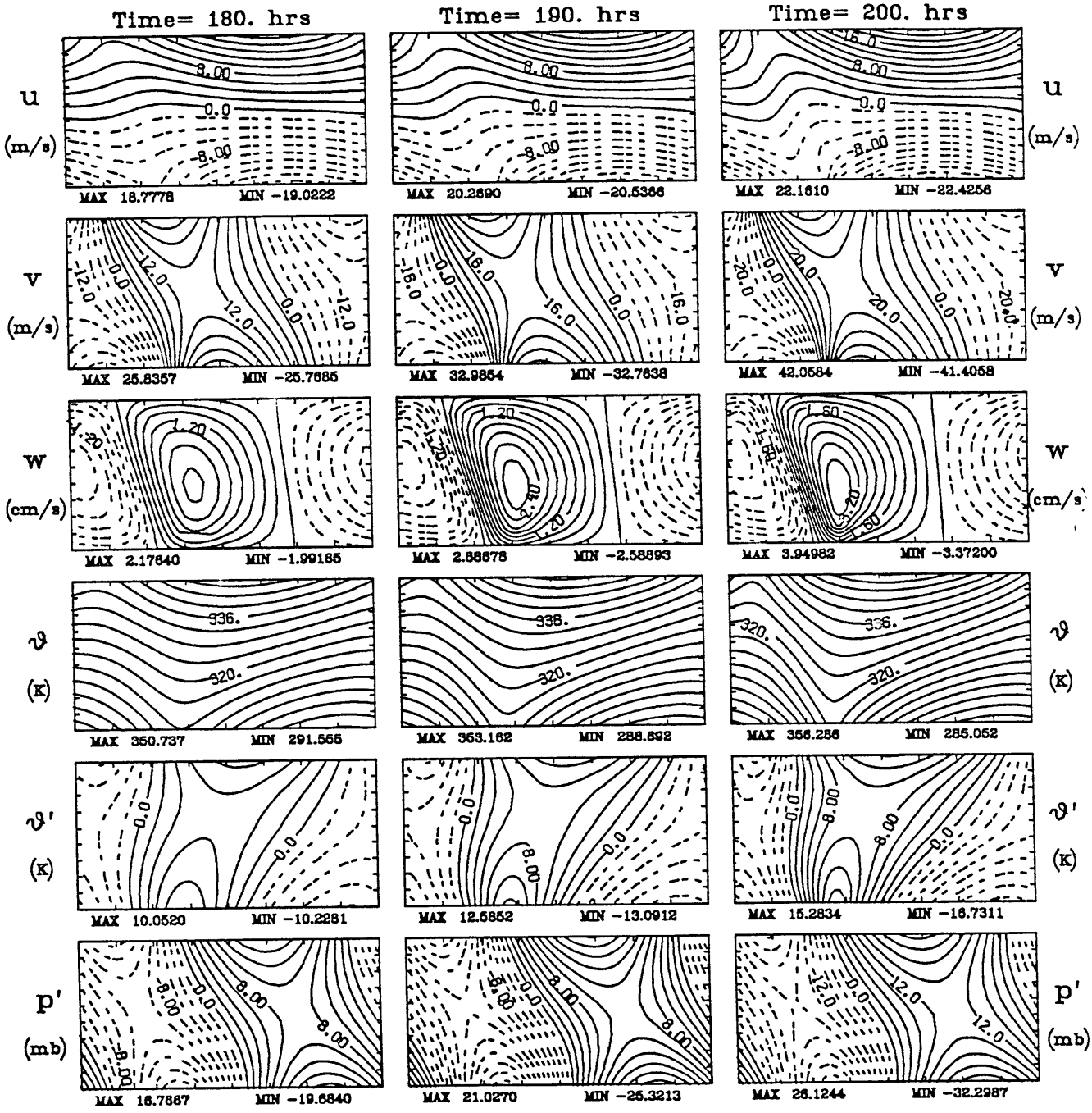

Time= 180. hrs
Time= 190. hrs
Time= 200. hrs
u
(m/s)
MAX 18.7778 MIN -19.0222
MAX 20.2690 MIN -20.5366
MAX 22.1610 MIN -22.4256
v
(m/s)
MAX 25.8357 MIN -25.7685
MAX 32.9854 MIN -32.7638
MAX 42.0584 MIN -41.4058
w
(cm/s)
MAX 2.17640 MIN -1.99185
MAX 2.88678 MIN -2.58693
MAX 3.94982 MIN -3.37200
ϑ
(K)
MAX 350.737 MIN 291.565
MAX 363.162 MIN 288.692
MAX 356.286 MIN 285.052
ϑ'
(K)
MAX 10.0520 MIN -10.2281
MAX 12.5852 MIN -13.0912
MAX 15.2834 MIN -16.7311
p'
(mb)
MAX 18.7867 MIN -19.6840
MAX 21.0270 MIN -25.3213
MAX 28.1244 MIN -32.2987

Fig. 2.10 (cont.)

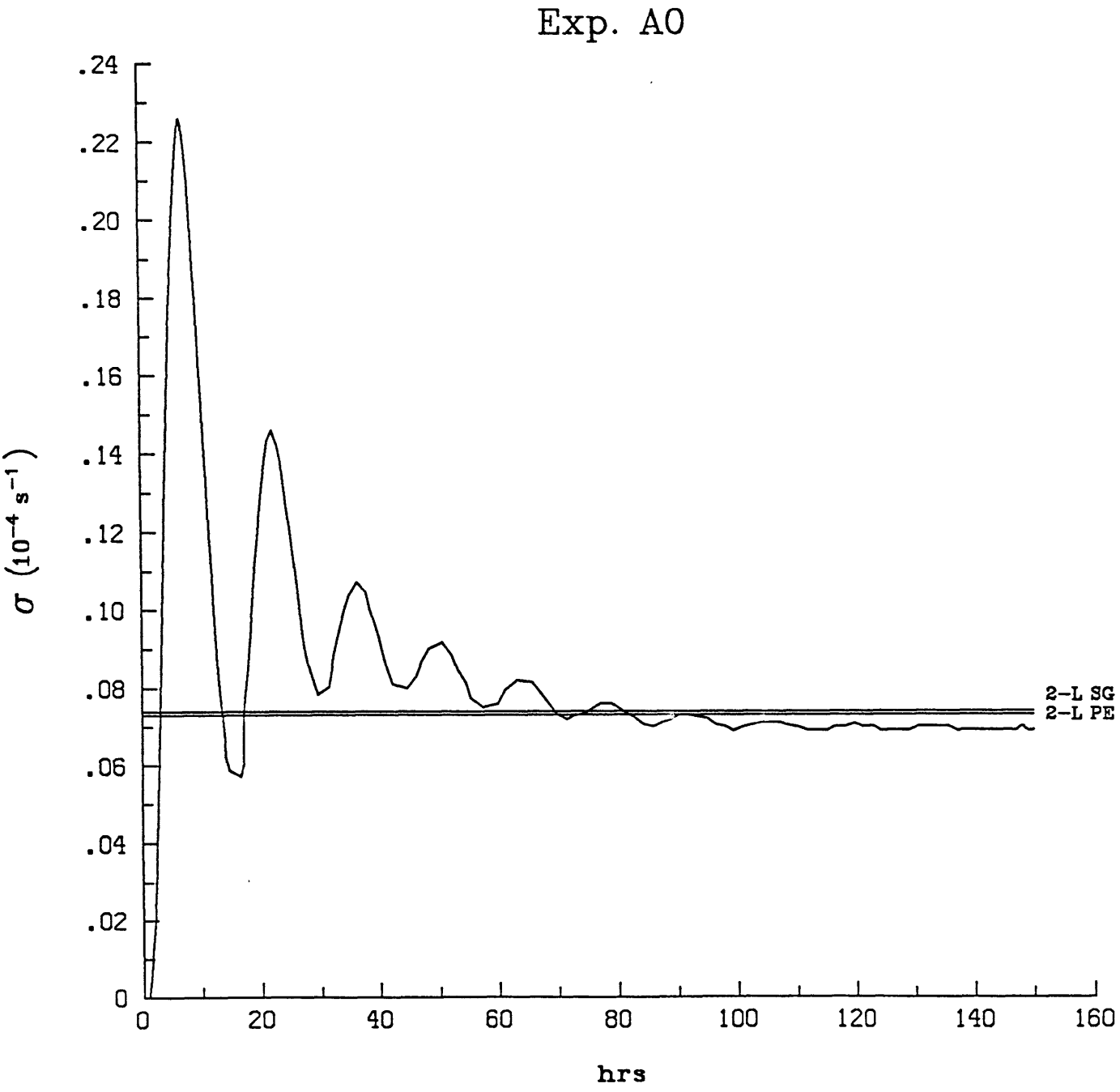


Fig.2.11 - Growth rate σ vs. time for exp. A0 and for the two-level analytic models with the same parameters as A0

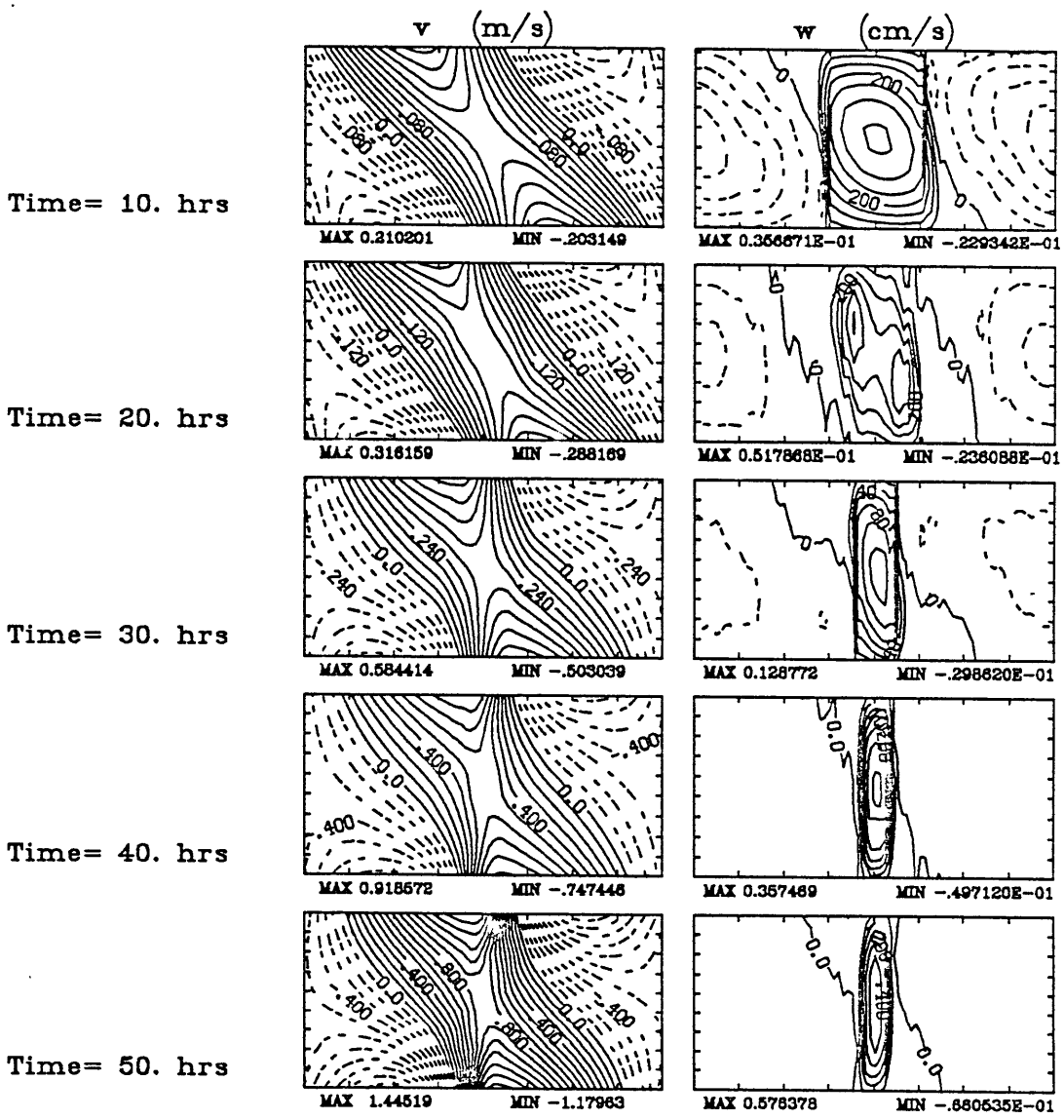


Fig.2.12 - v and w fields for exp. A1 from 10 to 50 hrs

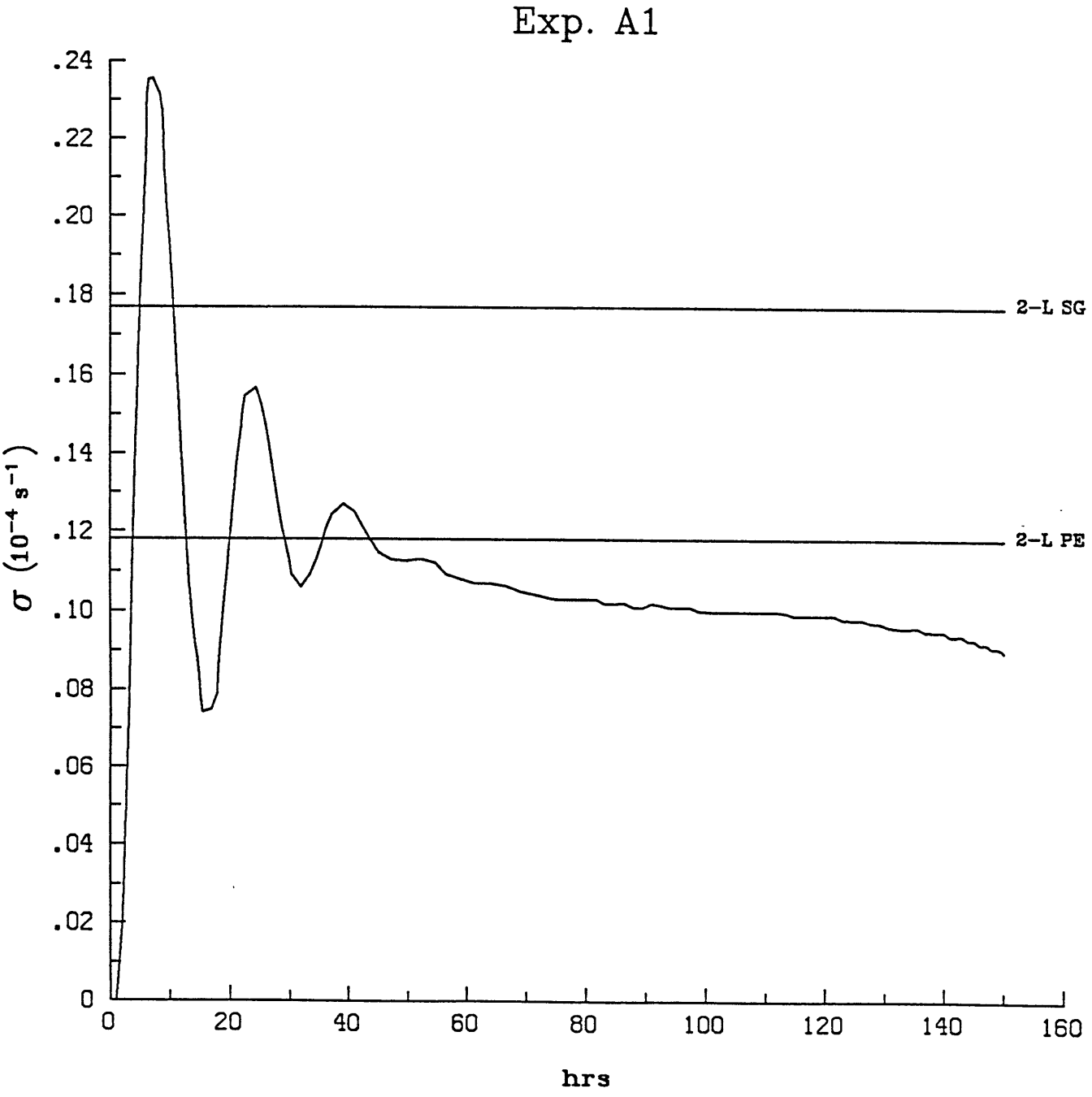


Fig.2.13 - same as 2.11 but for exp. A1

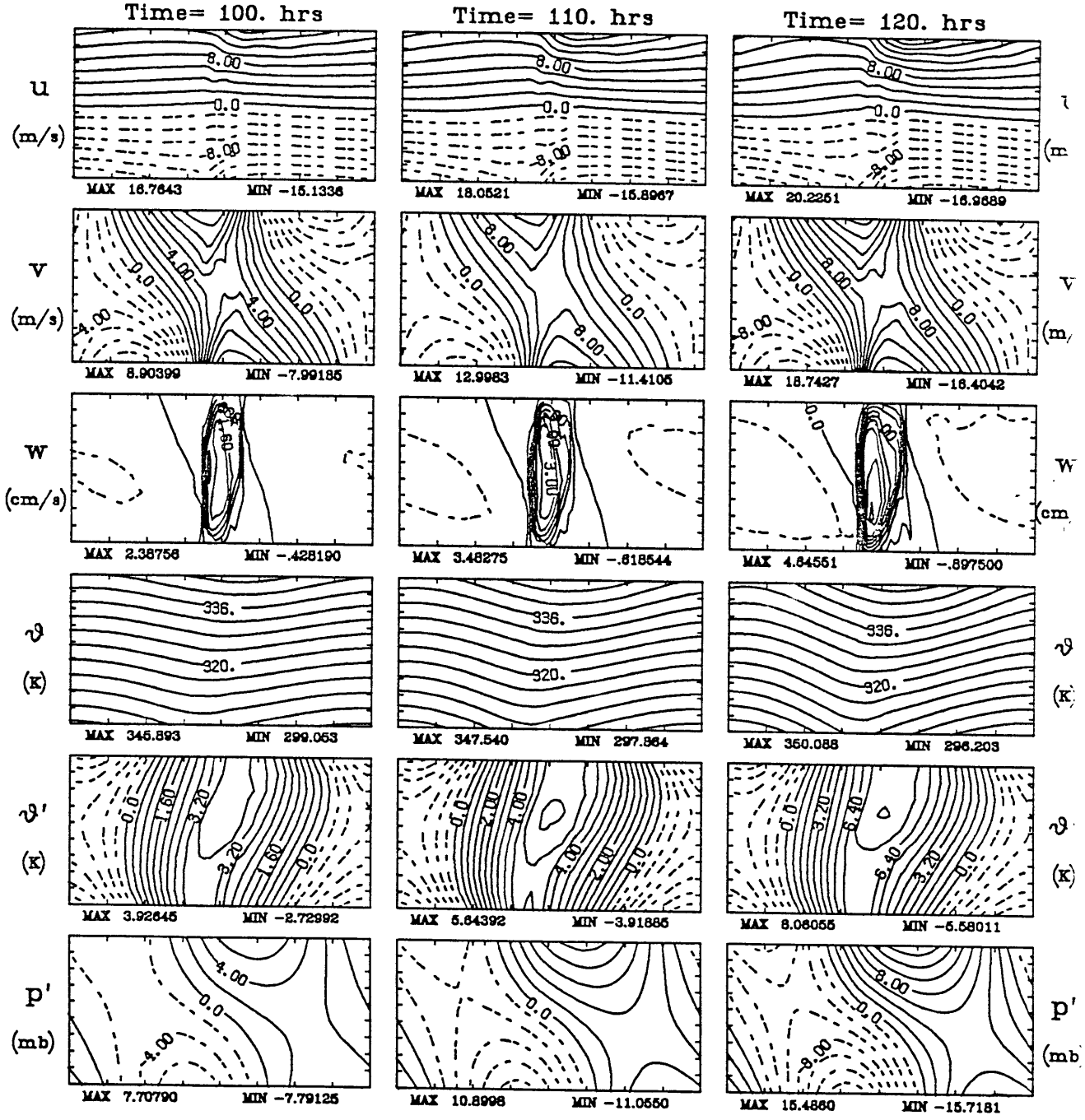


Fig.2.14 - same as 2.10 but for exp. A1 from 100 to 150 hrs

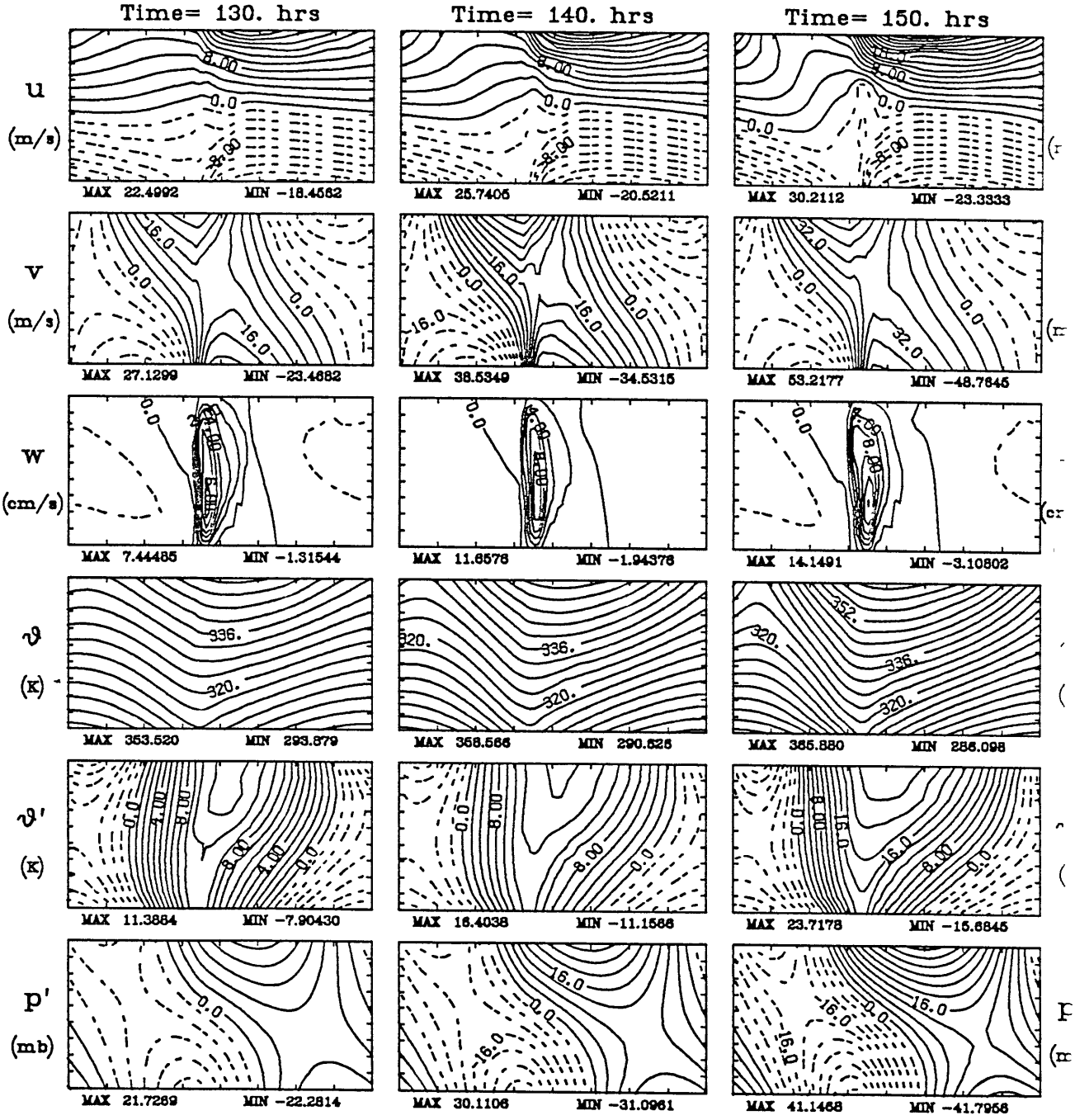

Time= 130. hrs
Time= 140. hrs
Time= 150. hrs
u
(m/s)
MAX 22.4992 MIN -18.4562
MAX 25.7405 MIN -20.5211
MAX 30.2112 MIN -23.3333
v
(m/s)
MAX 27.1299 MIN -23.4682
MAX 38.5349 MIN -34.5315
MAX 53.2177 MIN -48.7845
w
(cm/s)
MAX 7.44485 MIN -1.31544
MAX 11.6578 MIN -1.94378
MAX 14.1491 MIN -3.10802
ϑ
(K)
MAX 353.520 MIN 293.879
MAX 358.566 MIN 290.626
MAX 365.880 MIN 286.098
ϑ'
(K)
MAX 11.3884 MIN -7.90430
MAX 16.4038 MIN -11.1566
MAX 23.7178 MIN -15.6845
p'
(mb)
MAX 21.7289 MIN -22.2814
MAX 30.1106 MIN -31.0961
MAX 41.1468 MIN -41.7956

Fig. 2.14 (cont.)

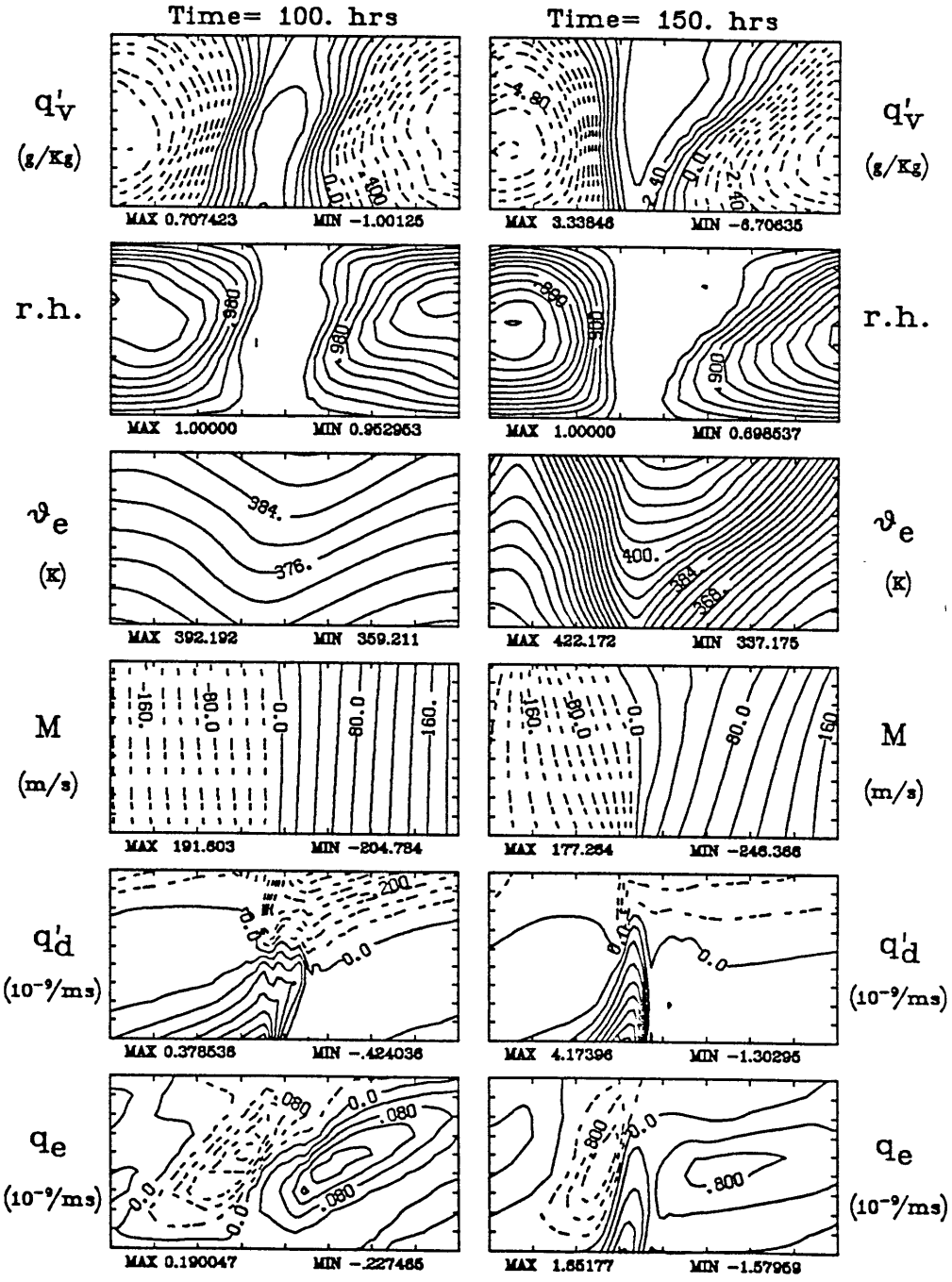


Fig.2.15 - q'_v, r.h., ϑ_e, M, q'_d, q_e for exp. A1 at 100 and 150 hrs

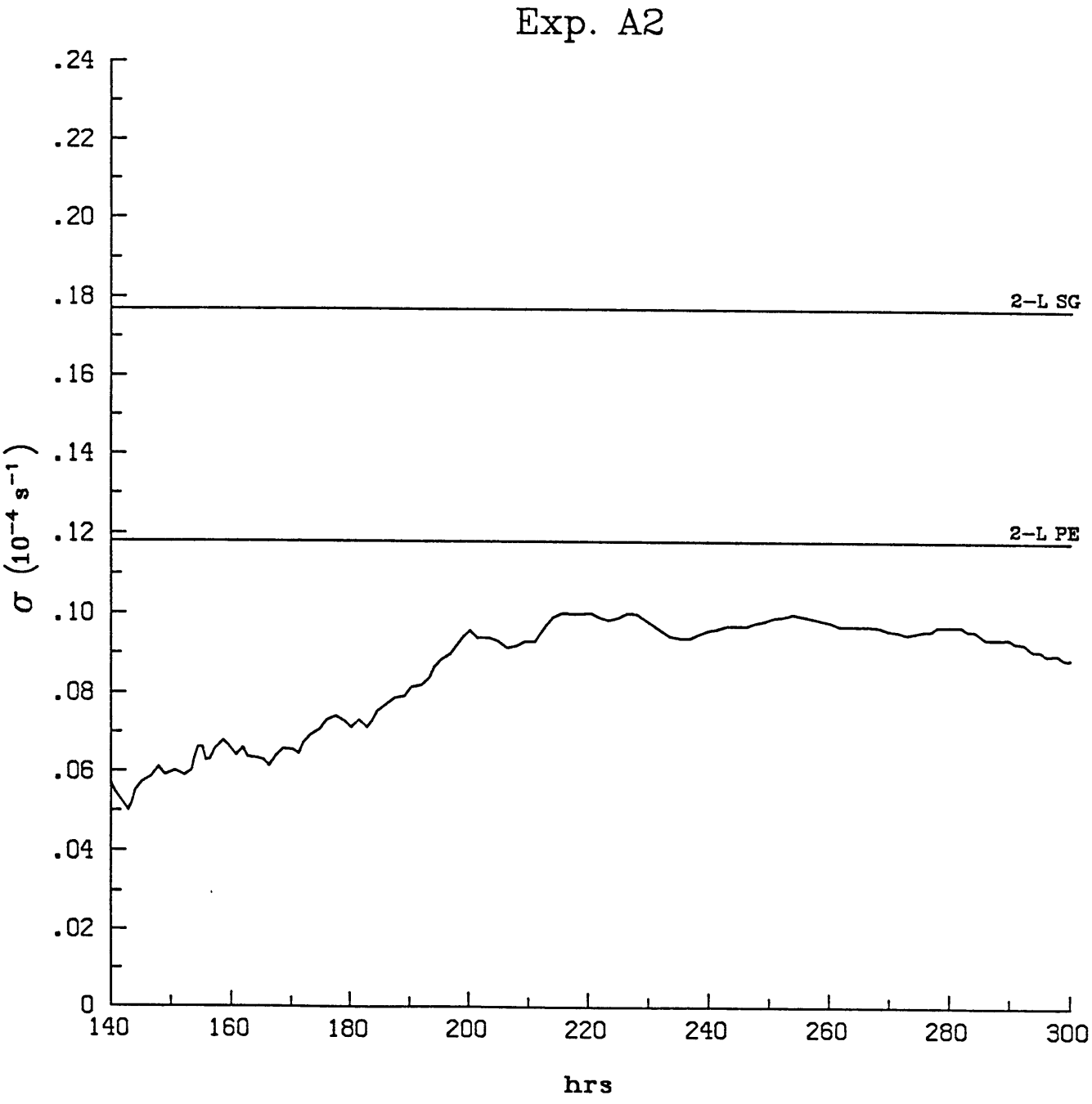


Fig.2.16 - same as 2.11 but for exp. A2

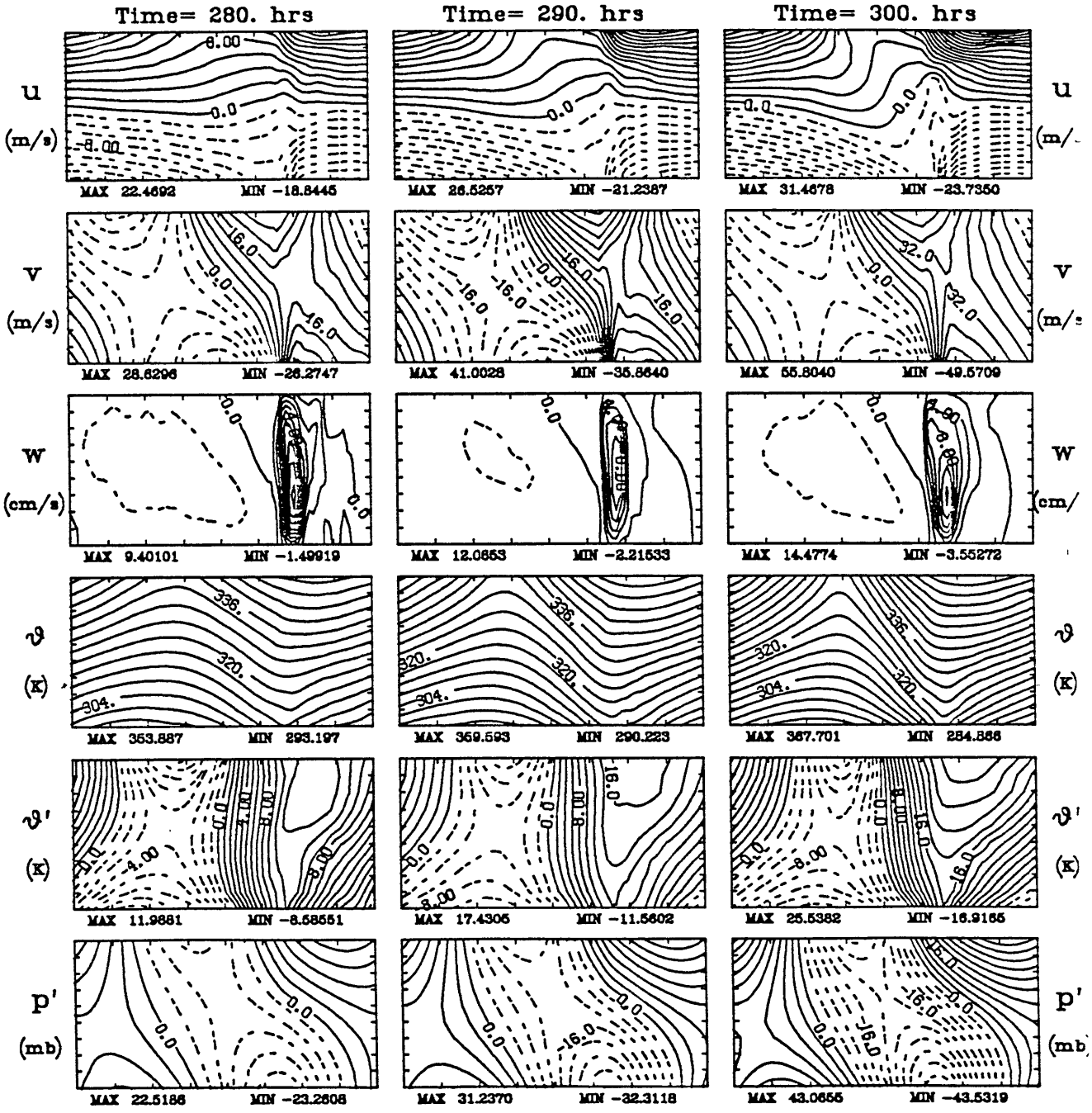


Fig.2.17 - same as 2.10 but for exp. A2 from 280 to 300 hrs

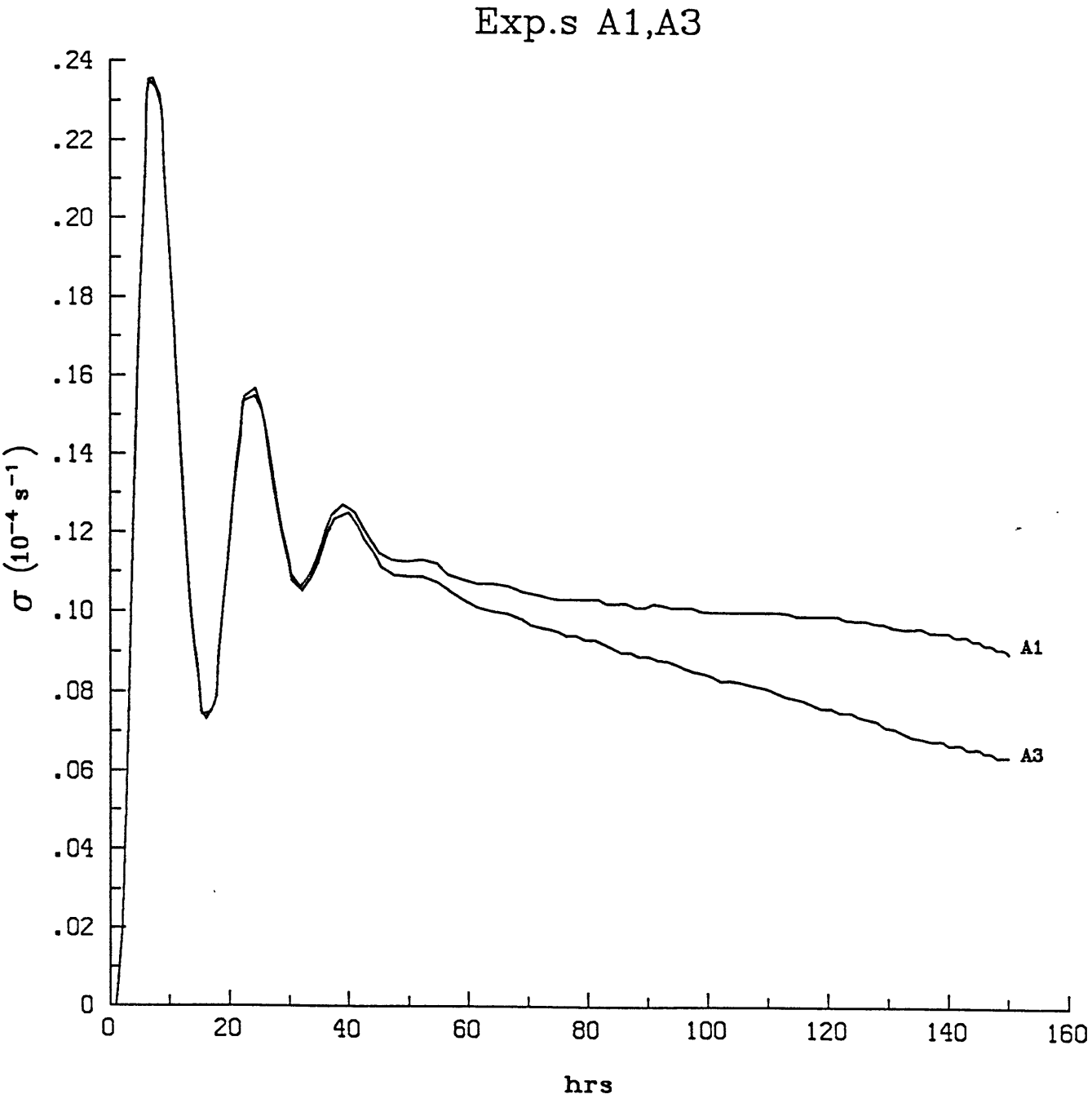


Fig.2.18 - Growth rate σ vs. time for exp.s A1 and A3

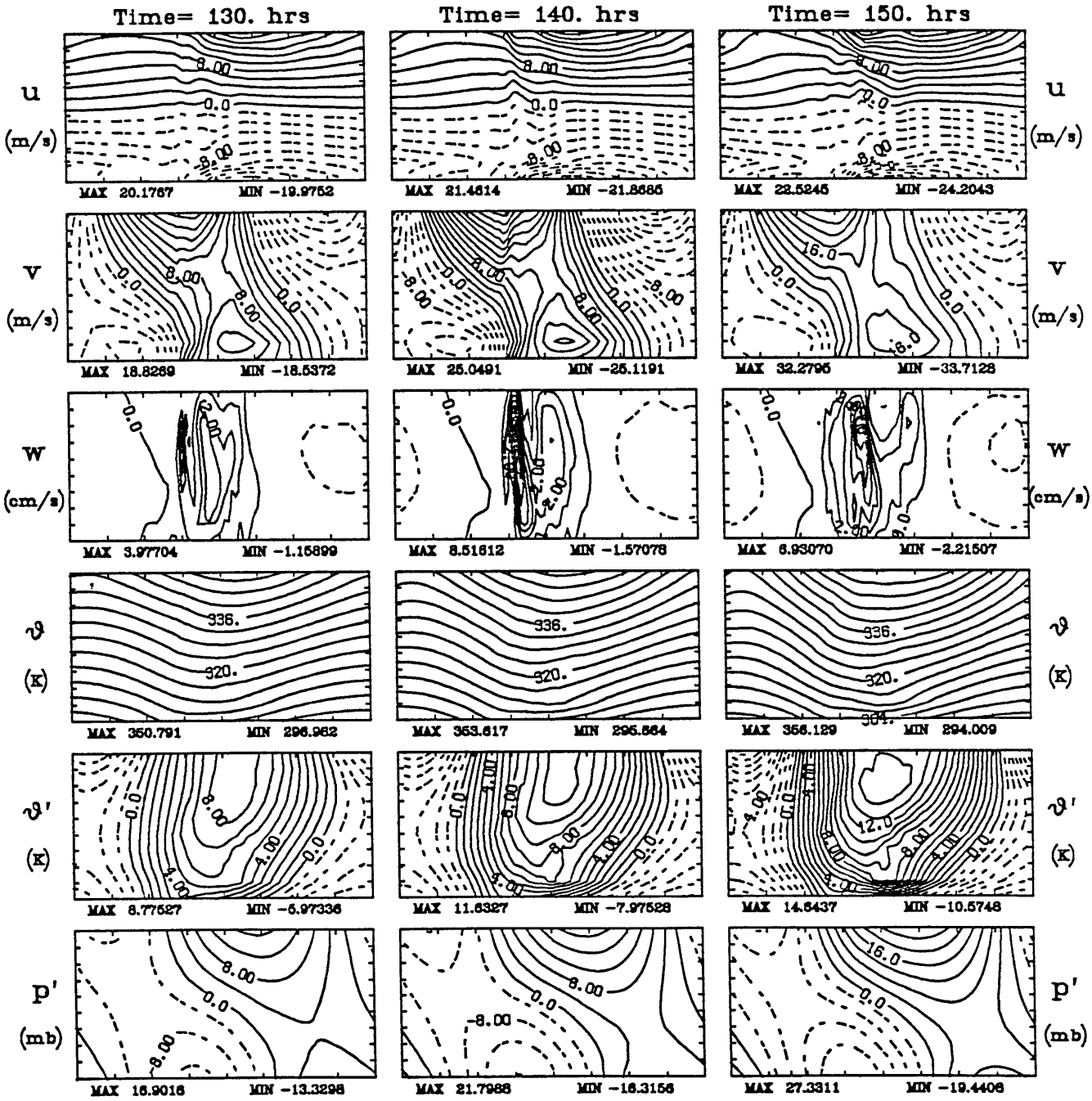


Fig.2.19 - same as 2.10 but for exp. A3 from 130 to 150 hrs

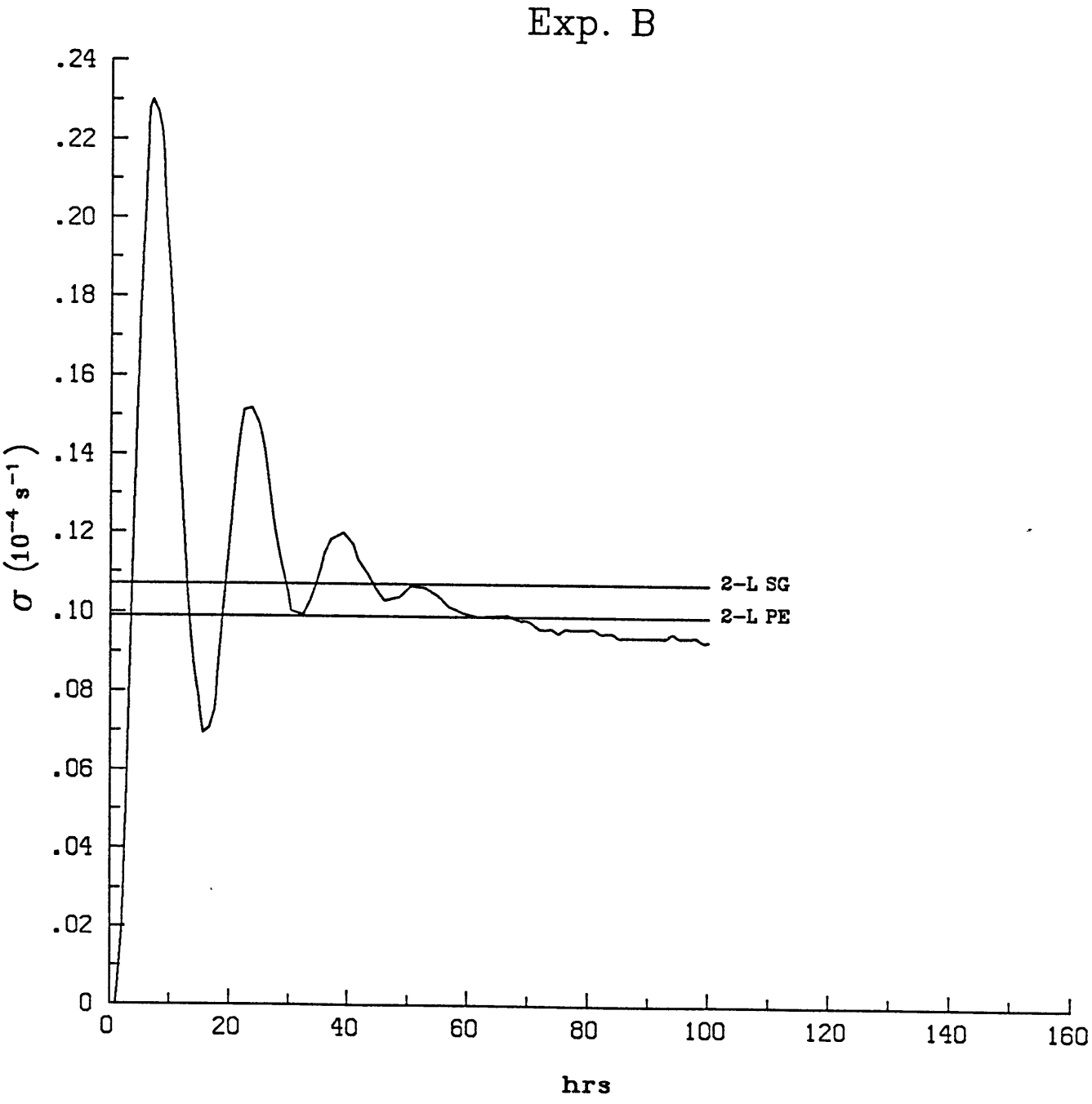


Fig.2.20 - same as 2.11 but for exp. B

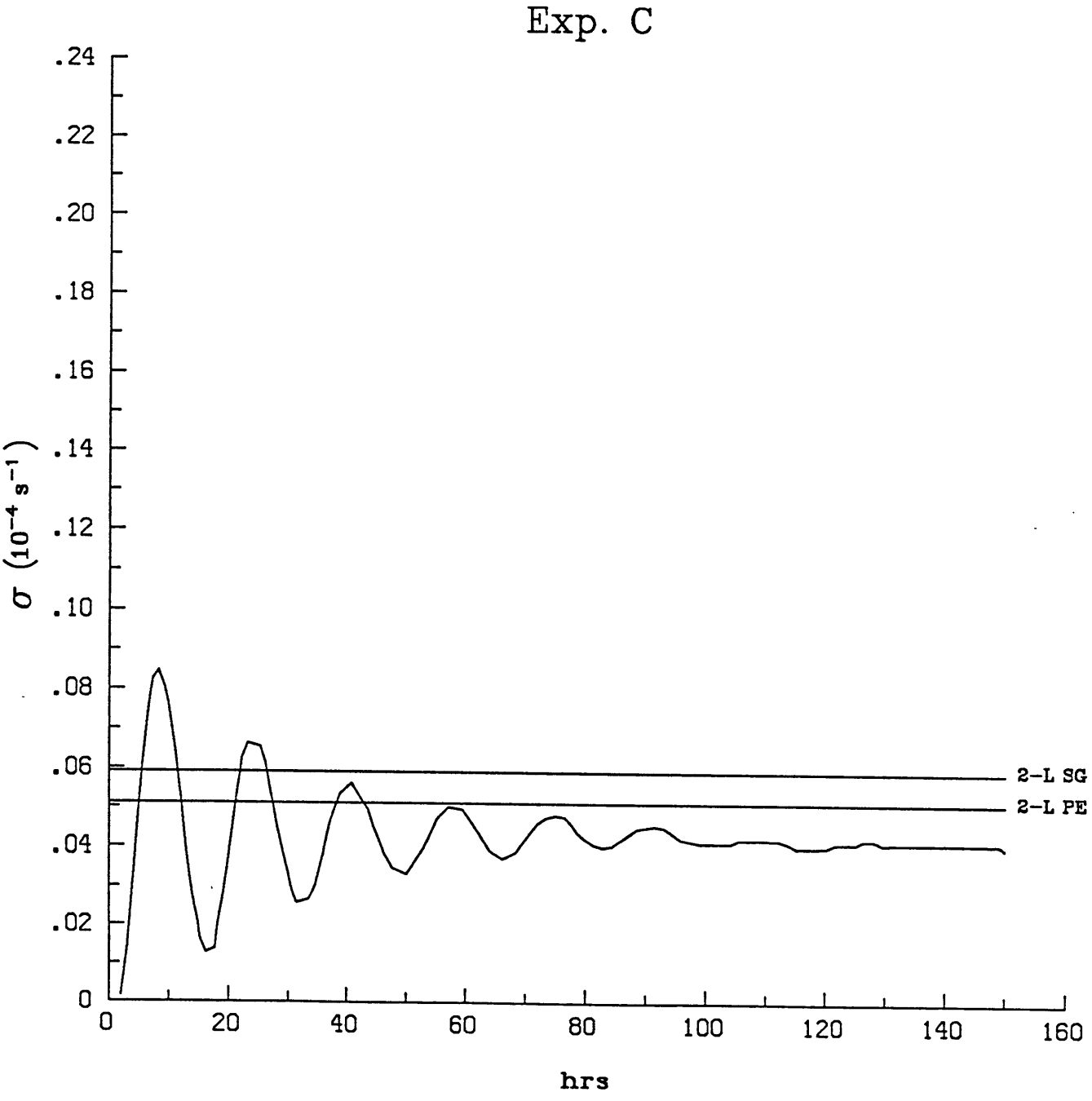


Fig 2.21 - same as 2.11 but for exp. C

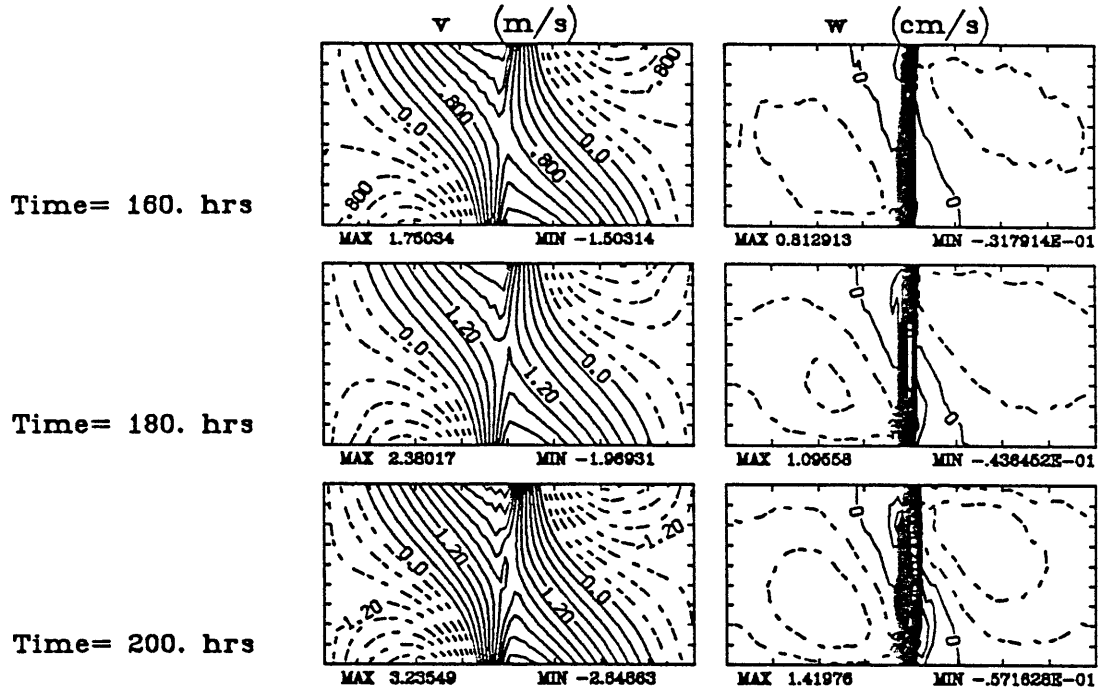


Fig.2.22 - same as 2.12 but for exp. C at 160,180,200 hrs

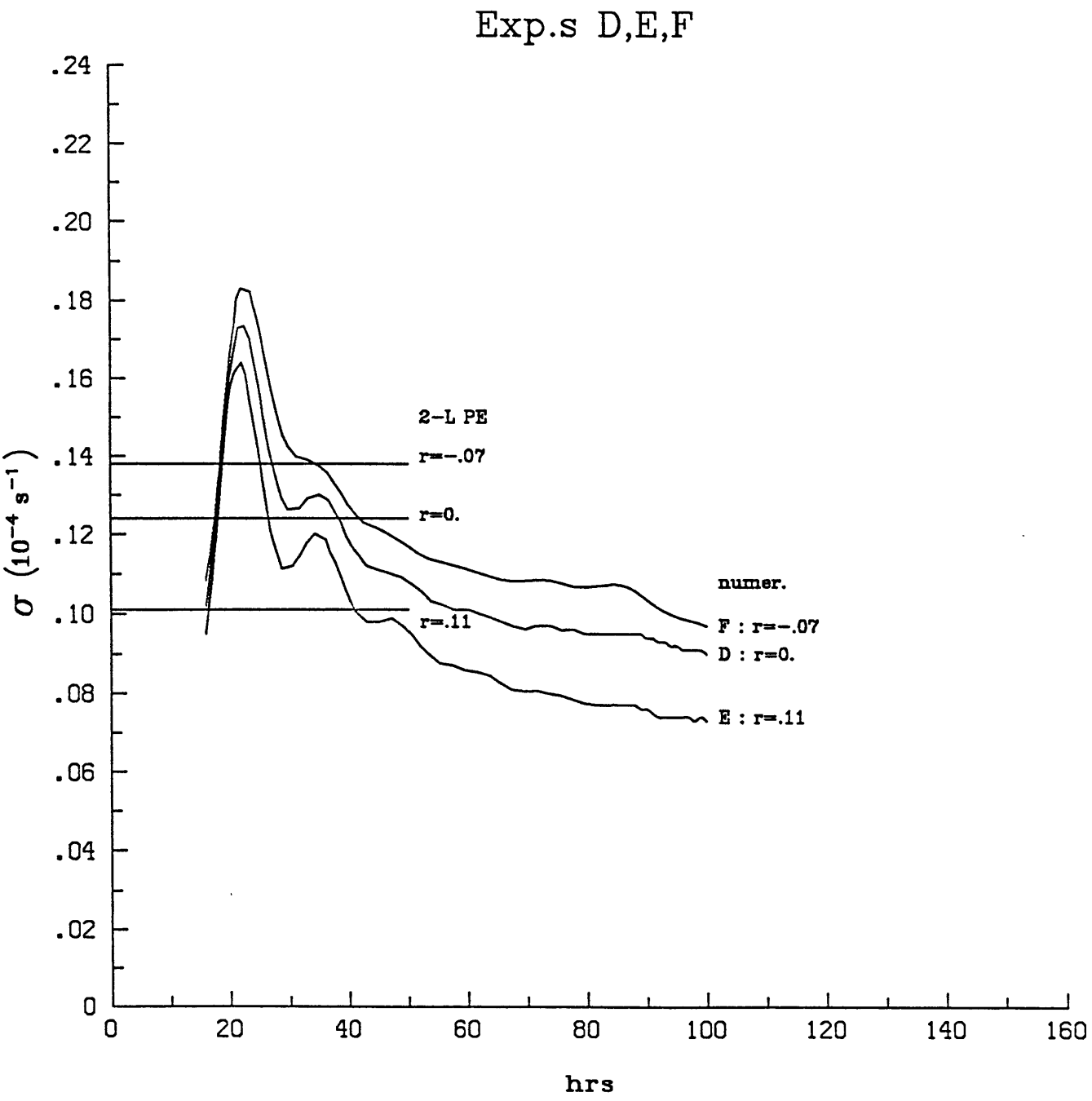


Fig.2.23 - Growth rate σ vs. time for exp.s D,E,F and for the two-level PE analytic model with the same parameters

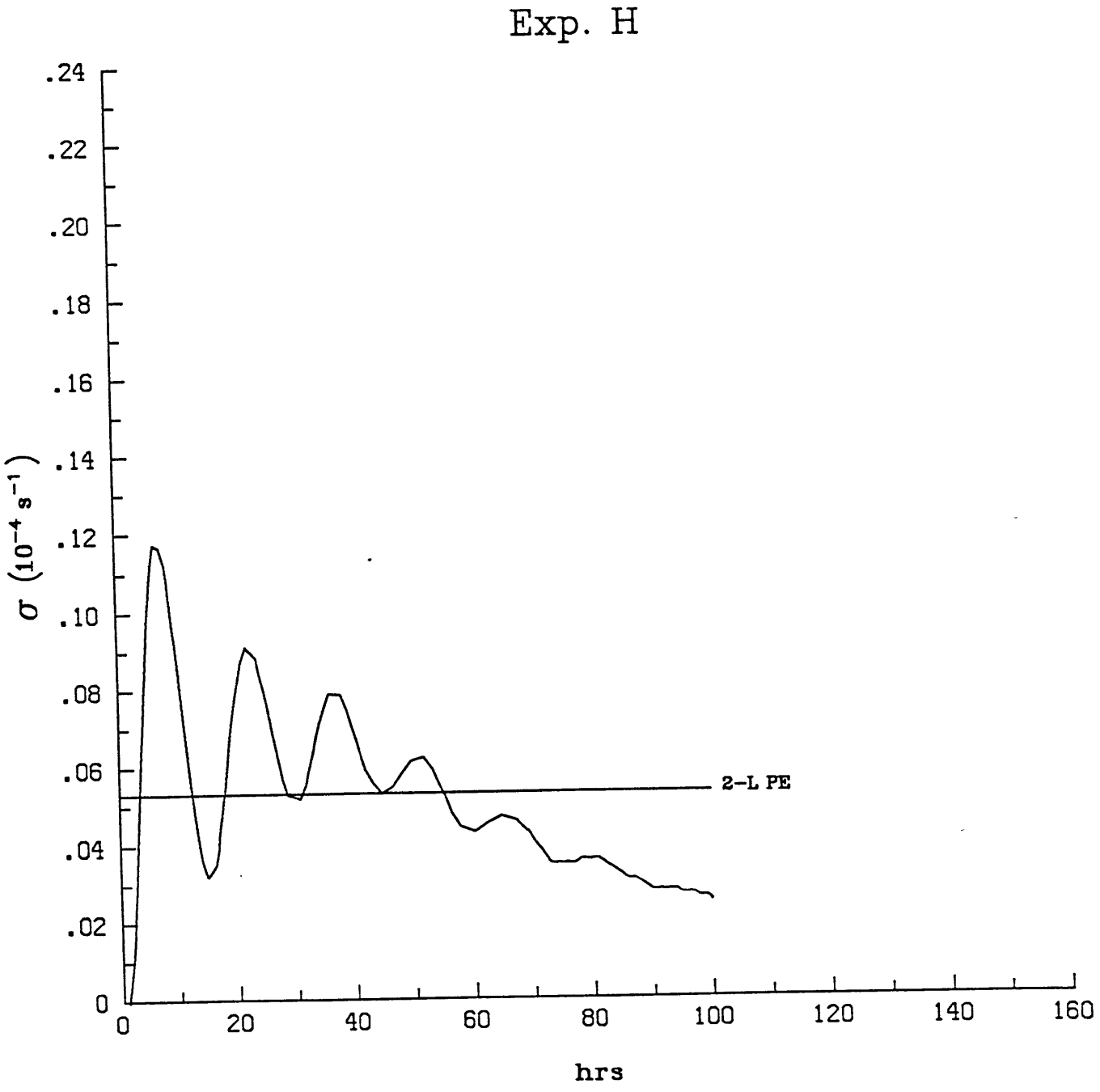


Fig.2.24 - same as 2.11 but for exp. H

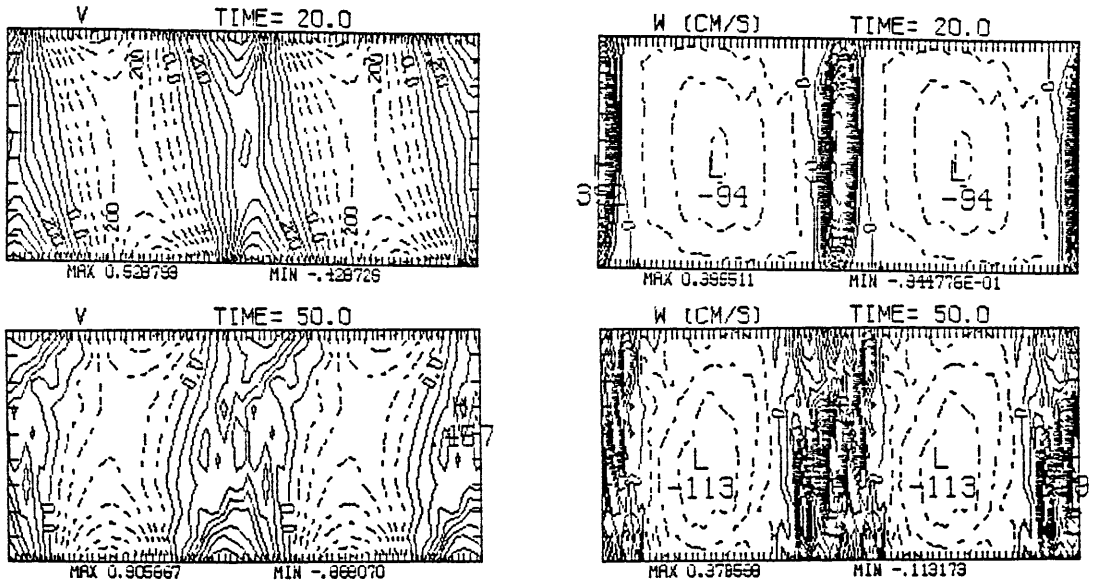


Fig.2.25 - same as 2.12 but for exp. G at 20 and 50 hrs

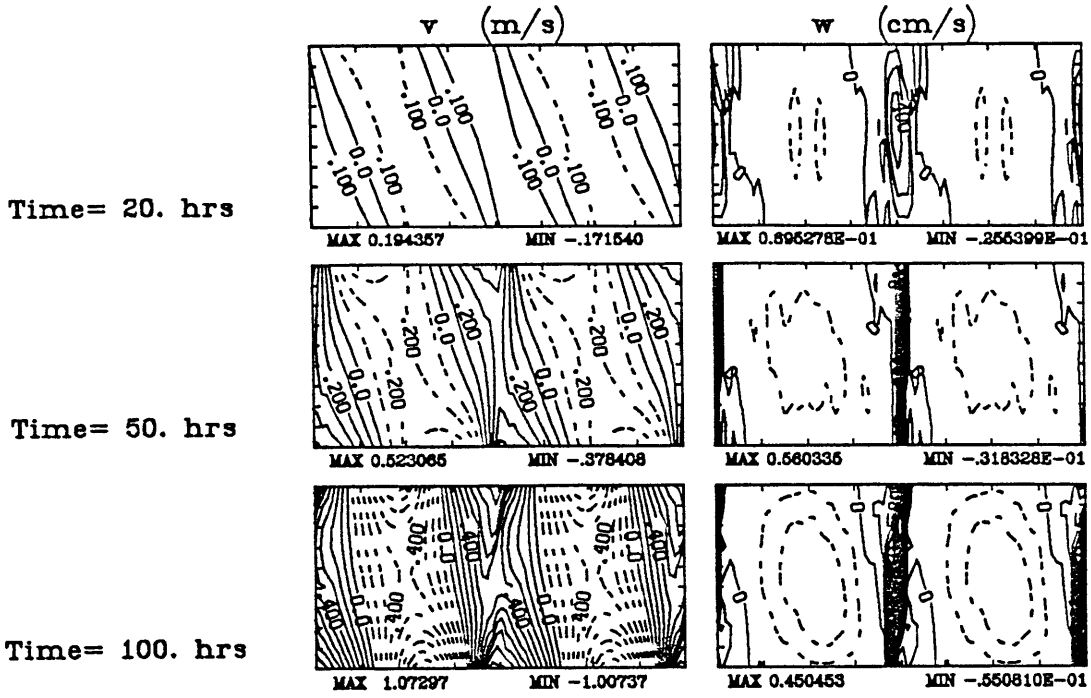


Fig.2.26 - same as 2.12 but for exp. H at 20,50 and 100 hrs

Appendix 2.A - Matching conditions for the linearized system

We present here for future reference the argument for the linearized system that will be used in the next sections. When we do not have a requirement on the transformation we have to get the continuity of v_1 and v_2 from some other source. On the other hand the interfaces are vertical in physical space, so the 'kinematic' condition on the normal velocity is just $u_0\Big|_{-\varepsilon}^{+\varepsilon} = -\psi_2\Big|_{-\varepsilon}^{+\varepsilon} = 0$ or $\psi\Big|_{-\varepsilon}^{+\varepsilon} = 0$ in the 2-level.

The 'dynamic' condition is the requirement of continuity of pressure. In order to derive this condition in a generalized fashion we rewrite system (2.16) in a frame of reference that moves at a speed u_0 in the positive x-direction

$$\begin{cases} (\sigma + (1-u_0)\partial_x) v_1 + \psi = 0 \\ (\sigma - (1-u_0)\partial_x) v_2 - \psi = 0 \\ (\sigma - u_0\partial_x)\theta - (v_1 - v_2) + q\psi_x = 0 \end{cases}$$

Now we integrate the momentum equations across the interface

$$\left[\sigma p_1 + (1-u_0) v_1\right]_{-\varepsilon}^{+\varepsilon} + \int_{-\varepsilon}^{+\varepsilon} \psi = 0$$

$$\left[\sigma p_2 - (1+u_0) v_2\right]_{-\varepsilon}^{+\varepsilon} - \int_{-\varepsilon}^{+\varepsilon} \psi = 0$$

then the requirements $p_1\Big|_{-\varepsilon}^{+\varepsilon} = p_2\Big|_{-\varepsilon}^{+\varepsilon} = 0$ can be expressed, by sum and subtraction as

$$\left[(v_1 - v_2) - u_0(v_1 + v_2)\right]_{-\varepsilon}^{+\varepsilon} = 0 \quad ; \quad \left[(v_1 + v_2) - u_0(v_1 - v_2)\right]_{-\varepsilon}^{+\varepsilon} + 2\int_{-\varepsilon}^{+\varepsilon} \psi = 0$$

Since the continuity of pressure cannot depend on the frame of reference we have to require $[v_1 - v_2]_{-\varepsilon}^{+\varepsilon} = 0$ and $[v_1 + v_2]_{-\varepsilon}^{+\varepsilon} = 0$ separately in order to satisfy the first of the above conditions for any u_0. The second then becomes just $\int_{-\varepsilon}^{+\varepsilon} \psi = 0$. We can express this by integrating (2.1ψ), or, more simply, get an equivalent condition from the thermodynamic equation above:

$$[\sigma(p_1 - p_2) - u_0(v_1 - v_2) - (v_1 + v_2) + q\psi_x]_{-\varepsilon}^{+\varepsilon} = 0$$

which gives $q\psi_x|_{-\varepsilon}^{+\varepsilon} = 0$. We therefore apply four conditions on ψ, v_1, v_2 and either $q\psi_x|_{-\varepsilon}^{+\varepsilon}$ or $\int_{-\varepsilon}^{+\varepsilon} \psi \, dx$.

Appendix 2.B - Proof that σ^2 is real for the SG two-level model

Multiply (2.17) by ψ^* (the complex conjugate of ψ) and integrate over a wavelength (end points are immaterial and will not be noted)

$$2\sigma^2\int|\psi|^2dx - \sigma^2\int\psi^*(q\psi_x)_x dx + \int\psi^*\left(2\psi_x+(q\psi_x)_{xx}\right)_x dx = 0$$

For the 2nd and 3rd term we know that neither factor in the integrand has a δ-like behavior at the interface because of the matching conditions imposed (see footnote pag. 35). Integrate by parts and use the periodicity of the solution to get

$$\int\left(q|\psi_{xx}|^2-2|\psi_x|^2\right)dx+\sigma^2\int\left(q|\psi_x|^2+2|\psi|^2\right)dx = -\int\psi_x\psi^*_{xxx}q_x\,dx$$

Since $q_x=(1-r)(\delta(x-C)-\delta(x-A))$ the r.h.s is

$$-(1-r)\left(\psi_{xx}(C)\psi^*_{xx}(C)-\psi_x(A)\psi^*_{xx}(A)\right)$$

but because $\psi_x(A)=\psi_x(C)=0$ this is zero and therefore σ^2 is real.

Appendix 2.C - QG and GM non-dimensional quantities

Let

$$L_{QG}^2 = \frac{N^2 H^2}{f_0^2} \quad , Ri_{QG} = \frac{N^2}{\bar{u}_z^2}$$

then the non-dimensional form of (2.29) is

$$\frac{1}{Ri_{QG}} D^3 \psi + D \psi_{zz} + D \psi_{xx} - 2 \psi_{xz} = 0 \quad ; \quad D \equiv \partial_t + \bar{u} \partial_x$$

the limit for $Ri_{QG} \to \infty$ of this is QG, as is well known. However, write $N^2 = (N^2 - \bar{u}_z^2) + \bar{u}_z^2$ and rescale with

$$L_{GM}^2 = \frac{(N^2 - \bar{u}_z^2) H^2}{f_0^2} = L_{QG}^2 - \frac{\bar{u}^2}{f_0^2} \quad ; Ri_{GM} = \frac{N^2 - \bar{u}_z^2}{\bar{u}_z^2} = Ri_{QG} - 1$$

then the non-dimensional form of (2.29) is

$$\frac{1}{Ri_{GM}} D^3 \psi + D \psi_{zz} + D \psi_{xx} + \frac{1}{Ri_{GM}} D \psi_{xx} - 2 \psi_{xz} = 0$$

the limit of this for $Ri_{GM} \to \infty$ is now the GM approximation. In other words we recover QG by neglecting $\bar{u}_z^2$ compared to N^2 ; and we recover GM by neglecting $\bar{u}_z^2$ compared to $N^2 - \bar{u}_z^2$. Since $N^2 \sim N^2 - \bar{u}_z^2$ for either $Ri_{QG} \to \infty$ or $Ri_{GM} \to \infty$, either form is correct in this limit. In the opposite limit the shift in the definition of the Richardson number moves the singularity from $N^2 = 0$ $(Ri_{QG} = 0)$ to $\bar{q} = 0$ $(Ri_{GM} = 0$ or $Ri_{QG} = 1)$.

Appendix 2.D - σ^2 for the PE two-level model

With the same procedure described in App. 2.B we find

$$\int((q+Ro^2)|\psi_{nn}|^2-2|\psi_n|^2)+\sigma^2\int((\tfrac{3}{2}Ro^2+q)|\psi_n|^2+2|\psi|^2)+$$

$$+\sigma^4\int\frac{Ro^2}{2}|\psi|^2=0$$

Let

$$A\equiv\int((q+Ro^2)|\psi_{nn}|^2-2|\psi_n|^2)$$

Since the other two coefficients are positive we can discuss the behavior of σ^2 in terms of A (but since A depends on the eigensolution itself we cannot say a priori whether any of the classes of solutions that follow are not empty).

For $A<0$, which is always the case when $N^2<0$, and may occur, depending on the form of the eigensolution, for some $N^2>0$, the two values of σ^2 are real, one being positive and one negative. When $Ro=0$ the negative root disappears, so in fact the modes of positive σ^2 with $A<0$ are the continuation of the GM solutions. At A = 0 the positive root has become $\sigma^2=0$. At $A>0$ we cannot say a priori what the sign of the discriminant is. Assume there is a $A_0>0$ for which $\Delta=0$; then for $0<A<A_0$ we get two real negative σ^2, i.e. four neutral, traveling solutions; for all $A>A_0$ there would be complex σ^2 and so unstable traveling modes. However, since this condition means N^2 large and positive, it is doubtful that this class of solutions exists

- more likely the eigensolutions in this range of N^2 are such that A is never larger than A_0.

3.1

In this chapter we examine the effect of adding a heat flux from the lower boundary in the models of ch.2. This is intended to simulate the behavior of developing baroclinic waves over the ocean, in an environment favourable for the explosive growth observed and described in the studies mentioned in the Introduction. We will use for this purpose the numerical model of sect.2.3, but first, in this section, we extend the SG model of sect 2.1.. It turns out that the eigenvalue problem as it is formulated here does not have a unique solution, but rather that we can only determine a possible range of growth rate, width of the updraft, and phase speed. Although it can be argued that the most unstable of these will be favoured we suspect that a model with internal diffusion would resolve the ambiguity by securing the continuity of all physical variables across the interfaces, and the mode thus selected would not necessarily be the most unstable of those found here. We think however that a better way to accomplish this is to simply use the numerical model of sect 2.3 - the investment of time and computation needed to include internal diffusion in the 2-L model would not be adequate to the sole result of small quantitative alterations of an already very idealized situation. As for the 2-L PE model, we already know from sect.2.2 what consequences the use of the primitive equations has on the moist baroclinic modes - it makes them sensitive to the Rossby number of the base state, reducing the growth rate, and allows us to find solutions in a slantwise unstable environment, as long as it is not vertically unstable. The simplifying

assumptions that we have to make in order to be able to solve a two level model with heat fluxes at the bottom boundary easily offset the better accuracy of the PE response in this situation. In summary, we still wish to present the 2-L SG for logical continuity with the previous chapter and then we will focus, in the next section, on the numerical simulations.

We now proceed to introduce a heat flux from the lower boundary as an explicit diabatic heating term in the thermodynamic equation of the 2-L SG model of sect.2.1. The 1st principle of thermodynamics can be written

$$\delta Q = c_p dT - \frac{1}{\rho} dp + L dq_v$$

Applying this law to adiabatic reversible processes the conservation of equivalent potential temperature θ_e is deduced. The transfer of heat from the sea surface to the air in contact with it has two components: $c_p \Delta T$ and $L \Delta q_v$, that are referred to as sensible and latent heat, respectively. The fluxes are usually parameterized (see Jacobs,1942; Malkus,1962) with a drag law of the form

$$Flux = C |\vec{u}|_{air} (a_{sea} - a_{air})$$

where a is $c_p T$ or $L q_v$; the subscript 'sea' refers to saturated air at the temperature of the sea surface, and 'air' to the air at some height (a few meters) above the surface. If the empirical drag coefficients C are the same for the two quantities the two laws can be combined in an expression for $c_p T + L q_v$, or, equivalently, $c_p \theta_e$. Following

Ooyama,1969 we write the sensible plus latent heat flux from tha sea surface as

$$F_o = C_D |\vec{u}|_{air} C_p (\theta_{e_{sea}} - \theta_{e_{air}})$$

The heat exchanged with the ocean will remain in the boundary layer unless some mechanism more efficient than turbulent diffusion can transport it upward - this role is played by convective activity in the moist region and we here assume that there is no such mechanism in the dry region (*). Since we know the potential temperature only at one point located in the middle troposphere we assume that only in the moist region is the thermodynamic equation affected by diabatic heating. We further assume, consistently with the 2-level discretisation, that the heat received from the sea is uniformly distributed in the troposphere, i.e. that the flux decreases linearly from the value F_o at z=0 to zero at z=H , so that the thermodynamic equation is written

$$\frac{d\theta_e}{dt} = \frac{C_D}{H} |\vec{u}|_a C_p (\theta_{e_s} - \theta_{e_a}) \qquad (3.1)$$

To deal with this term it is necessary to consider small amplitude perturbations and linearized equations; we now assume a basic state

---

(*) In the real world, and in the numerical model of the next section, it is of course possible to have convection, dry or moist, anywhere if the latent and sensible heat input at the bottom boundary is large enough to create instability.

with zero velocity at the surface and a constant air-sea equivalent temperature difference $\overline{\Delta\vartheta_e}$. The perturbation form of $\dot{Q}$ is then $\frac{c_D}{H}|\vec{u}|_{z=0} c_p \overline{\Delta\vartheta_e}$. For convenience we will later write the equations in a moving coordinate frame, but it is understood that in the system in which the sea is at rest the basic state surface velocity is zero so that the thermal forcing does not enter the equation for the basic state.

A different linearisation of (3.1) is possible: if $\overline{\Delta\vartheta} = 0$ then the base state is balanced for any $\bar{u}|_{z=0} \neq 0$. In this case it is possible to consider a heat flux given by the coupling of the perturbation temperature with the basic state surface wind $-(|\bar{u}|\vartheta')_{z=0}$: it is apparent that this heating always acts to reduce ϑ' and its gradient - it is negative where ϑ' is positive and viceversa. Then it reduces both the amplitude of the thermal wave and the temperature advection. It is therefore unlikely that this term could be responsible for increased instability.(*) On the other hand the heating term that we use reduces (see eq.(3.2) below) for positive v, to Γv, so that the meridional advection term in the thermodynamic equation $v\bar{\vartheta}_y$ becomes $v(\bar{\vartheta}_y - \Gamma)$, which is equivalent to an increase of the basic state

---

(*) Note that this argument is valid for the 2-level only. In a model with a higher vertical resolution we cannot a priori exclude that the wave modifies its structure in such a way as to take adventage of this form of heating (e.g. by changing phase with height more rapidly than an ordinary baroclinic wave).

baroclinicity (**). The two terms $|\bar{u}|\theta'$ and $|\vec{u}'|\overline{\Delta\theta}$ are mutually exclusive if we want to use the same basic state as in the previous chapter. The use of both terms would imply that both $\bar{u}|_{z=0}$ and $\overline{\Delta\theta}|_{z=0}$ are non-zero - therefore a heat flux in the form $C_D|\bar{u}|\overline{\Delta\theta}$ would appear in the zero-order equation and modify the base state.

The term $|\vec{u}'|$ is not easily tractable unless it has just one component that does not change sign, in which case it becomes linear. The perturbation velocity at z=0 has two components $(u_a, v_g + v_a)$: v_a is zero, being proportional to w (see eq.2.2) but v_g and u_a are both present. Moreover their values at z=0 are not explicitly known in the model - they can either be assumed to be equal to the values at level 2, or extrapolated from the two known levels to the surface. Since we are at this point more interested in the qualitative changes induced in the solutions by this form of diabatic heating, than in accuracy of details, we will use only v_2 as the perturbation velocity at the surface. We found in sect.2.1 that $v_2 > 0$ everywhere in region 1 and we hope that this will not change, at least for small values of the heat flux. This of course simplifies things, in that we can use the same setup of the model as in 2.1 (as opposed to having to further subdivide

---

(**) This is only a qualitative argument, and not entirely correct: Γ acts only in the updraft, which is order .1; Γ itself is order 1. so that, in a domain average, $\bar{\theta}_y - \Gamma$ is only 10% larger than $\bar{\theta}_y$ (see fig 3.1). A posteriori we can say that the increase in growth rate observed cannot be solely attributed to increased meridional heat flux.

the updraft region according to the sign of $w\big|_{z=0}$)(*).

We finally write the thermodynamic equation in the moist region as

$$\frac{\Gamma_d}{\Gamma_m}\left(\theta'_t + \bar{u}\,\theta'_x + v_g\bar{\theta}_y\right) + w q_e \frac{\theta_{e0}}{f_0} = \frac{C_0}{H}\,\overline{\Delta\theta_e}\, w_2 \qquad (3.2)$$

From sect.2.1 we know that w_2 is not in phase with θ and at least for small heating this character should be preserved (the limit $\dot{Q} \to 0$ is not singular). We then have a thermal forcing out of phase with the homogeneous solution and we cannot expect the forced solution to have the same phase speed. For mathematical convenience we write the equations in a frame of reference that moves with a velocity $\bar{u} + u_0^*$ in the positive x-direction. We assume that such a system exists in which σ^2 is real and solve the eigenvalue problem for σ, λ (as in sect.2.1) and u_0.

With the same scaling as in sect.2.1 we get the non-dimensional equations as

---

(*) This is a model of a continuous fluid resolved only at two levels in the vertical, and not a model of two superposed homogeneous layers of fluid. Accordingly it would be consistent to use a linearly extrapolated v at the surface. We checked the results for some values of the parameters with this choice of $w\big|_{z=0}$ and no major change occurs. In some cases however the extrapolated $w\big|_{z=0}$ becomes negative inside region 1 when zero or low heating is applied, so that the solution obtained is inconsistent. In all cases an increased heat flux forces a positive v at the surface.

$$\begin{cases} (\sigma + (1-u_0)\partial_x)v_1 + \psi = 0 \\ (\sigma - (1+u_0)\partial_x)v_2 - \psi = 0 \\ (\sigma - u_0\partial_x)\vartheta - (v_1+v_2) + q\psi_x - \Gamma v_2 = 0 \\ \vartheta_x = v_1 - v_2 \end{cases} \tag{3.3}$$

Where $q=1, \Gamma=0$ in region 2 and $q=2, \Gamma=\Gamma_0$ in region 1;

$$\Gamma_0 = \frac{1}{2}\frac{g}{f_0\bar{u}} C_D \frac{\overline{\Delta v_e}}{\sigma_0}\frac{\Gamma_m}{\Gamma_d} \quad \text{(a constant)} \quad ; \; u_0 = u_0^*/\bar{u}$$

The equation for ψ derived from here is

$$(1-u_0^2)q\psi_{xxxx} + 2\sigma u_0 q\psi_{xxx} + (2(1+u_0^2) + \Gamma(1-u_0) - \sigma^2 q)\psi_{xx} + \\ + \sigma(\Gamma - 4u_0)\psi_x + 2\sigma^2\psi = 0 \tag{3.4}$$

and the meridional geostrophic velocities are given by

$$\begin{aligned} 4\sigma^2 v_1 &+ (1-u_0)^2(\sigma q\psi_{xx} - (1+u_0)q\psi_{xxx} - \Gamma\psi_x) - \\ &- 2(1-u_0)(1+u_0^2)\psi_x + 2\sigma(1+2u_0-u_0^2)\psi = 0 \\ 2\sigma^2(\Gamma+2)v_2 &- (1+u_0)^2(\sigma q\psi_{xx} + (1-u_0)q\psi_{xxx}) - \\ &- \Gamma(1-u_0^2)\psi_x - 2(1+u_0)(1+u_0^2)\psi_x - 2\sigma\Gamma\psi - \\ &- 2\sigma(1-2u_0-u_0^2)\psi = 0 \end{aligned} \tag{3.5}$$

The matching conditions are derived as in Appendix.2.A. We have to require continuity of $\psi, v_1, v_2, \vartheta$ and these imply the continuity of pressure. Expressed in terms of ψ and its derivatives, and of

v_{Bottom}, they are

$$
\begin{aligned}
&\text{i)} \quad \psi \\
&\text{ii)} \quad q\psi_n - \Gamma v_B \\
&\text{iii)} \quad (q\psi_n - \Gamma v_B)_x \\
&\text{iv)} \quad (1-u_0^2)(q\psi_n - \Gamma v_B)_{nx} + 2(1+u_0)\psi_x
\end{aligned}
\tag{3.6}
$$

(recall that we use $v_B = v_2$, but these expressions are valid for a general v_B). These expressions are valid unless $u_0 = \pm 1$. When this happens eq.3.3 becomes 3rd order and the momentum equations in 3.2 give $v_1 = -\psi/\sigma$ or $v_2 = \psi/\sigma$ so that only three matching conditions are required. We will use 3.6 above and check a posteriori that $u_0 \neq \pm 1$.

Condition ii) does not imply w=0 at A,B and C as it was in sect.2.1 but we still want w to change sign there. It is useful to impose conditions more restrictive than ii) that help to filter out some of the unwanted modes(*). Let

$$w^{(1)} = w_I \geq 0 \; ; \; w^{(2)} = w_{II} \leq 0 \; ; \; v_2^{(1)} = v_I \geq 0$$

at the interface. Then condition ii) gives

$$\tau w_I - \Gamma_0 v_I = w_{II} \leq 0$$

So we want $\Gamma_0 v_I \geq \tau w_I \geq 0$. We then introduce a factor δ such that $\tau w_I = \delta \Gamma_0 v_I \; ; \; w_{II} = (\delta - 1)\Gamma v_I \; ; \; 0 \leq \delta \leq 1$

(*) see sect.2.2 for analogous discussion in the no-flux case

When $\delta=0$ then $w_I=0$ and w_{II} has a negative non-zero value. When $\delta=1$ then $w_{II}=0$ and w_I has a positive non-zero value. The discontinuity of w at the interface is given by

$$\Delta w = w_I - w_{II} = \left(\frac{\delta}{r} - \delta + 1\right) \Gamma_0 \nu_I$$

We cannot say a priori what its value is, because ν_I is part of the eigensolution, but note that for $0<r\leq 1, 0\leq\delta\leq 1$, the term in parenthesis is always positive, so the vertical velocity will always have a discontinuity at the interface.

We replace condition ii) in 3.6 with the two separate conditions

$$\text{ii a)}\quad r\psi_x^{(1)} = \delta\,\Gamma_0\,\nu_2^{(1)}$$

$$\text{ii b)}\quad \psi_x^{(2)} = (\delta-1)\,\Gamma_0\,\nu_2^{(1)}$$

(where δ is allowed to have different values at the two interfaces and $0\leq\delta_A,\delta_C\leq 1$) and we then solve eq.(3.4) and apply the five conditions at the two interfaces. Since there are no obvious symmetry properties as in sect 2.1 we are left with the full 10x8 homogeneous linear system that will yield non-trivial solutions when three eighth-order determinants are set equal to zero. The 'dispersion relation' then will determine three eigenvalues - we solve for σ, λ, u_0 for given $L_2, r, \Gamma_0, \delta_A, \delta_C$. The last two parameters are perfectly arbitrary (as long as they are between 0 and 1). In the results presented next the most unstable solution is always the one with $\delta_A=\delta_C=0$ and the least unstable the one with $\delta_A=\delta_C=1$. Since the

width of the updraft changes by changing δ_A and δ_C we can think of these parameters as arbitrarily choosing the point at which the matching is performed within an interval of allowed widths determined by the other (physical) conditions (*).

Fig.3.1 shows the behavior of the eigenvalues when the heating Γ_0 is increased at fixed r and L_2. The spread due to the choice of δ_A, δ_C is shown. The more unstable (at fixed Γ_0) has a larger updraft (which is understandable, since heating acts only in the updraft, its effect is larger when it acts on a larger portion of the wave). The phase speed is also larger for the more unstable modes. The value of Γ_0 shown are realistic: for average atmospheric values $\Gamma_0 \simeq .1 * \overline{\Delta\sigma_e}$.

In Fig 3.2 the eigenvalues for the most unstable case ($\delta_A = \delta_C = 0$) versus L_2 are shown. Notice, above all, the further destabilisation of the short waves, and the large increase in growth rate. The phase speed is also increasing with Γ_0 but we will see in the next section that this is an artifact of the 2-level model (**).

The form of the eigensolution for $L_2 = 1.8$, $r = .1$, $\Gamma_0 = 2.$, $\delta_A = \delta_C = 0$ is displayed in fig.3.3. This mode has $\sigma = 1.5$, $\lambda = .17$, $u_0 = .23$. Major differences with the $\Gamma_0 = 0$ case are only the discontinuity of w and the presence of a double minimum of vertical velocity at the edges of the

---

(*) In a work by Lilly, 1960 a similar technique is applied to upright convection and the same problem arises. The growth rate is there found after arbitrarily picking the width of the updraft.

updraft, like a return flow that is not spread out uniformly in the downdraft region.

Finally fig. 3.4 is the growth rate as function of Γ_0 and τ for a fixed wavelength, showing a remarkably linear behavior with Γ_0 .

(**) As already noted the vertical structure is rigidly determined in a 2-level. The heating is proportional to σ_2 , so it is maximum slightly ahead of the thermal wave (see fig.3.3) and therefore it induces a forward motion. This does not change if σ_{BOT} is linearly extrapolated. It does not seem impossible that a heating proportional, say, to σ_1 , which is maximum sligthly behind the thermal wave would produce a backward motion, but of course there is no justification for doing this in the present model. This effect, that is in fact observed in the numerical model of the next section is accomplished by a different vertical structure of the wave.

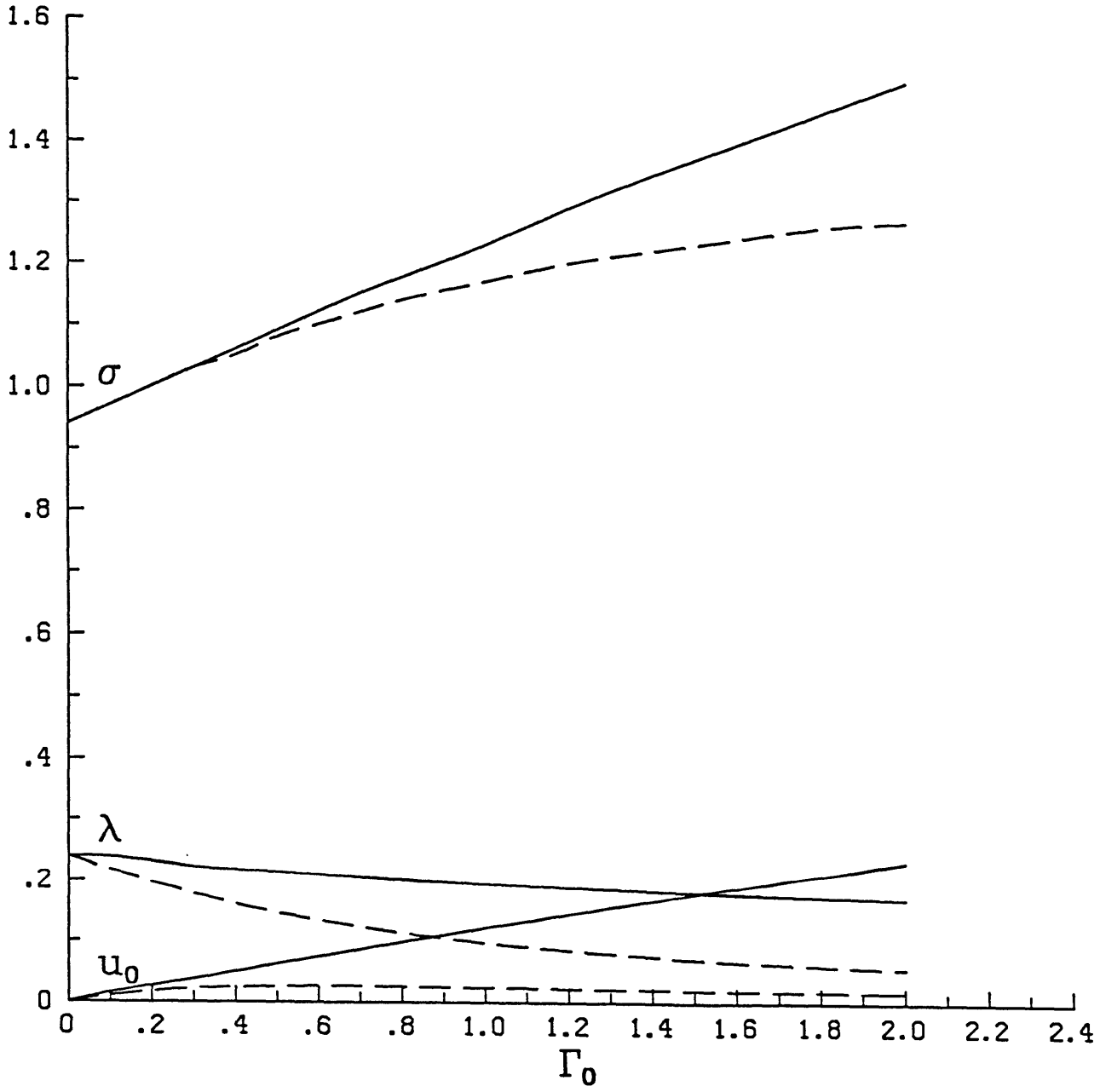


Fig.3.1 - Eigenvalues σ, λ, u_0 of the SG 2-level model with heat flux from the lower boundary vs. heating parameter Γ_0 for r=.1, L2=1.8. Solid:most unstable $\delta_A = \delta_C = 0$, dashed: least unstable $\delta_A = \delta_C = 1$.

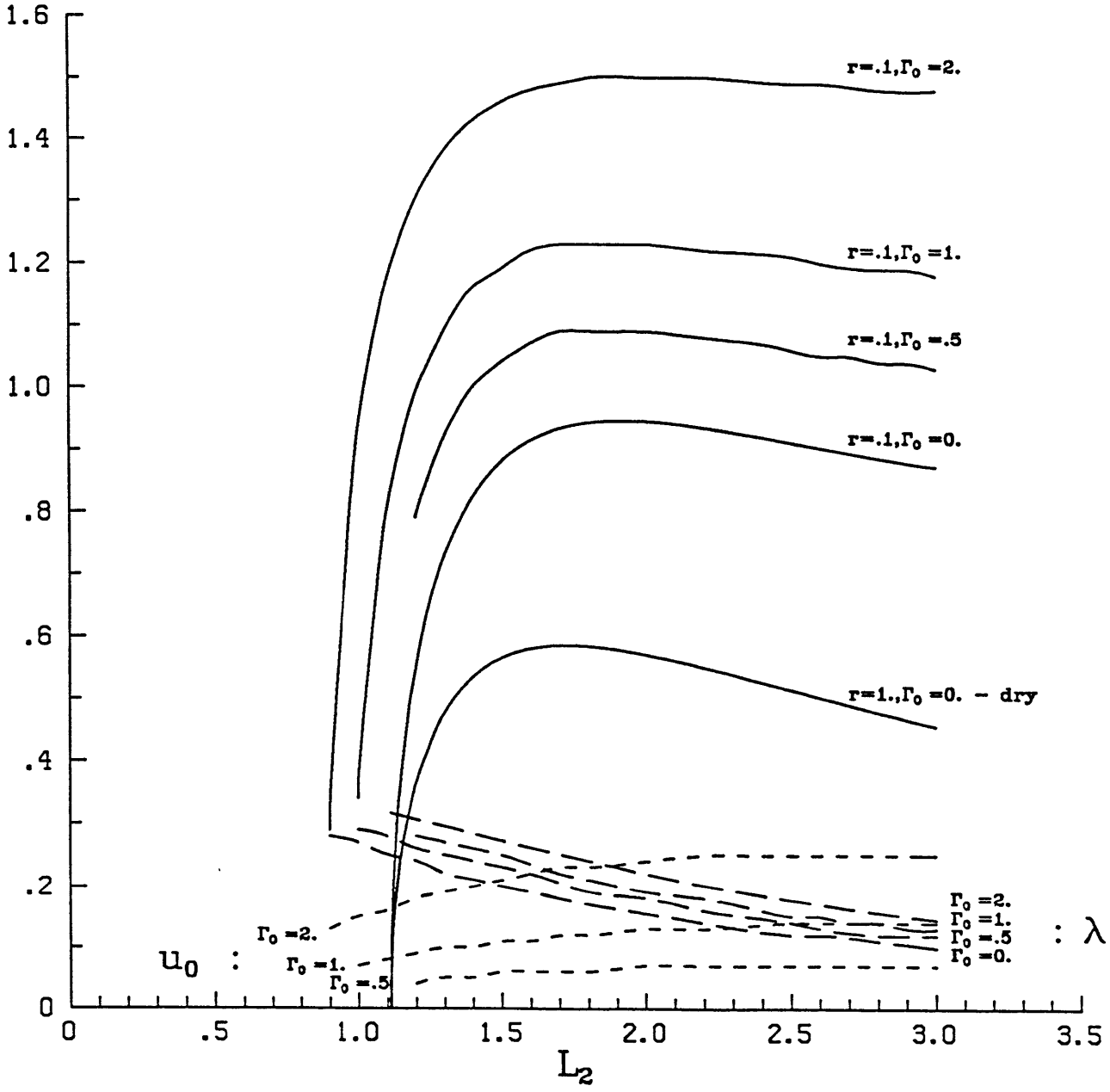


Fig.3.2 - Eigenvalues σ, λ, u_0 vs. L2 for various values of the heating parameter Γ_0 for the most unstable case $\delta_A = \delta_C = 0$ (see text). Solid: growth rate σ ; long dash: ratio of the width of the updraft to downdraft λ ; short dash: relative phase speed u_0 .

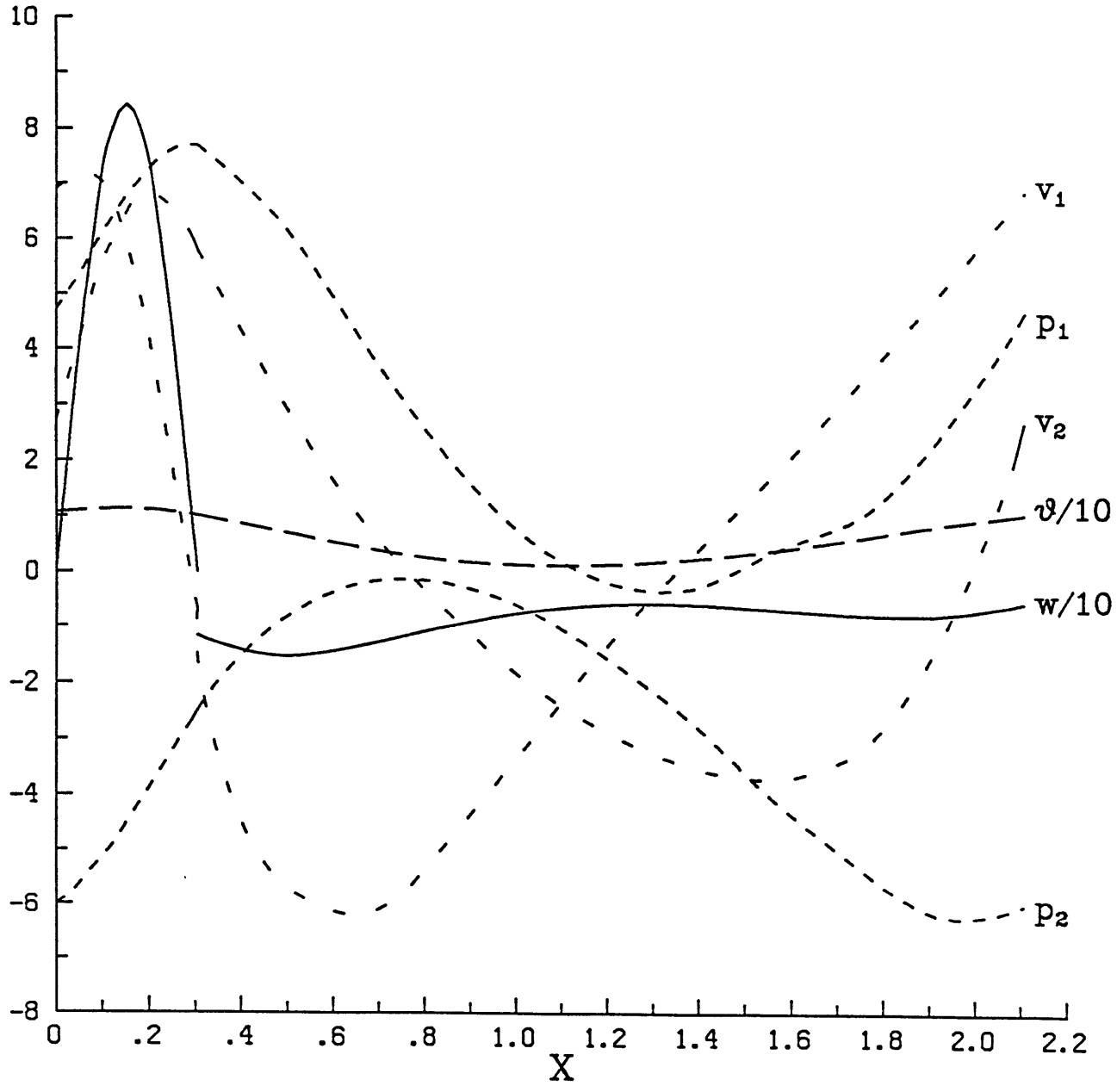


Fig.3.3 - Form of the eigensolution for L2=1.8, r=.1, Γ_0 =2., $\delta_A = \delta_C = 0$. Eigenvalues for this mode are σ =1.5, λ =.17, μ_0 =.23. Pressure is known only from it derivative v, so that an arbitrary constant can be added to both p1 and p2.

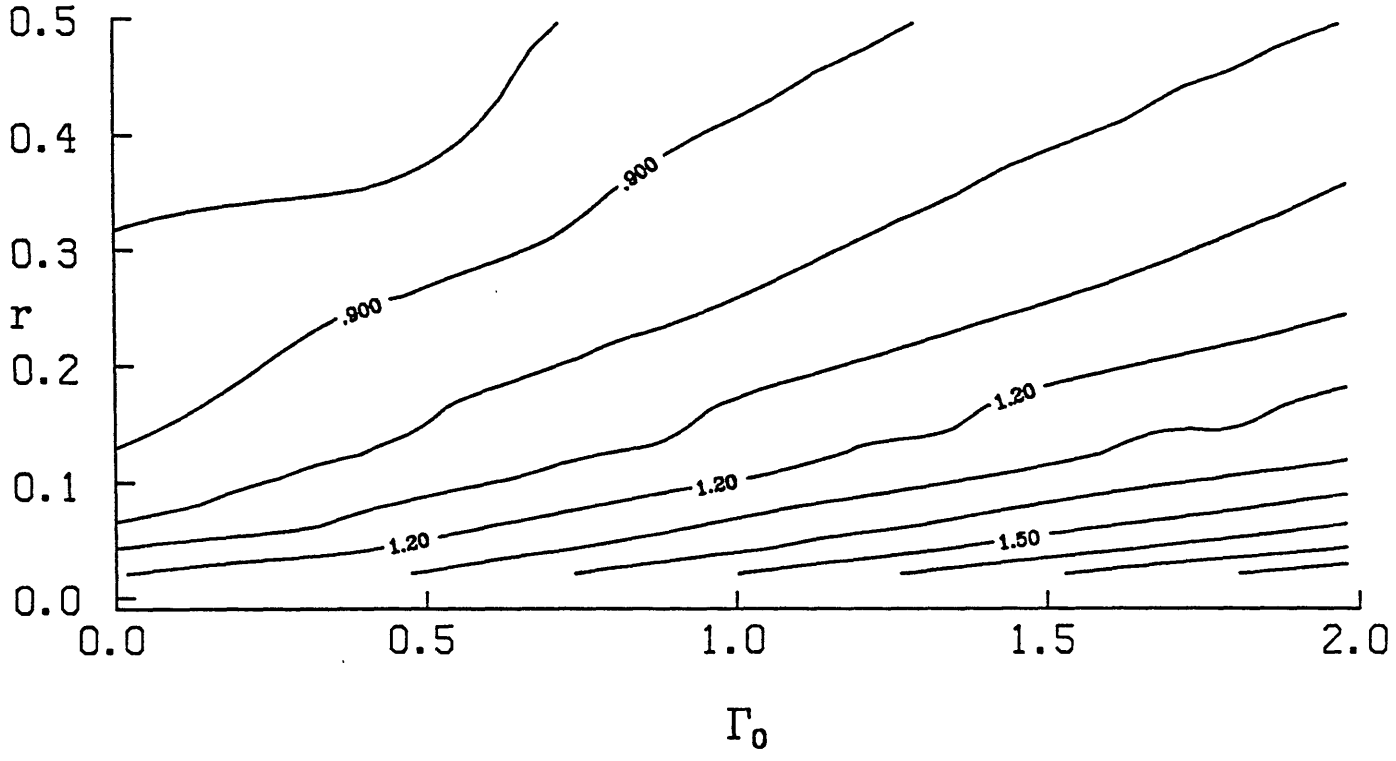


Fig.3.4 - Contours of constant growth rate σ for L2=1.8, $\delta_A = \delta_C = 0$, on the Γ_0, r plane.

3.2

The numerical model of sect.2.3 is used again in this section with added heat and moisture fluxes from the lower boundary in the form used in Rotunno and Emanuel,1987, i.e.:

$$F_{(\theta)} = C_E \left(\sqrt{u^2 + v^2}\right)_{j=1} (\theta_{surf} - \theta_{j=1})$$

$$F_{(q_v)} = C_E \left(\sqrt{u^2 + v^2}\right)_{j=1} (q_{v_{surf}} - q_{v_{j=1}})$$

where

$$\theta_{surf} = (\bar{\theta}_{j=1} + \overline{\Delta\theta}) \frac{\bar{\pi}_{j=1}}{\bar{\pi}_{j=1} + \pi'_{j=1}}$$

$$q_{v_{surf}} = (rh)\, q_v^{sat}(\theta_{surf}, \pi_{j=1})$$

The latter quantities are functions of x and t through the surface pressure perturbation π' . The relative humidity and the air-sea temperature difference in the base state $\overline{\Delta\theta}$ are chosen uniform in space. Both these parameters contribute to $\overline{\Delta\theta_e}$ - here the relative humidity is fixed at 100% and only $\overline{\Delta\theta}$ is varied. The limitations of the linearized saturation law that we use become evident at this point. In the model's thermodynamics $\overline{\Delta\theta_e} = 1.5\ \overline{\Delta\theta}$ always, and this is not a good approximation of the real thermodynamics. For example a $\overline{\Delta\theta} = 5K$ at the surface (θ_{air} =300 K ;p=1000. mb) gives $\overline{\Delta\theta_e}$ =25.2 K in the real world (using the value given in the Smithsonian meteorological tables for saturation mixing ratio) but only 7.5 K in the model. As long as the total $\overline{\Delta\theta_e}$ is relevant we can use arbitrarily high values of

$\Delta\theta$(model) to reach a $\Delta\theta_e$ corresponding to a much lower $\Delta\theta$(world). However, the different proportion of sensible and latent heat flux in the model and in the atmosphere is likely to have an impact on the phenomenon we are trying to model - a larger part of the entropy flux goes into warming of the boundary layer instead of being saved as latent heat for future release in the updraft. Since the latter mechanism reinforces the updraft we may expect here a weaker development than occurs in reality, especially if the air is sub-saturated at sea level, so that the entropy flux has an even larger component of latent heat.

The drag coefficient C_E is here assumed equal to the momentum drag coefficient C_D that appears in the momentum flux:

$$F_{(u,v)} = C_D \left[(u,v) \sqrt{u^2+v^2} \right]_{j=1}$$

and

$$C_E = C_D = 1.1 \cdot 10^{-3} + 4 \cdot 10^{-5} \left(\sqrt{u^2+v^2} \right)_{j=1} \qquad (*)$$

A summary of the experiments presented in this chapter is in Table 3.1. The first experiment that we show (labeled I) is run with $C_E = 0$, so as to provide a control experiment for the rest of the section. It

---

(*) This form is appropriate for marine environment. Recall that the one experiment with drag shown in sect. 2.3 (exp.A3) was run with a constant $C_D = .004$; the drag coefficient that we use here increases with the perturbation and does not reach that value until $|\vec{u}'| \simeq 70$ m/sec.

has 3,000 km wavelength and r=0, i.e. it is similar to exp.D of sect. 2.3, except that it has frictional drag at the surface in the form specified above, and the horizontal resolution is 30. Km instead of 50.Km. The horizontal 'mixing length' ℓ_H defined in sect 2.3 remains 50. Km. The initial perturbation is the same as in sect.2.3 (see pag.68)

Fig. 3.5 shows the evolution of the growth rate calculated from the perturbation kinetic energy as a function of time. Comparision with fig 2.23 will show that no difference appears until 50. hrs, after which time a slight decrease of the growth rate due to frictional dissipation takes place. There are no surprises in the evolution of the disturbance, that is shown at selected times in fig. 3.7.

Fig 3.6 shows the growth rate vs. time for exp. FI2, which is the same as I except that heat and moisture fluxes are active and an air-sea temperature difference $\overline{\Delta\theta}$ =10 K is imposed in the base state. The evolution follows that of exp. I until about 65. hrs, after which time faster growth takes place. The form of the solution is shown in fig.3.8. At 50. and 60. hours there is only a slightly stronger wind field at the surface, presumably due to the increased horizontal thermal gradients. At 70. hrs the strong increase in w and one-grid-point oscillations in the wind field suggest that convection is occurring. As we assumed in the previous section removal of heat from the boundary layer occurs in the updraft and we can begin to see at 70. hrs that this process is taking place. In the following 20. hrs distinct narrow updrafts are evident, embedded in a larger area of

weak positive w, and, associated with them, distinct maxima of vorticity and potential temperature are observed. At 100 hrs all the updrafts have collapsed into one, which is strong and narrow enough that its effect is clearly seen on the zonal wind field as well as in the vorticity maximum at the surface and in the thermal maximum, all of which coincide with the minimum surface pressure and extend to the middle troposphere (see also fig. 3.9). Note that at this time the 310 K isentropic (*) surface is into the ground, so the sign of the surface flux at the center of the perturbation is reversed and only the low-level convergence feeds heat into the updraft. In the next 30. hrs the inner warm core of the cyclone extends to higher levels but it also spreads out. The vertical velocities are actually weaker than they were at 100. hrs but the updraft becomes wider. The thermal structure is suggestive of a tropical storm and the wind field itself can be looked at as the superposition of one of the 'moist baroclinic' modes of Ch. 2 and an entity resembling a shallow hurricane, as seen in fig.3.10 where the difference of meridional wind fields of exp. FI2 and I at the same hours are shown. This '2-D hurricane', being a shallow feature, is advected by the low-level wind, and the whole wave appears to be moving with it. Fig.3.11 shows the location of the 0.

(*) The flux is determined by the moist entropy ϑ_e which for saturated air at 310 K in the model's thermodynamics is 377.5 K. Since the updraft is saturated (see relative humidity in fig.3.14) and the 'sea' relative humidity is 100% the argument can be made with either ϑ or ϑ_e as the ϑ_e field in fig.3.9 confirms.

m/s isotach of meridional wind at the lowest level versus time. The largest westward displacement, that occurs between 100. and 110. hours on the western side, and 20. hours later at the eastern edge of the southerly winds, corresponds to a phase speed of 15. Km/hr $\simeq$ 4.2 m/s slower than the mid-level zonal wind. This is a point of qualitative disagreement with the two-level model of the previous section. Given the more realistic features of the numerical model we would expect its results to be closer to reality. Observations show (Sanders,1986) that the more rapidly growing bombs tend to travel faster, although this is not a general feature, while in the model an increased heat flux seems to induce a slower phase speed (the westward displacement relative to the mid-level wind is larger with increasing $\overline{\Delta\theta}$). The only point in which the numerical model is weaker than the two level is the relative amount of sensible to latent heat in the entropy flux, as we mentioned earlier, and this point should be further explored, possibly with a 3-D model using a realistic thermodynamics (recall that we are forced to use a linearized saturation law in order to be consistent with a constant meridional gradient of mixing ratio, which is all a 2-D model can do)

The phase of rapid growth seems coincident with the occurrence of convection, vertical or slantwise, in the model. Initially the wind is only zonal and the model has zero resolution on the meridional plane, so there cannot be any slantwise convection. As the meridional wind increases, the surface normal to the wind acquires a non-trivial projection on the x-z plane but still only very long wavelengths of

symmetric modes can be resolved, while it is known that the shortest are the most unstable. Fig. 3.14 shows that at 60. hrs, when individual updrafts can already be identified in the w field (and in the relative humidity) the buoyancy for saturated vertical motion $B_{sat}=\left(\theta_z+\frac{L}{c_p\bar{\pi}}q_{v_z}^{sat}\right)\frac{g}{\theta_0}$ is positive, while the equivalent potential vorticity q_e is negative, in the interior and they are both negative at the lowest level, where direct heating is applied. Later on (see 90. hrs. in fig. 3.14) a region of negative vertical buoyancy is formed in both I and FI2 where the ϑ perturbation decreases with height. Neither this nor the interior negative q_e region seem to have any effect on exp. I or exp. FI2. Ten hours later a region of unstable air (both vertically and slantwise) extends continuously over the depth of the troposphere. The main updraft is located in the same position and the inner core of the perturbation reaches the upper levels of the model. At this same time, which is the beginning of the phase of fast growth (see fig.3.6), the domain integrated 'symmetric' conversion term $\bar{u}_z\,\overline{u'w'}^{xz}$ in the KE equation becomes positive and remains so until the end of the integration, with values an order of magnitude smaller than the baroclinic terms. In the later stages, when the inner core has become broad, and the growth rate is beginning to decline, both the vertical and the slantwise stability are positive again where the air is saturated (not shown).

Fig. 3.12 shows that an increase of the air-sea temperature difference changes the maximum growth rate reached and also the time of onset of the phase of rapid growth. The same effect is observed in fig

3.13 where the minimum surface pressure is plotted for runs with different $\overline{\Delta\theta}$. In the first stage the low pressure center is modestly deeper for stronger heating and the KE of the perturbation is not significantly altered. The fields in fig. 3.8 show that in this phase the effect of surface heating is confined to the lowest levels of the atmosphere, that are directly subjected to the heat flux. Later on a very rapid growth occurs, with deepening approximately linear with time, and hurricane-like features in the temperature, wind and potential vorticity. The pressure drop during this phase reaches values above the conventional threshold for exposive cyclones, that is $\simeq$ 19.5 mb/24 hrs at the latitude (45^{o}) at which the model is run, for $\overline{\Delta\theta} \gtrsim 15$ K.

The environmental stability influences both the maximum growth rate achieved and the time of onset of the 'explosive' phase of growth, as shown by the sequence of experiments L,FL1,FL2,FL3 (see table 3.1), whose growth-rate is shown in Fig. 3.15, and minimum surface pressure in Fig. 3.16, versus time. These are runs in which the base state has a negative r, corresponding to neutrality for saturated vertical displacement. Comparision with 3.12,3.13 shows that each of them is faster and deeper than its counterpart at r=0.

The evolution of the perturbation in exp. FL2 is shown from 30. hrs in fig. 3.17 and it follows the same pattern as FI2, with the exception that the phase of explosive growth begins sooner. With this base state $q_e < o$ everywhere initially, which is allowed within a 2-D model. In a 3-D world we would expect widespread slantwise convection

to restore a condition of symmetric neutrality in a short time and then the evolution to follow that of FI2. The relative importance of slantwise and vertical convection in the evolution cannot be assessed in a model that does not resolve the most unstable symmetric modes. The only effect of the reduced stability is that, as already seen in the 2-level model, the moist baroclinic wave grows faster - whether this has a direct causal effect on the onset of the 'explosive' stage we cannot say at this point, but it may be observed in fig.s 3.13 and 3.16 that the change of pace from the initial 'exponential' growth to the later 'linear' growth seems to take place in the neighborhood of 10. mb in all but the weakest cases shown, thus suggesting an amplitude dependence for this transition. A possible explanation of this behavior is that in the first stage only the vertical advection by the large-scale flow can transport heat upward of the lowest levels of the atmosphere, and weaker disturbances take longer to do so. Once the latent heat acquired in the boundary layer is released, and begins to modify the thermal structure in the updraft, convection can take place. Its relative importance for the vertical heat transport at this stage is uncertain, but its kinematic consequences on the structure of the solution are evident in the subsequent evolution. The updraft becomes narrower, more intense and more effective in the transport of heat. Notice that the collapse of the updraft region in this stage is in direct contrast with the 2-level model - there we directly applied heat to the middle of the troposphere, here the system has to organize its own means to do so. This result should be compared with the result of Davis and Emanuel,1988 that show that the correlation between deepening

rate and heat flux undergoes a transition from $\simeq .5$ to $\simeq .8$ when the deepening rate goes above 1.2 bergerons (*). Since we initialize all our experiments with the same amplitude of the perturbation a growth-rate threshold is equivalent to an amplitude threshold for our experiments. On the other hand Rotunno and Emanuel,1987 have shown that tropical hurricanes need a finite amplitude initiator to begin the development and the behavior of our '2-D hurricane' seems consistent with this conclusion.

Finally Fig 3.18 shows the wavelength dependence of the growth rate. The curves are the pressure drop vs. time for experiments similar to FI2 (i.e. r=0 , $\overline{\Delta\theta} = 10$ K), but for varying length of the domain, at the same (30. Km) resolution. The growth rate seems to be levelling off at 3600. Km, but we could not explore further for lack of computer time.

(*) 1 bergeron is the threshold for 'bombs' as defined in Sanders and Gyakum,1980. Its value varies with the sine of latitude and is equal to a pressure drop of 24. mb in 24. hrs at 60^0 N

T A B L E 3.1

EXP	r	wavel.	$\overline{\Delta\theta}$	comments
I	0.	3,000 Km	--	slantwise neutral - as in D plus momentum drag
FI0	0.	"	0 K	as I plus heat flux at the bottom
FI1	0.	"	5 K	"
FI2	0.	"	10 K	"
FI3	0.	"	15 K	"
FI4	0.	"	20 K	"
L	-.07	"	--	vertically neutral - as in F plus momentum drag
FL1	-.07	"	5 K	as L plus heat flux at the bottom
FL2	-.07	"	10 K	"
FL3	-.07	"	15 K	"

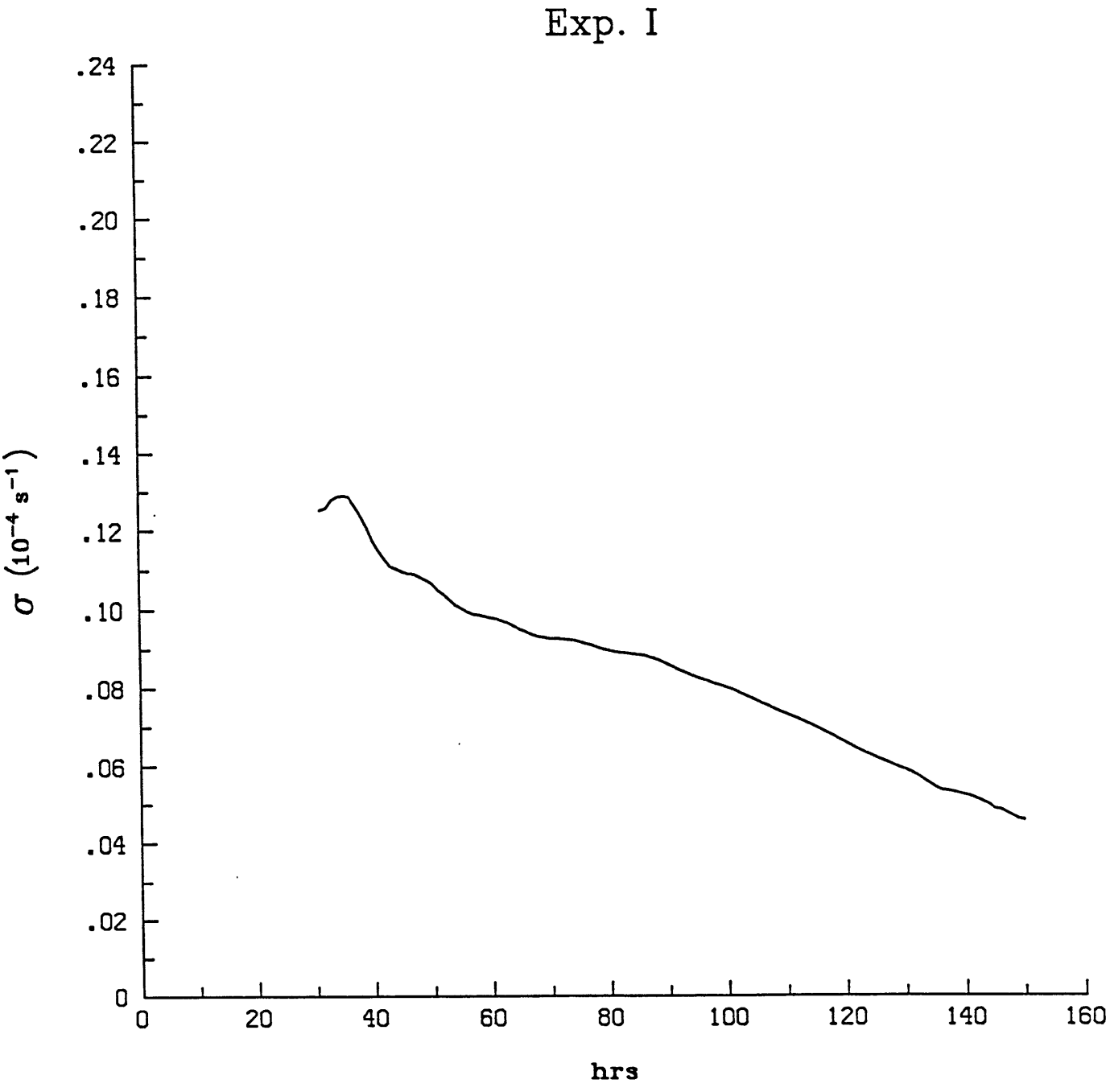


Fig.3.5 - growth rate σ vs. time for exp. I

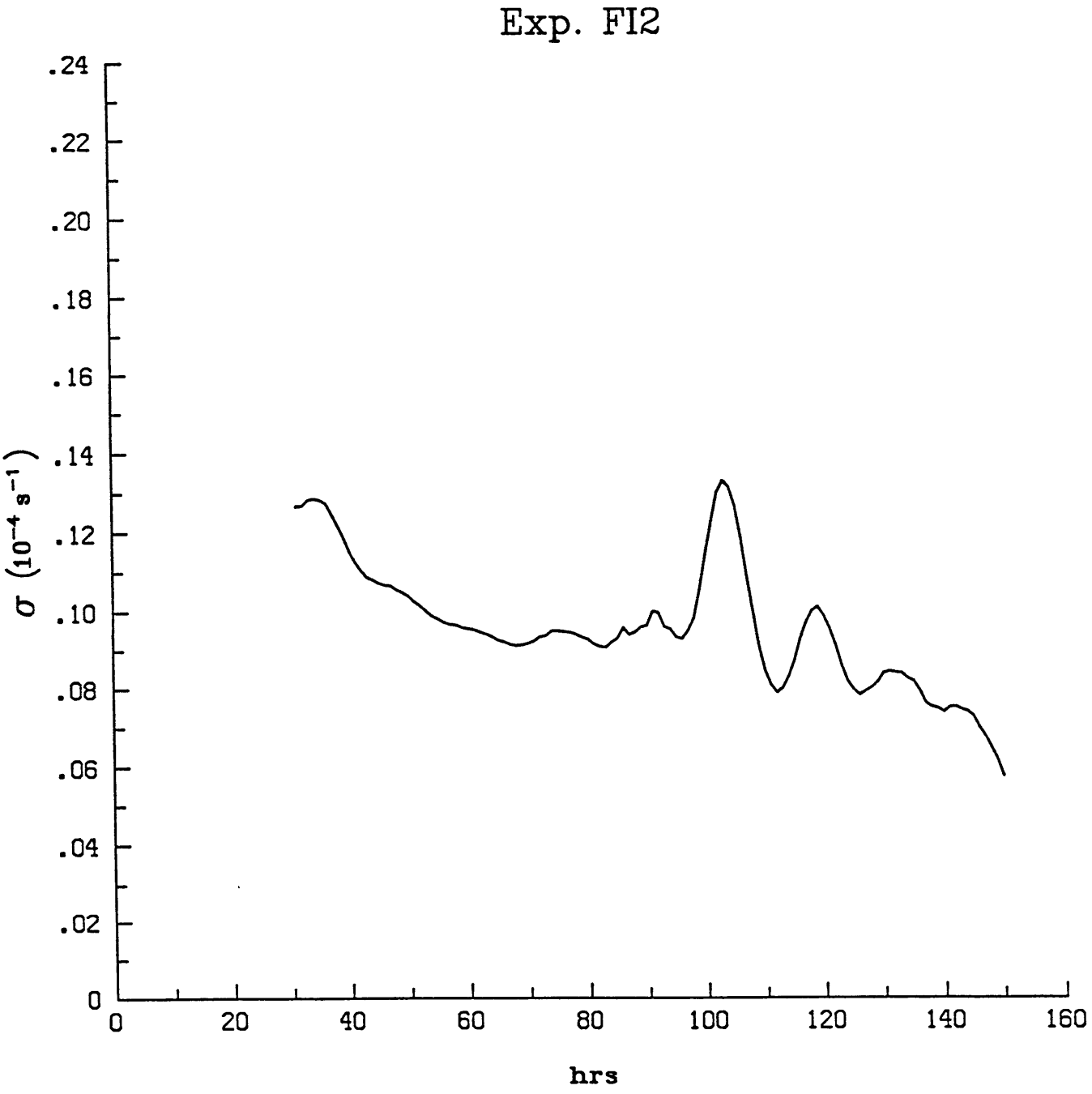


Fig.3.6 - same as fig.3.5 but for exp. FI2

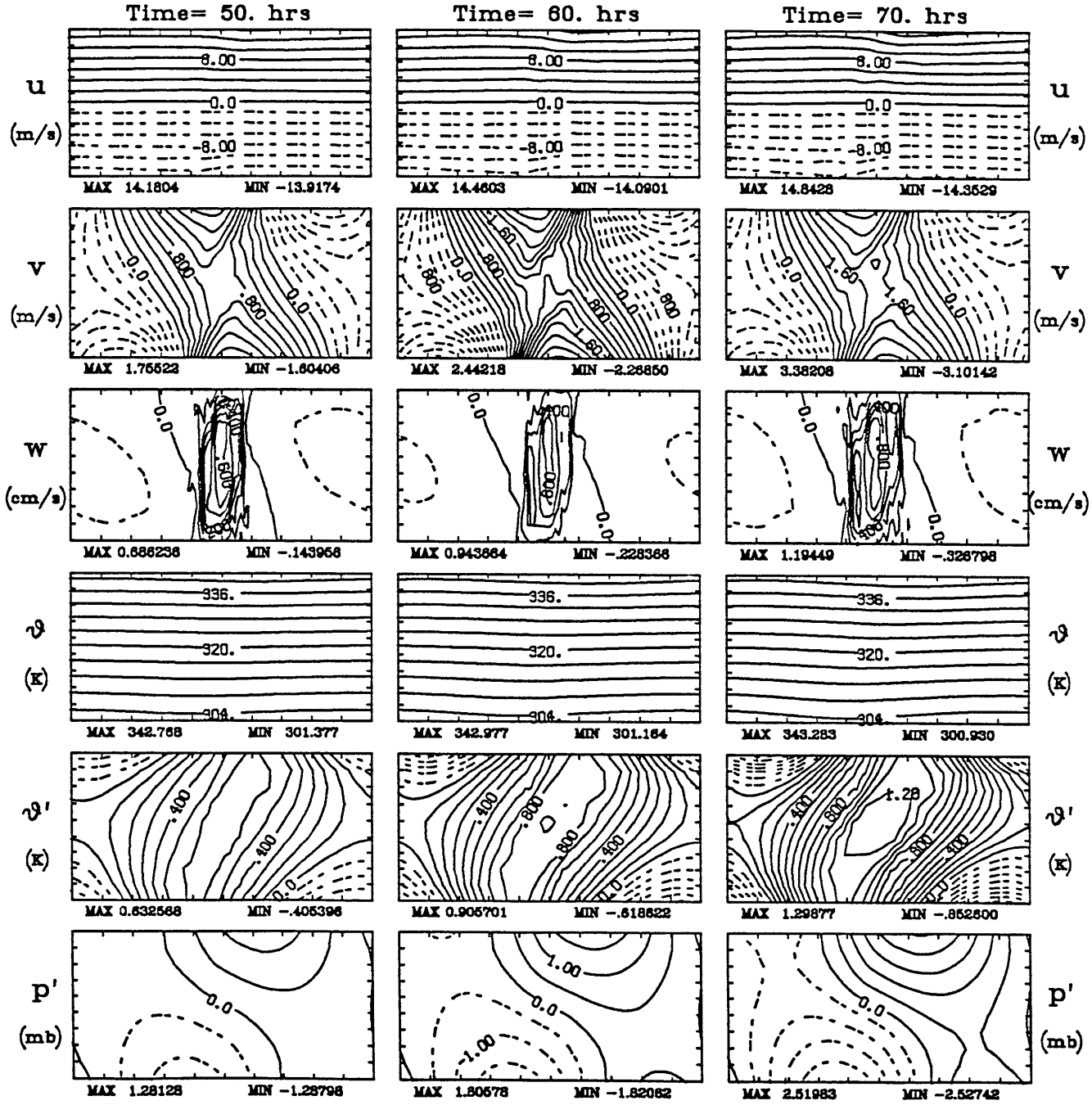


Fig.3.7 - u,v,w, ϑ, ϑ', p fields for exp.I, shown every 10. hours from 50. hrs to 130. hrs. Contour interval is not constant with time.

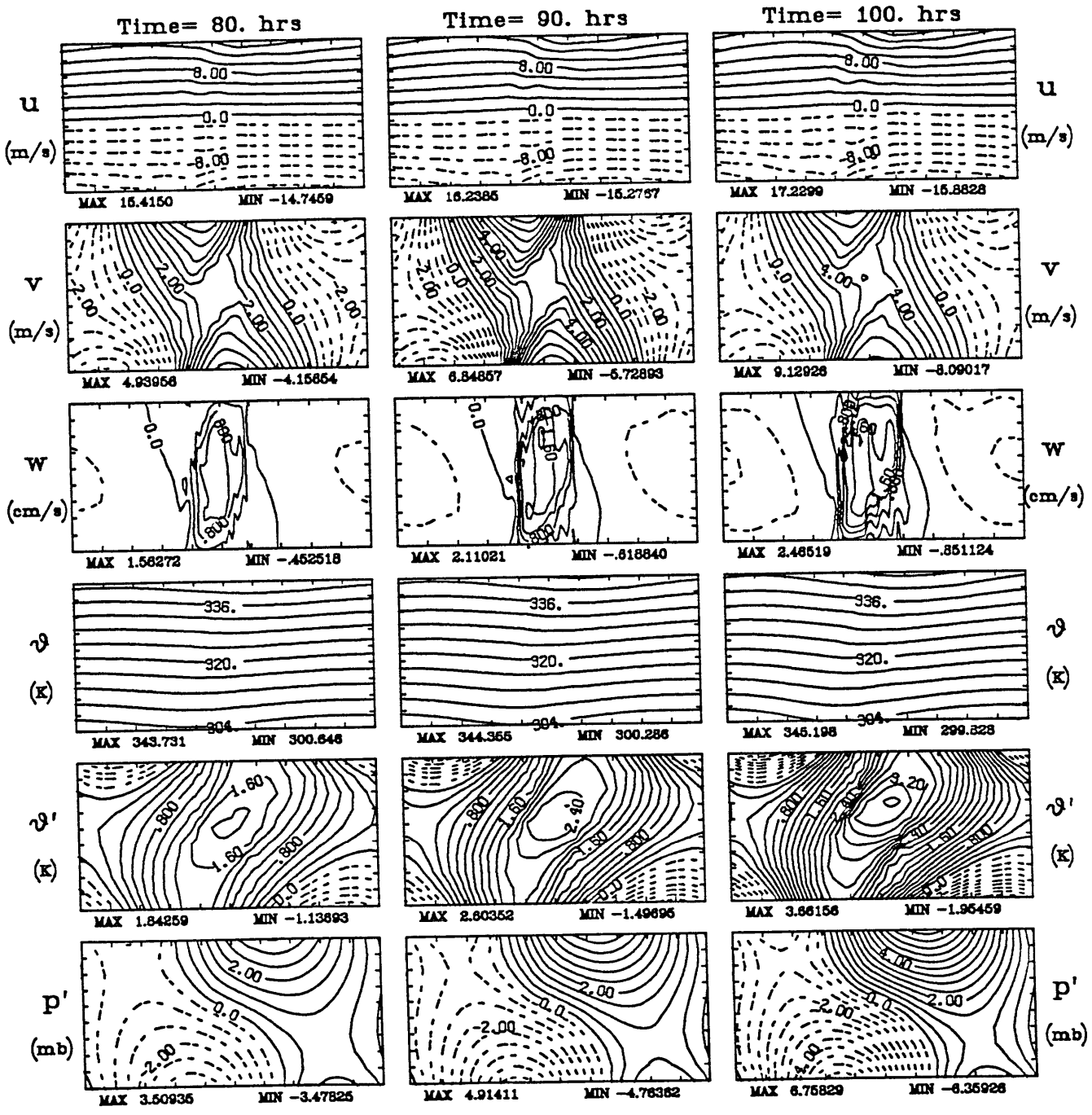

Time= 80. hrs
Time= 90. hrs
Time= 100. hrs
u
(m/s)
MAX 15.4150 MIN -14.7459
MAX 16.2386 MIN -15.2757
MAX 17.2299 MIN -15.8828
v
(m/s)
MAX 4.93956 MIN -4.15654
MAX 6.84857 MIN -5.72893
MAX 9.12928 MIN -8.09017
w
(cm/s)
MAX 1.56272 MIN -.452518
MAX 2.11021 MIN -.618840
MAX 2.46519 MIN -.851124
ϑ
(K)
MAX 343.731 MIN 300.648
MAX 344.365 MIN 300.286
MAX 345.198 MIN 299.828
ϑ'
(K)
MAX 1.84259 MIN -1.13693
MAX 2.60352 MIN -1.49696
MAX 3.66156 MIN -1.96459
p'
(mb)
MAX 3.50935 MIN -3.47825
MAX 4.91411 MIN -4.76362
MAX 6.75829 MIN -6.35926

Fig.3.7 (cont)

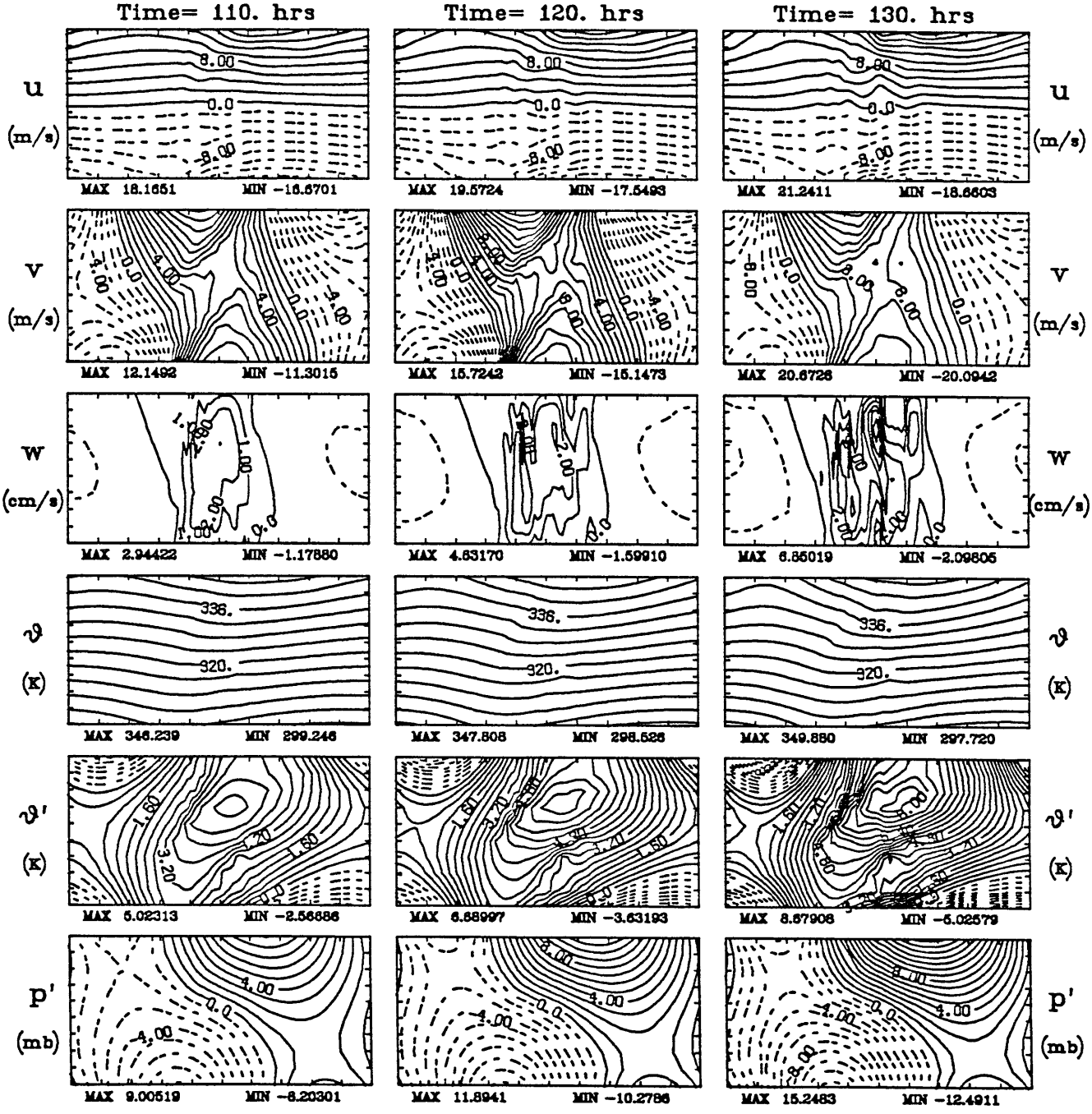

Time= 110. hrs
Time= 120. hrs
Time= 130. hrs
u
(m/s)
MAX 18.1651 MIN -16.6701
MAX 19.5724 MIN -17.5493
MAX 21.2411 MIN -18.6603
v
(m/s)
MAX 12.1492 MIN -11.3015
MAX 15.7242 MIN -15.1473
MAX 20.6726 MIN -20.0942
w
(cm/s)
MAX 2.94422 MIN -1.17880
MAX 4.63170 MIN -1.59910
MAX 6.85019 MIN -2.09805
ϑ
(K)
MAX 346.239 MIN 299.246
MAX 347.808 MIN 298.526
MAX 349.880 MIN 297.720
ϑ'
(K)
MAX 5.02313 MIN -2.56686
MAX 6.68997 MIN -3.63193
MAX 8.57908 MIN -5.02579
p'
(mb)
MAX 9.00519 MIN -8.20301
MAX 11.8941 MIN -10.2786
MAX 15.2483 MIN -12.4911

Fig.3.7 (cont)

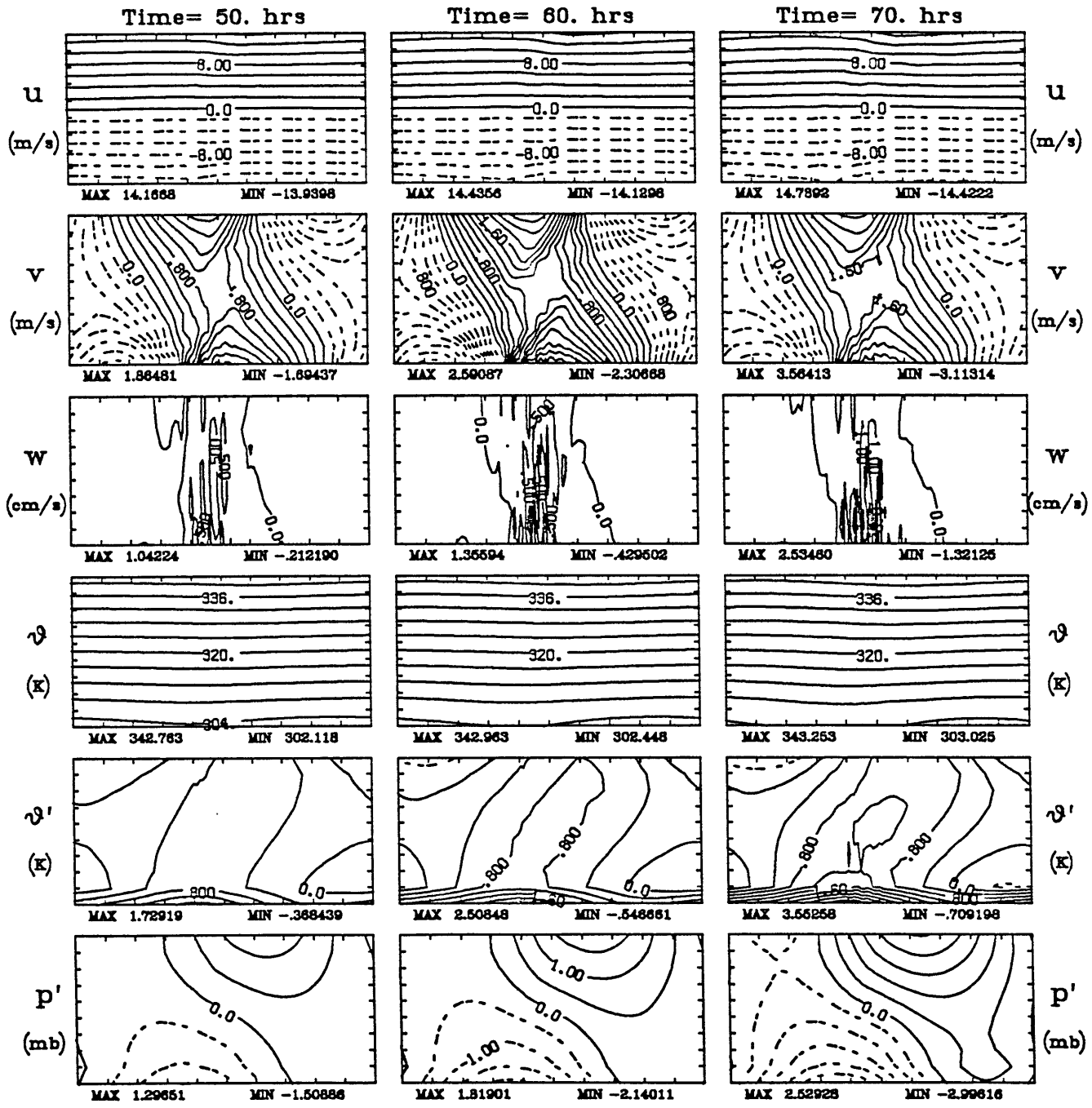


Fig.3.8 - same as fig.3.7 but for exp. FI2

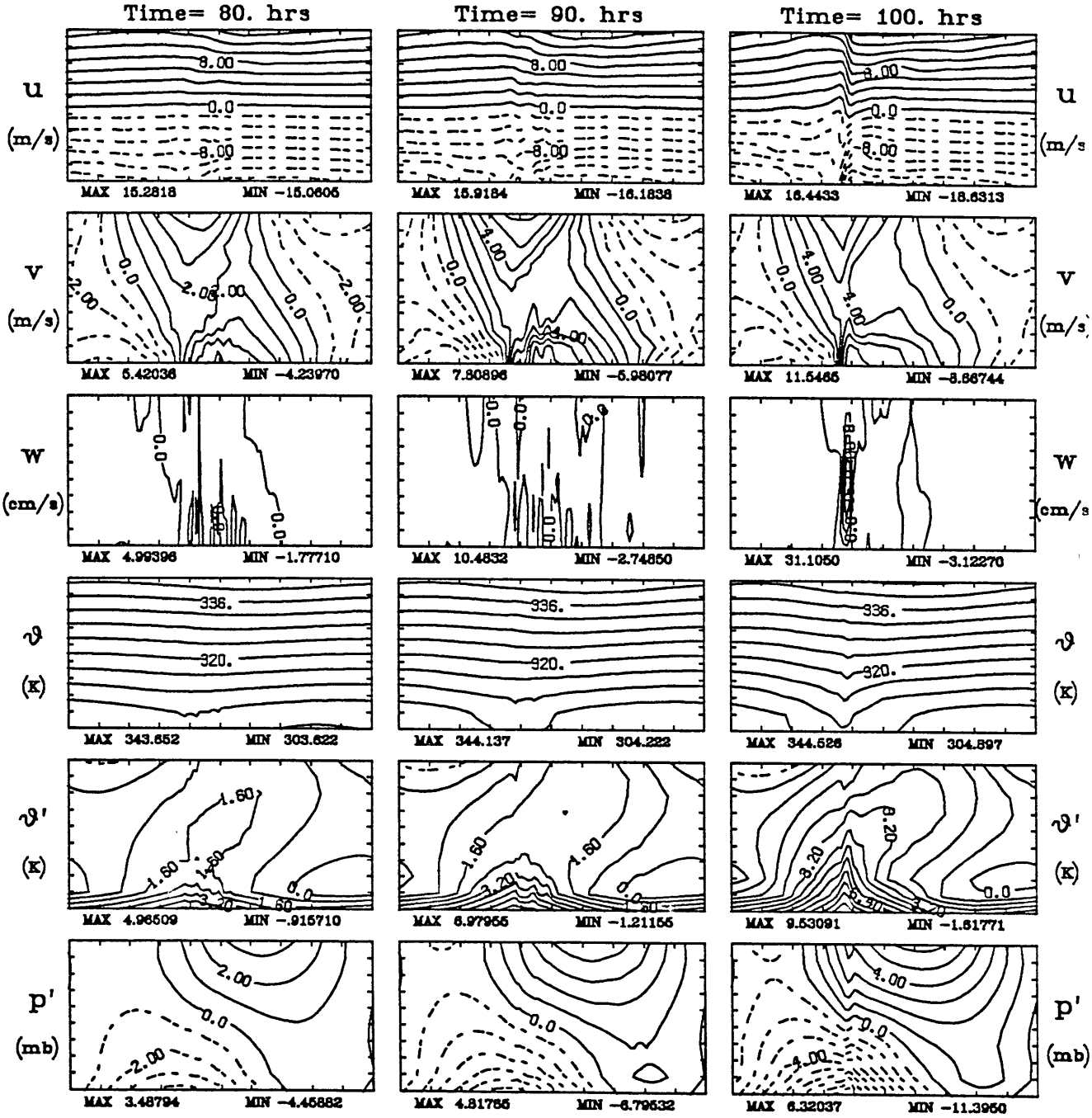

Time= 80. hrs
Time= 90. hrs
Time= 100. hrs
u
(m/s)
MAX 15.2818 MIN -15.0606
MAX 15.9184 MIN -16.1838
MAX 16.4433 MIN -18.6313
v
(m/s)
MAX 5.42036 MIN -4.23970
MAX 7.80896 MIN -5.98077
MAX 11.5466 MIN -8.66744
w
(cm/s)
MAX 4.99396 MIN -1.77710
MAX 10.4832 MIN -2.74650
MAX 31.1050 MIN -3.12270
ϑ
(K)
MAX 343.652 MIN 303.622
MAX 344.137 MIN 304.222
MAX 344.526 MIN 304.897
ϑ'
(K)
MAX 4.96509 MIN -.915710
MAX 6.97955 MIN -1.21155
MAX 9.53091 MIN -1.61771
p'
(mb)
MAX 3.48794 MIN -4.45882
MAX 4.81755 MIN -6.79532
MAX 6.32037 MIN -11.3950

Fig.3.8 (cont)

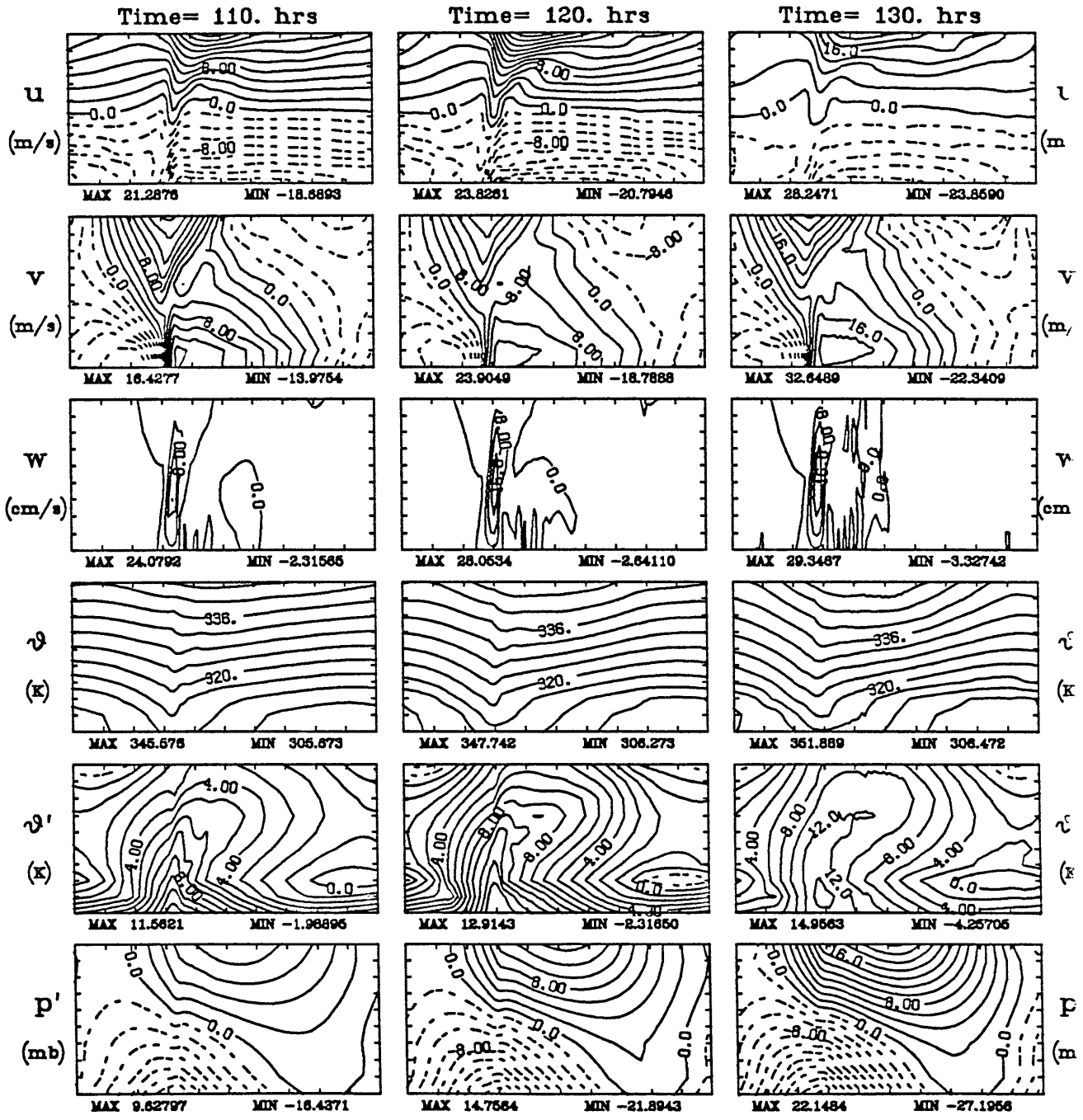

Time= 110. hrs
Time= 120. hrs
Time= 130. hrs
u
(m/s)
MAX 21.2876 MIN -18.6893
MAX 23.8261 MIN -20.7946
MAX 28.2471 MIN -23.8590
v
(m/s)
MAX 16.4277 MIN -13.9754
MAX 23.9049 MIN -18.7888
MAX 32.6489 MIN -22.3409
w
(cm/s)
MAX 24.0792 MIN -2.31565
MAX 28.0534 MIN -2.64110
MAX 29.3487 MIN -3.32742
ϑ
(K)
MAX 345.575 MIN 305.873
MAX 347.742 MIN 306.273
MAX 351.889 MIN 306.472
ϑ'
(K)
MAX 11.5621 MIN -1.98896
MAX 12.9143 MIN -2.31650
MAX 14.9563 MIN -4.25705
p'
(mb)
MAX 9.62797 MIN -16.4371
MAX 14.7564 MIN -21.8943
MAX 22.1484 MIN -27.1956

Fig.3.8 (cont)

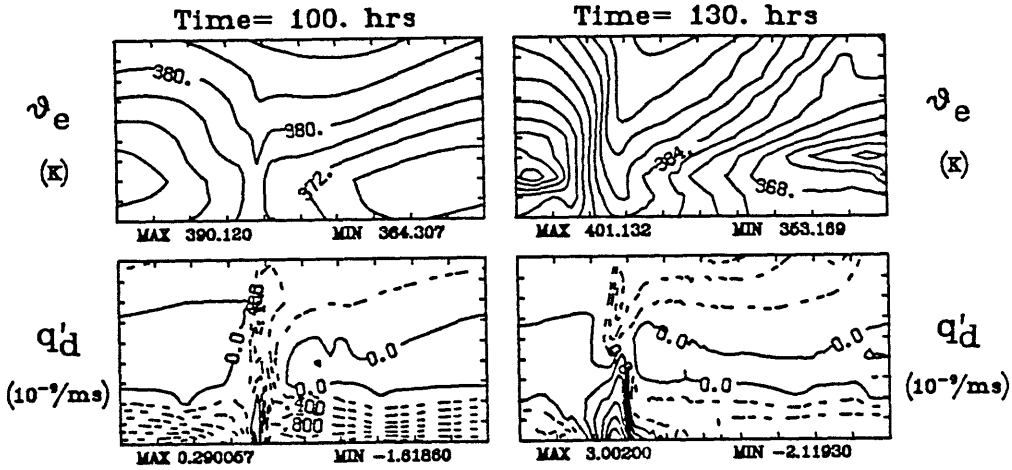


Fig.3.9 - equivalent potential temperature ϑ_e and perturbation potential vorticity q'_d for exp. FI2 at 100. hrs and 130. hrs

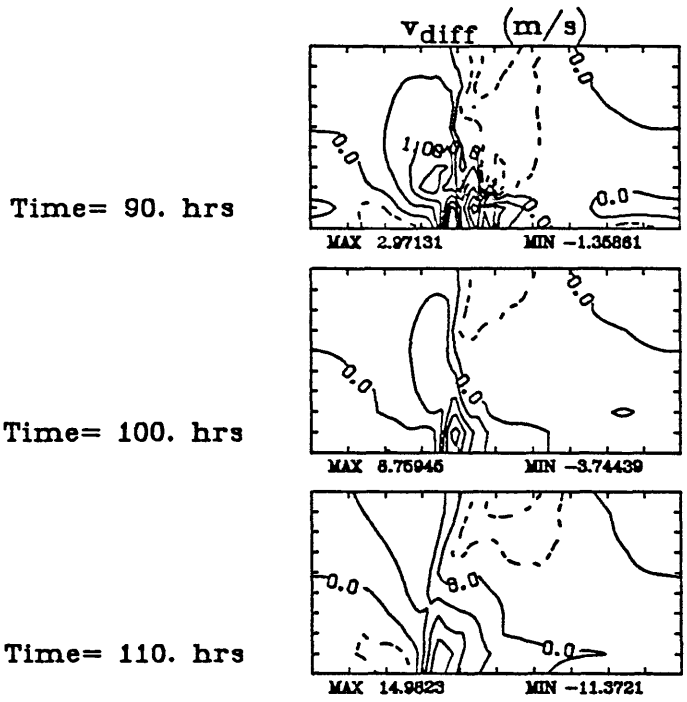


Fig.3.10 - difference in meridional wind field v between exp. FI2 and exp. I at 90,100,110 hrs. The graph shows FI2 minus I

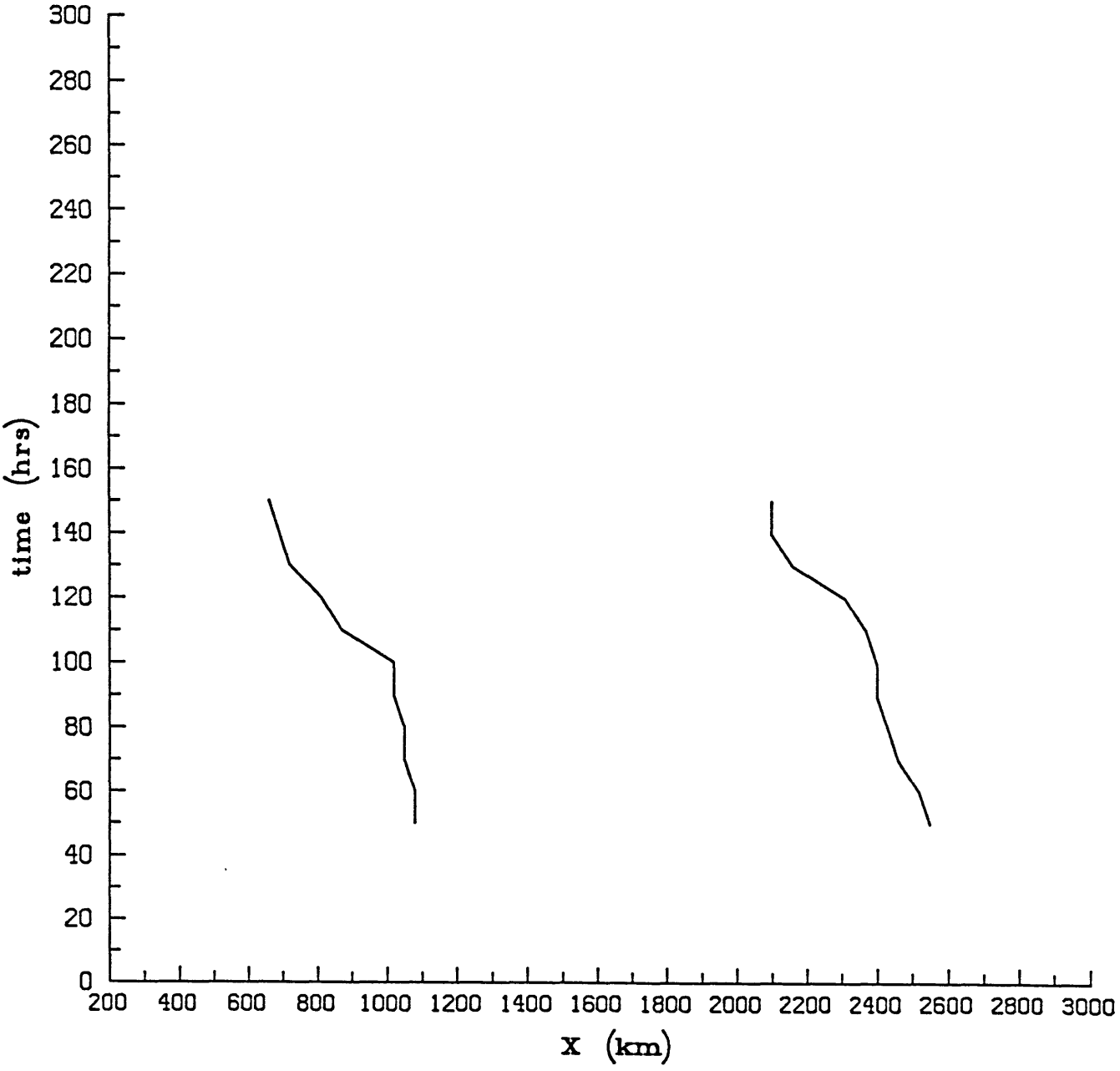


Fig.3.11 - Location of the two 0.m/s isotachs of meridional wind, at the lowest resolved level (500. m height), for exp. FI2, versus time, showing the westward displacement of the disturbance in the frame of reference in which the zonal basic wind is zero at mid-level

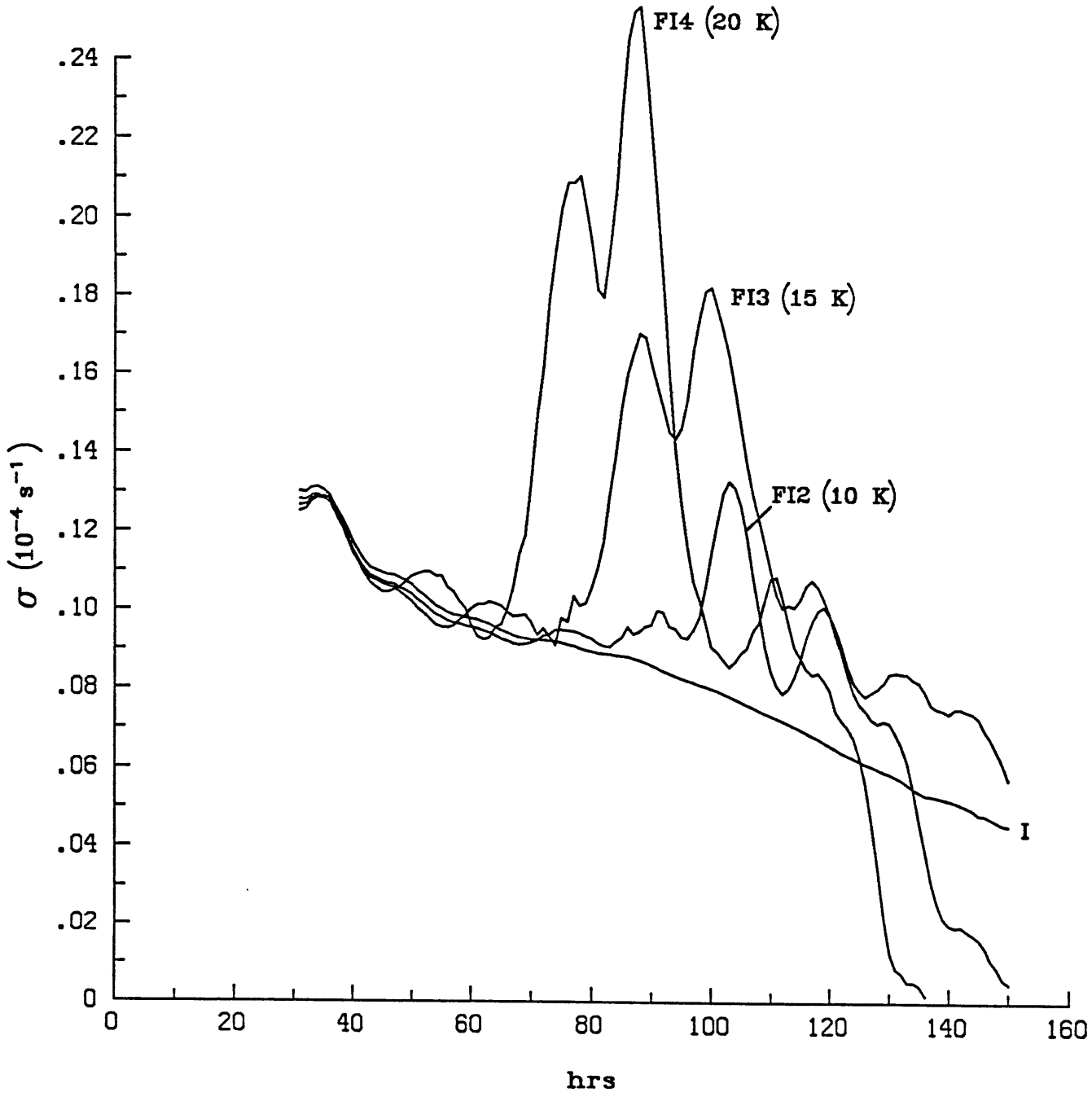


Fig.3.12 - growth rate σ vs. time for exp.s I,FI2,FI3,FI4

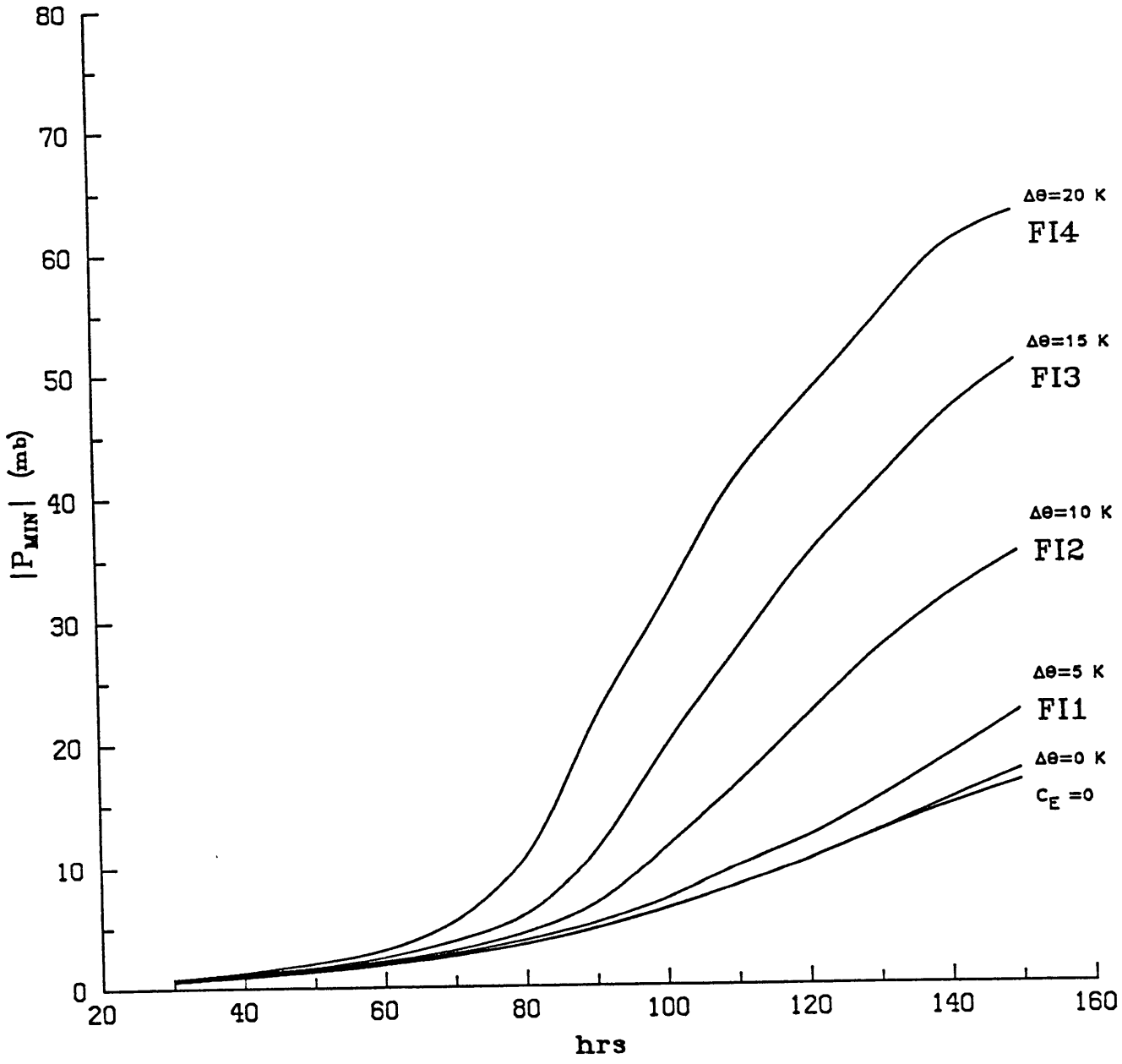


Fig.3.13 - minimum surface pressure vs. time for exp.s I (C_E=0), FI0 ($\overline{\Delta\theta}$ =0 K), FI1,FI2,FI3,FI4

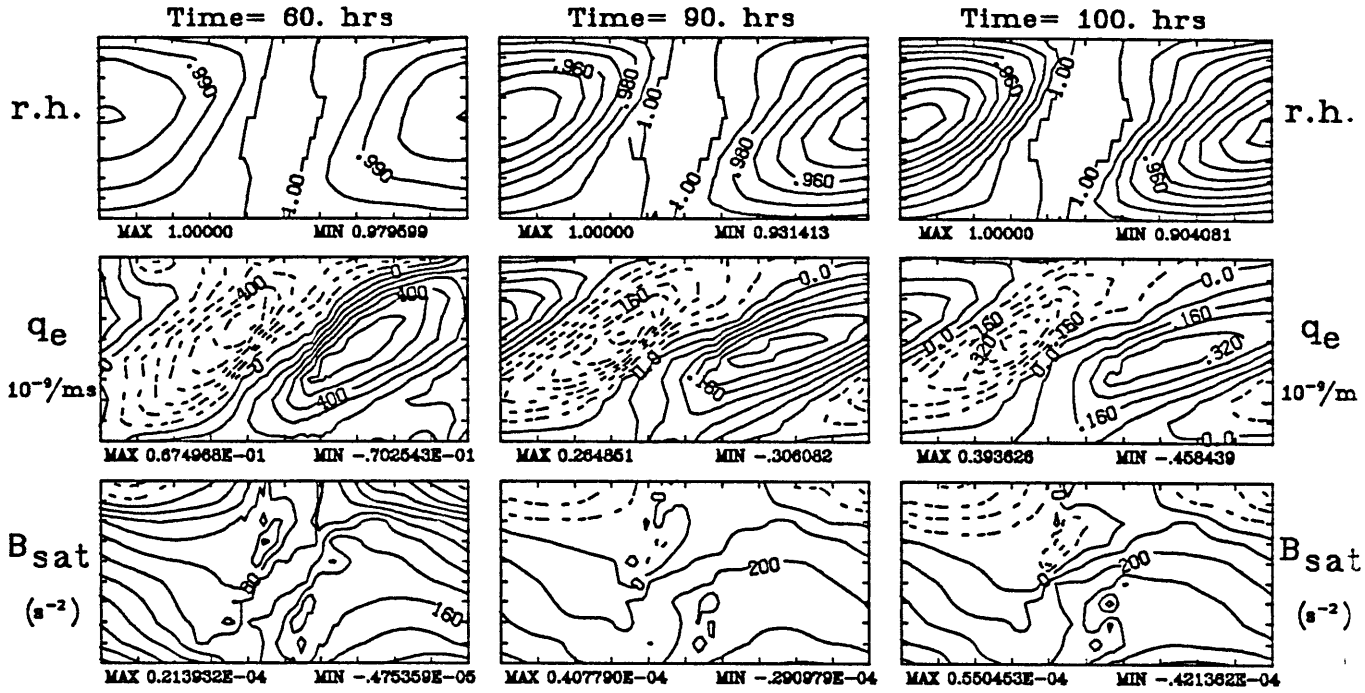


Fig.3.14a - relative humidity, equivalent potential vorticity q_e and buoyancy for saturated vertical motions $B_{sat} = \left(\sigma_z + \frac{L}{c_p \bar{\pi}} q^{sat}_{vz}\right) g/\theta_v$, for exp. I at 60.,90.,100. hrs

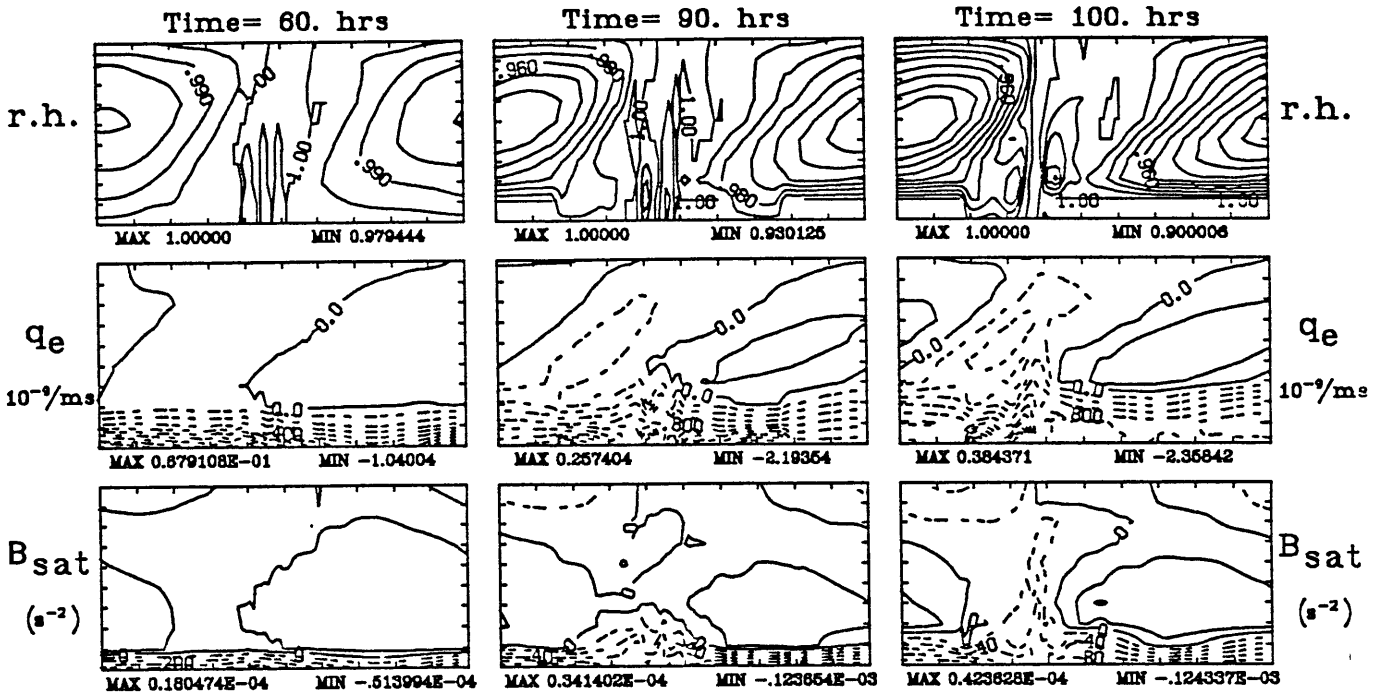


Fig.3.14b - same as a) but for exp. FI2

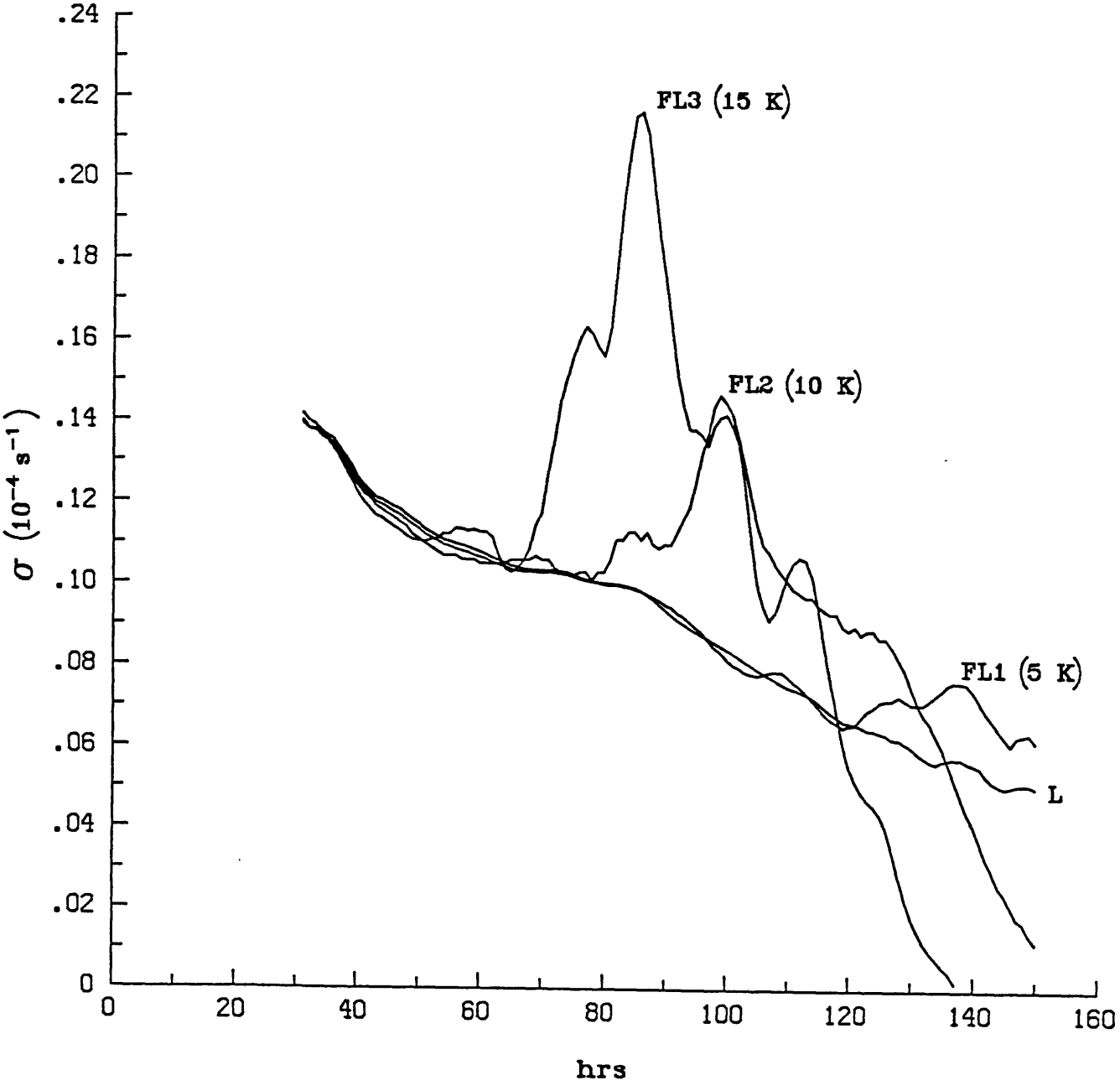


Fig.3.15 - same as fig.3.12 but for exp.s L,FL1,FL2,FL3

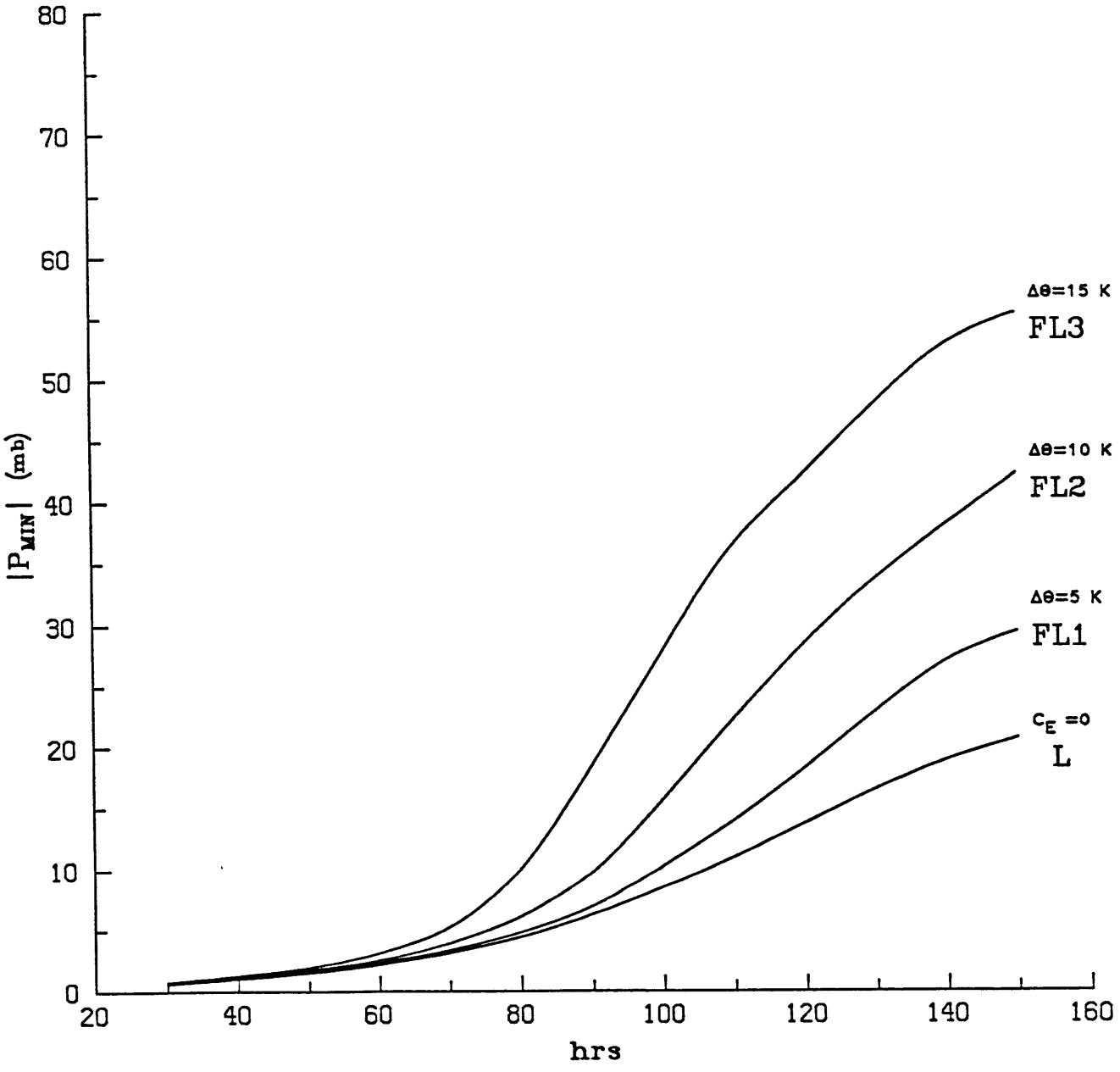


Fig.3.16 - same as fig.3.13 but for exp.s L,FL1,FL2,FL3

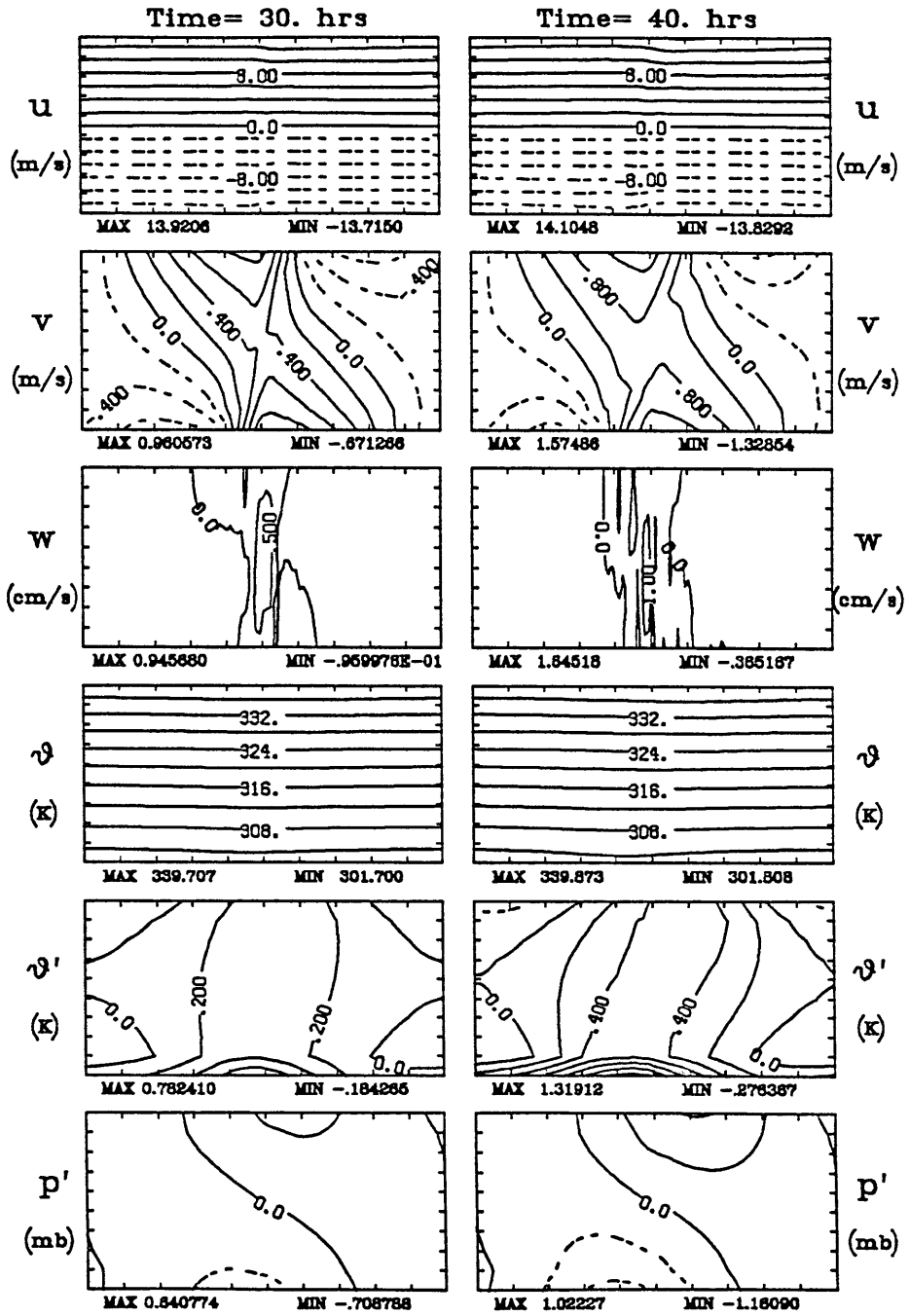


Fig.3.17 - same as fig.3.7 but for exp. FL2 between 30 hrs and 130. hrs

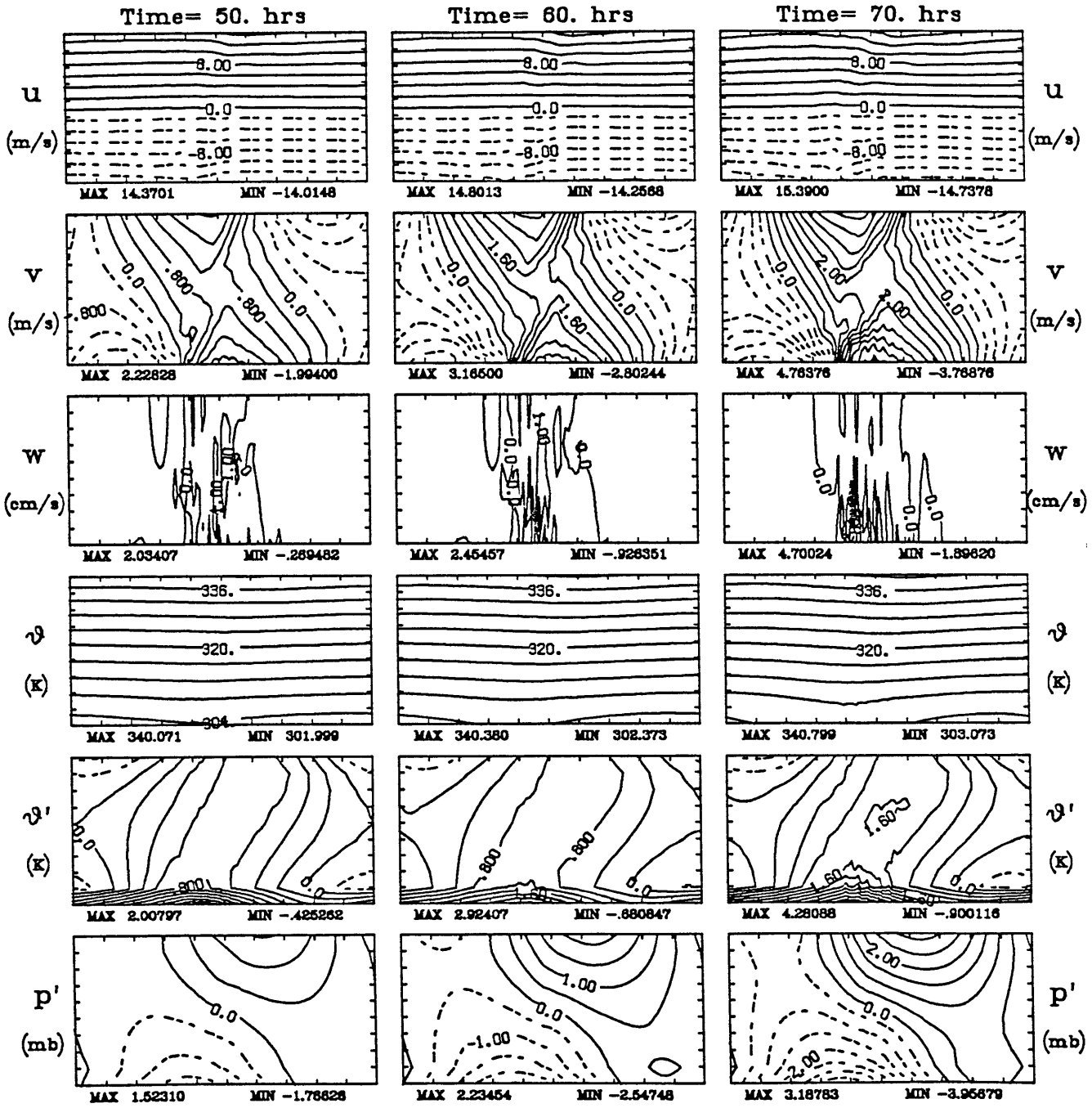

Time= 50. hrs
Time= 60. hrs
Time= 70. hrs
u
(m/s)
8.00
0.0
-8.00
MAX 14.3701 MIN -14.0148
MAX 14.8013 MIN -14.2568
MAX 15.3900 MIN -14.7378
v
(m/s)
MAX 2.22828 MIN -1.99400
MAX 3.16500 MIN -2.80244
MAX 4.76376 MIN -3.76876
w
(cm/s)
MAX 2.03407 MIN -.269482
MAX 2.45457 MIN -.926351
MAX 4.70024 MIN -1.89620
ϑ
(K)
336.
320.
304.
MAX 340.071 MIN 301.999
MAX 340.380 MIN 302.373
MAX 340.799 MIN 303.073
ϑ'
(K)
MAX 2.00797 MIN -.425262
MAX 2.92407 MIN -.880847
MAX 4.28088 MIN -.900116
p'
(mb)
1.00
-1.00
2.00
-2.00
MAX 1.52310 MIN -1.78628
MAX 2.23454 MIN -2.54748
MAX 3.18783 MIN -3.95679

Fig.3.17 (cont)

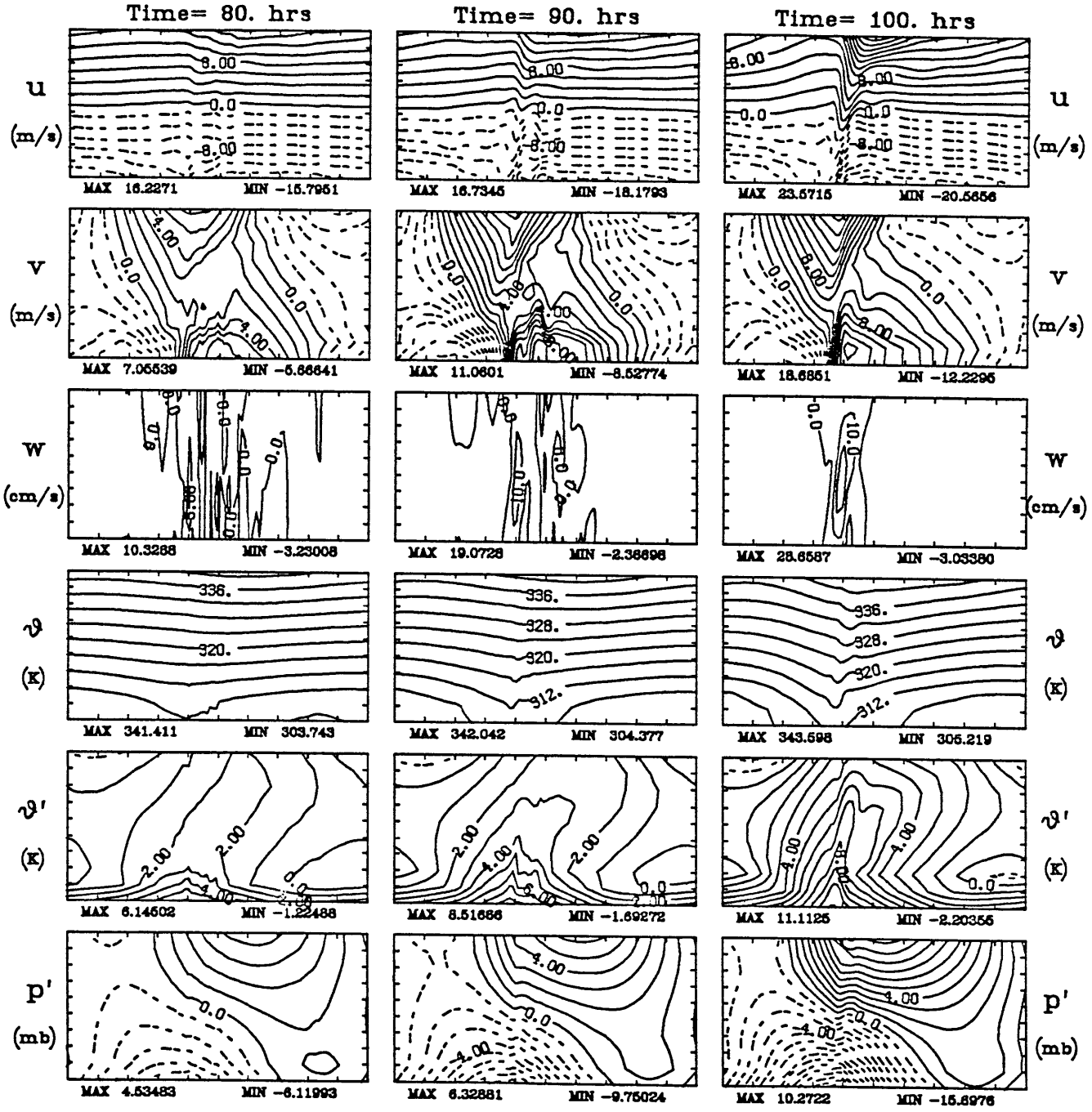

Time= 80. hrs
Time= 90. hrs
Time= 100. hrs
u
(m/s)
MAX 16.2271 MIN -15.7951
MAX 16.7345 MIN -18.1793
MAX 23.5715 MIN -20.5656
v
(m/s)
MAX 7.05539 MIN -5.66641
MAX 11.0601 MIN -8.52774
MAX 18.6851 MIN -12.2295
w
(cm/s)
MAX 10.3268 MIN -3.23008
MAX 19.0728 MIN -2.36898
MAX 28.6587 MIN -3.03380
ϑ
(K)
MAX 341.411 MIN 303.743
MAX 342.042 MIN 304.377
MAX 343.698 MIN 305.219
ϑ'
(K)
MAX 6.14502 MIN -1.22488
MAX 8.51666 MIN -1.69272
MAX 11.1125 MIN -2.20356
p'
(mb)
MAX 4.53483 MIN -6.11993
MAX 6.32881 MIN -9.75024
MAX 10.2722 MIN -15.6976

Fig.3.17 (cont)

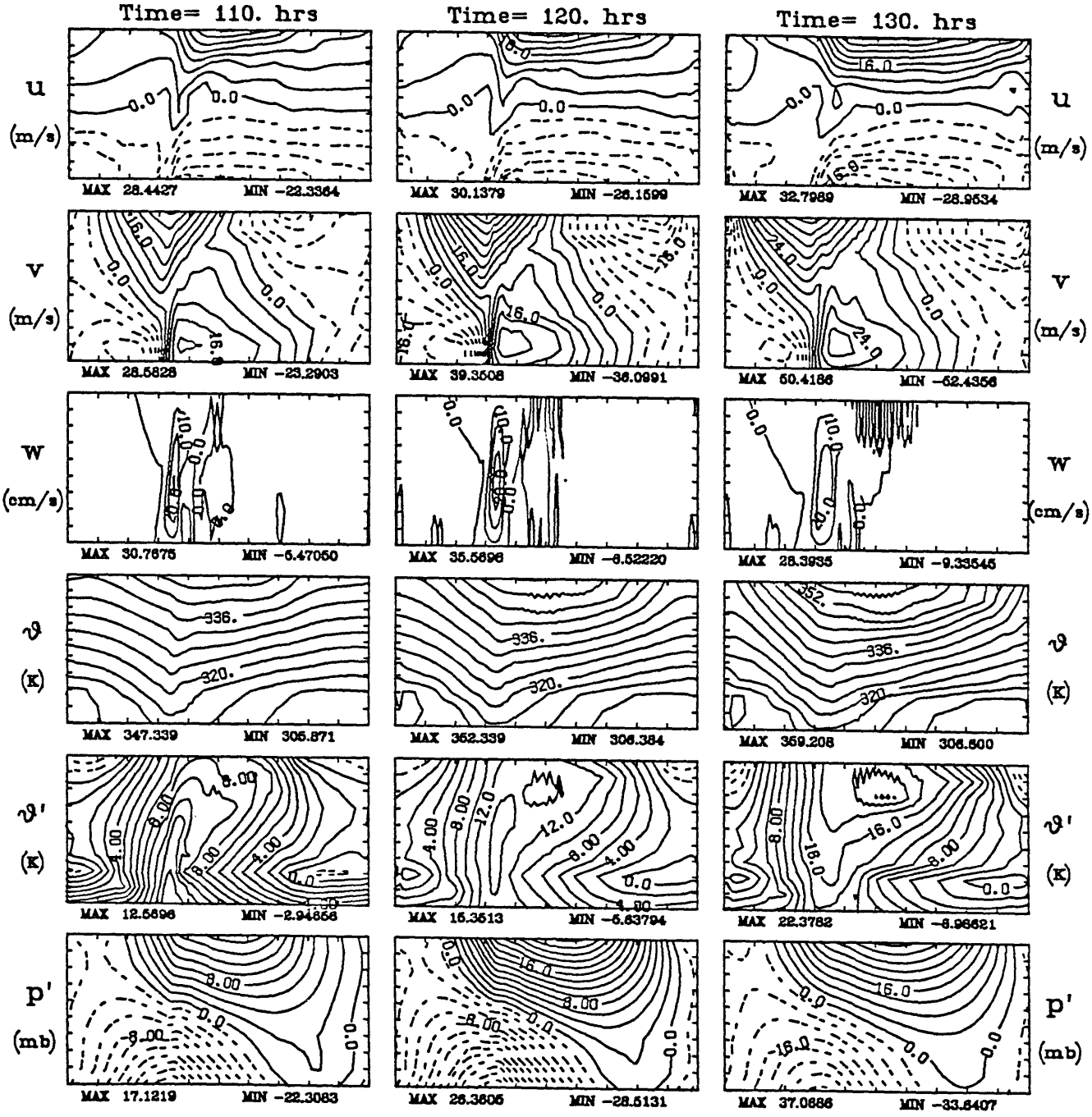

Time= 110. hrs
Time= 120. hrs
Time= 130. hrs
u
(m/s)
MAX 28.4427
MIN -22.3364
MAX 30.1379
MIN -26.1599
MAX 32.7989
MIN -28.9534
v
(m/s)
MAX 28.5828
MIN -23.2903
MAX 39.3508
MIN -36.0991
MAX 50.4186
MIN -62.4356
w
(cm/s)
MAX 30.7675
MIN -6.47050
MAX 35.5696
MIN -6.52220
MAX 28.3935
MIN -9.33545
ϑ
(K)
MAX 347.339
MIN 305.871
MAX 352.339
MIN 306.384
MAX 359.208
MIN 306.500
ϑ'
(K)
MAX 12.5696
MIN -2.94856
MAX 15.3513
MIN -5.83794
MAX 22.3782
MIN -6.96621
p'
(mb)
MAX 17.1219
MIN -22.3083
MAX 26.3605
MIN -28.5131
MAX 37.0886
MIN -33.6407

Fig.3.17 (cont)

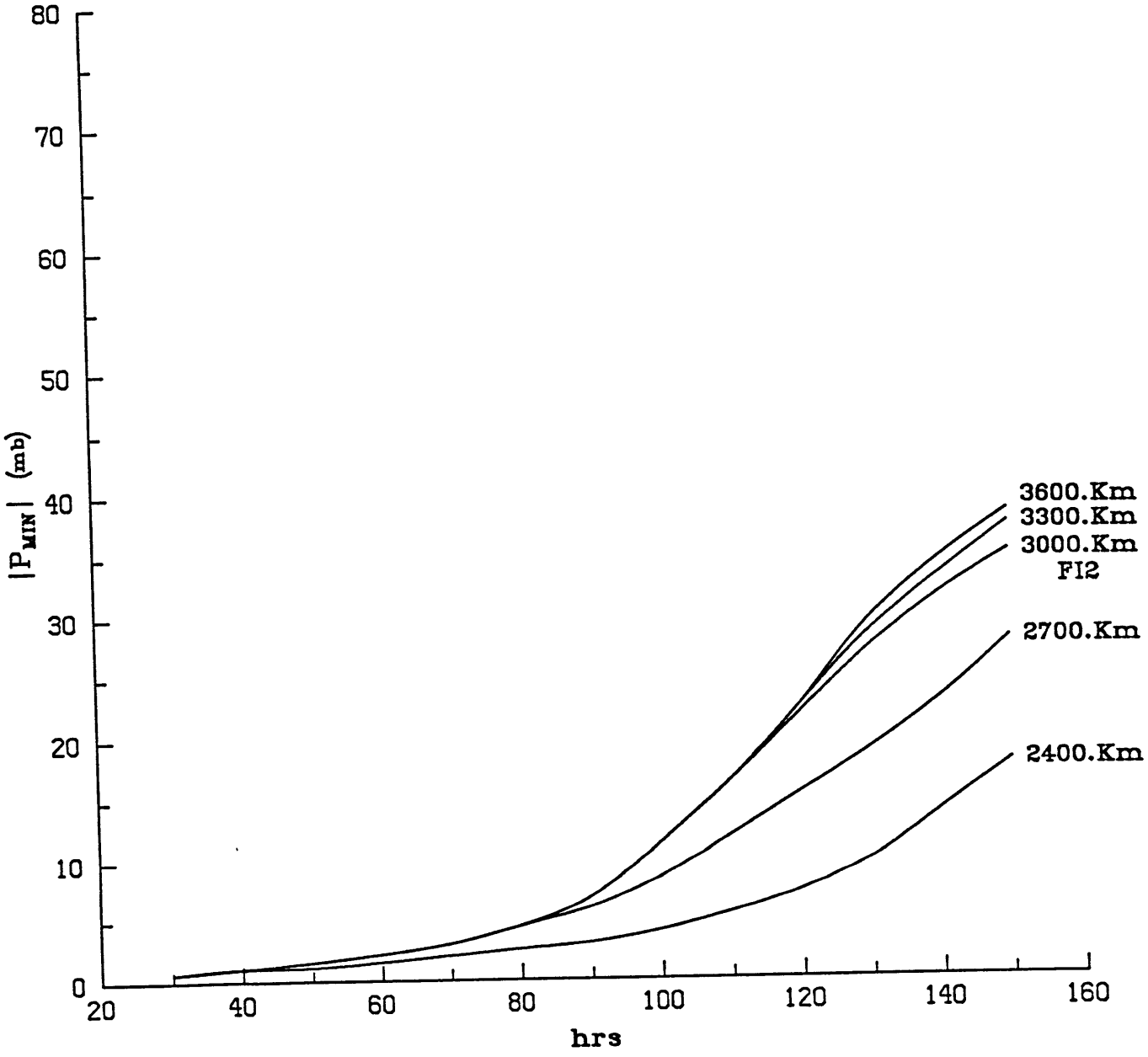


Fig. 3.18 - minimum surface pressure vs. time for experiments similar to FI2 but with varying horizontal length of the domain. Exp. FI2 has a 3000 Km wavelength

4.1

This work consisted of two parts. In the first (chapter 2) we studied the behavior of 2-D Eady waves in a saturated environment. We assumed that a slantwise convective adjustment had taken place to reduce the lapse rate to symmetric neutrality. Therefore we designed a base state with uniform vertical shear and zero equivalent potential vorticity. The release of latent heat was accounted for explicitly in the numerical model (section 2.3) and implicitly, by conserving the equivalent potential temperature in the updraft, in the analytic models (this representation assumes that all upward motion is saturated). The numerical experiments confirmed the finite amplitude semi-geostrophic results as far as the structure of the eigenfunctions is concerned, but revealed that the non-geostrophic contributions ignored in the semi-geostrophic approximation have a large impact on the growth rates in the limit $q_e \to 0$, where the SG system is singular. Specifically the non-dimensional growth rates increase as the Rossby number of the mean flow decreases, as was expected from previous studies of non-geostrophic baroclinic instability, and in a larger measure as the system gets closer to conditional symmetric neutrality. The linearized 2-level PE model reproduces fairly well the growth rates of the numerically simulated waves at small amplitude. The moist baroclinic waves exhibit some features that are commonly observed and not reproduced in dry models, such as an updraft much narrower than the downdraft, a sharp gradient of vertical velocity across the cold front, and frontal collapse occurring at low level first, and not

symmetrically at top and bottom boundaries. The asymmetry of the w field accounts for a much shorter wavelength of the most unstable mode, that is about 60% of the dry most unstable wavelength, with a growth rate about twice as large. A cursory examination of the energy conversion terms reveals that during most of the evolution the 'baroclinic' conversion from mean to eddy potential $\overline{v'\theta'}$ is smaller than the eddy potential to eddy kinetic term $\overline{w'\theta'}$, the missing eddy potential energy being provided by the release of latent heat of condensation.

Although this first part gives results in the desired direction, both the growth rate and the structure of the eigensolutions do not compare favourably with the observed cases of explosive marine cyclones. As we mentioned in the Introduction some of the observed features may however be due to non-modal growth while we are only studying the normal modes. In Chapter 3 we included a representation of heat and moisture fluxes at the lower boundary in the models of the previous chapter. A heating term proportional to the meridional velocity of the perturbation and to an air-sea entropy difference (a linearization of a drag law for equivalent potential temperature) was added to the thermodynamic equation of the 2-level SG model, in the updraft region only, having assumed that only there can latent heat flux from the lower boundary be realized as sensible heat input aloft. The most unstable modes thus found have a growth rate that increases almost linearly with the air-sea temperature difference. The numerical simulations, performed with the model of section 2.3 with fluxes of

heat in the form of drag laws for potential temperature and moisture, confirm this result, in addition to a retrograde phase speed with respect to the mid-level base wind, and to a warm-core thermal structure, which is very narrow at the beginning of the phase of 'explosive' growth and becomes broader later on. The evolution occurs in two distinct phases - in the first one the heat from the bottom boundary accumulates in the lowest levels, the deepening of the low-pressure center and the growth rate of kinetic energy are modestly increased, but the differences with the no-flux simulations are confined to the low levels. In a second stage heat is efficiently transported upward in the updraft region, a narrow warm core develops, with a hurricane-like circulation superimposed on the moist baroclinic wave, the growth rate of perturbation kinetic energy reaches peak values two to three times higher than in the no-flux experiments and the deepening rate of the central surface pressure is above the conventional threshold for explosive cyclones. When compared with the numerical simulations we observe that the two-level model qualitatively reproduces the increase in growth-rate in the 'explosive' phase of growth but it misses the 'shallow' early phase because of poor vertical resolution. Moreover, a complex vertical structure is created by the more realistic model in order to transport heat upward, while in the two-level heat was applied directly at mid-level. The models also give conflicting results as to the phase speed of the explosive cyclones, that appear to be faster than the mean wind in the two-level and slower than the mean wind in the numerical model. The observations of real cases leave uncertainties on this point so we cannot decide which model

performs better from this point of view. The limitations of both models (especially with regard to the linearized saturation law used in the numerical simulations) have been discussed in the appropriate sections. The deepening rate of the pressure perturbation increases almost linearly with the air-sea temperature difference, and it must be kept in mind that the same entropy flux can be achieved with smaller temperature differences if the air in contact with the ocean surface is not saturated, as seems to be the case, so that a larger latent heat flux can take place.

Our goal at the outset had been to provide a plausible mechanism for maritime explosive developments by studying non-adiabatic influences on baroclinic instability. Specifically, Roebber's (1984) study seems to indicate that the distribution of deepening rates of mid-latitude cyclones is biased toward the strongest events, suggesting that a distinct physical mechanism is active. The results of Chapter 2 show features that are commonly observed in land cyclones as well and therefore do not offer the means to discriminate between ordinary and explosive developments in the way implied by climatological studies. They are relevant for the description of baroclinic development anywhere moisture is present, presumably with more or less enhanced features depending on the relative humidity, and they offer some improvement over those earlier studies mentioned in the Introduction that do not consider the ability of the marine environment to provide a sustained source of moist entropy. It is likely that 'moist' events are more frequent over sea and 'dry' events over land, but when land

and sea cyclones are considered together there is no 'a priori' reason to expect a non-gaussian distribution of events from this mechanism. On the other hand the experiments of Chapter 3, in addition to a better adherence to the observed behavior of explosive cyclones, seem to suggest that only those events that reach above a 'threshold' of amplitude (or growth rate) are further enhanced by the effect of heat fluxes from the ocean. It is then conceivable that the deviations from a normal distribution, if they are confirmed by studies of more extensive samples of events, are caused by the activation of this 'feedback' mechanism in those disturbances that are already the strongest beforehand.

We have only been studying this problem from the 'normal mode' point of view, and the common assumption in this regard is that if the development lasts long enough the most unstable normal mode will be observed, after the transients are dissipated away. Recently however the work by Farrell,1982, 1984,1985 has shown that the 'non-modal' initial growth may be more important than previously thought. In this model, specifically, the suggested presence of an amplitude threshold makes it possible that a favorable initial condition (as well as any of the observed features that we have ignored, like the interaction with a pre-existing trough in the upper level flow) may help the perturbation reach sooner the stage, or the organization, in which it can efficiently use the energy provided by the heat fluxes at the lower boundary.

In addition to the previously discussed linearized saturation law, at least one other problem related to the two-dimensionality of the model appears in the results - the onset of the explosive phase is related to a 'hurricane' type of organization, and while 2-D baroclinic waves are qualitatively similar to waves of finite meridional extent, we know that the natural structure of hurricanes is axisymmetric, so that the 3rd dimension, in a cartesian space, is as important as the other two. Whether or not the addition of a 3rd dimension would significantly alter our conclusion that the most distinguishing features of mid-latitude explosive cyclones are due to air-sea exchange of latent and sensible heat transported upward by convective activity cannot be determined at this point, and only a 3-D model can answer the question. The presence of a 'hurricane' phase at the beginning of the exposive growth in real cases could however be detected by observation, since its duration is, in the model, of the order of 20. hours.

BIBLIOGRAPHY

Anthes.R.A.,Y.-H. Kuo and J.R.Gyakum,1983 - Numerical simulations of a case of explosive marine cyclogenesis. Mon.Wea.Rev.,111,1174-1188

Aubert,E.J.,1957 - On the release of latent heat as a factor in large-scale atmospheric motions. J.Meteor.,14,527-542

Bennetts,D.A. and B.J.Hoskins,1979 - Conditional symmetric instability - a possible explanation for frontal rainbands. Quart.J.Roy.Meteor.Soc,105, 945-962

Bjerknes,J.,1919 - On the structure of moving cyclones. Geofys.Publ.,1,1-8

Blumen,W.,1979 - On short wave baroclinic instability. J.Atmos.Sci.,37, 1925-1933

Bosart,L.F.,1981 - The President's Day snowstorm of 18-19 February 1979: a subsynoptic-scale event. Mon.Wea.Rev.,109,1542-1566

Chang,C.B.,D.J.Perkey and W.-D.Chen,1987 - Observed dynamic structure of an intense oceanic cyclone. Mon.Wea.Rev.,115,1127-1139

Charney,J.G.,1947 - The dynamics of long waves in a baroclinic westerly current. J.Meteor.,2,136-163

Charney,J.G. and A.Eliassen,1964 - On the growth of the hurricane depression. J.Atmos.Sci.,21,68-75

Danard,M.B.,1964 - On the influence of released latent heat on cyclone development. J.Appl.Meteor.,3,27-37

Davis,C.A. and K.A.Emanuel,1988 - Observational evidence for the influence of surface heat fluxes on maritime cyclogenesis. Submitted to Mon.Wea.Rev.

Eady,E.T.,1949 - Long waves and cyclone waves. Tellus,1,33-52

Emanuel,K.A.,1985 - Frontal circulation in the presence of small moist symmetric stability. J.Atmos.Sci,42,1062-1071

Emanuel,K.A.,1986 - An air-sea interaction theory for tropical cyclones. Part I: Steady-state maintenance. J.Atmos.Sci,43,585-604

Emanuel,K.A.,1988 - Observational evidence of slantwise convective adjustment. Submitted to Mon.Wea.Rev.

Emanuel,K.A.,M.Fantini and A.J.Thorpe,1987 - Baroclinic instability in an environment of small stability to slantwise moist convection. Part I: Two-dimensional models. J.Atmos.Sci., 44, 1559-1573

Farrell,B.F.,1982 - The initial growth of disturbances in a baroclinic flow. J.Atmos.Sci., 39, 1663-1686

Farrell,B.F.,1984 - Modal and nonmodal baroclinic waves. J.Atmos.Sci., 41, 668-673

Farrell,B.F.,1985 - Transient growth of damped baroclinic waves. J.Atmos.Sci., 42, 2718-2727

Gall,R.L.,1976 - The effect of released latent heat in growing baroclinic waves. J.Atmos.Sci,33,1686-1701

Green,J.S.A.,1960 - A problem in baroclinic stability. Quart.J.Roy.Meteor.Soc., 86,237-251

Gyakum,J.R.,1983 - On the evolution of the QEII storm. I: synoptic aspects. Mon.Wea.Rev.,111,1137-1155

Gyakum,J.R.,1983b - On the evolution of the QEII storm. II: dynamic and thermodynamic structure. Mon.Wea.Rev.,111,1156,1173

Harrold,T.W. and K.A.Browning,1969 - The polar low as a baroclinic disturbance. Quart.J.Roy.Meteor.Soc.,95,710-723

Hoskins,B.J.,1975 - The geostrophic momentum approximation and the semi-geostrophic equations. J.Atmos.Sci.,32,233-242

Hyun,J.M.,1981 - Separate and combined effects of static stability and shear variation on the baroclinic instability of a two-layer current. J.Atmos.Sci,38, 322-333

Jacobs,W.C.,1942 - On the energy exchange between sea and atmosphere. J.Mar.Res.,5,37-66

Keiser,D. and R.A.Anthes,1982 - The influence of planetary boundary layer physics on frontal structure in the Hoskins - Bretherton horizontal shear model. J.Atmos.Sci., 39, 1783-1802

Klemp,J.B. and R.B.Wilhelmson,1978 - The simulation of three-dimensional convective storm dynamics. J.Atmos.Sci.,35,1070-1096

Lilly,D.K.,1960 - On the theory of disturbances in a conditionally unstable atmosphere. Mon.Wea.Rev.,88,1-17

Liou,C.-S. and R.L.Elsberry,1987 - Heat budget analyses and forecasts of an explosively deepening maritime cyclone. Mon.Wea.Rev.,115,1809-1824

Mak,M.K.,1982 - On moist quasi-geostrophic baroclinic instability. J.Atmos.Sci.,39,2028-2037

Malkus,J.S.,1962 - Large scale interactions. The Sea, ch.4. John Wiley and Sons

Manabe,S.,1956 - On the contribution of heat released by condensation to the change in pressure pattern. J.Meteor.Soc.Japan,34,12-24

Manabe,S.,J.Smagorinsky and R.F.Strickler,1965 - Simulated climatology of a general circulation model with a hydrological cycle. Mon.Wea.Rev.,93, 769-798

Mansfield,D.A.,1974 - Polar Lows: the development of baroclinic disturbances in cold air outbreaks. Quart.J.Roy.Meteor.Soc.,100,541-554

Mason,P.J. and R.I.Sykes,1982 - A two dimensional numerical study of horizontal roll vortices in an inversion capped planetary boundary layer. Quart.J.Roy.Meteor.Soc.,108,801-823

Matsumoto,S.,S.Yoshizumi and M.Takeuchi,1970 - On the structure of the 'Baiu front' and the associated intermediate-scale disturbances in the lower atmosphere. J.Meteor.Soc.Japan,48,479-491

McWilliams,J.C. and P.R.Gent,1980 - Intermediate models of planetary circulations in the atmosphere and ocean. J.Atmos.Sci.,37,1657-1678

Nehrkorn,T.,1985 - Wave-CISK in a baroclinic basic state. Ph.D. dissertation. Massachusetts Institute of Technology

Nitta,T.,1964 - On the development of relatively small scale cyclone due to the release of latent heat by condensation. J.Meteor.Soc.Japan,42,260-267

Nitta,T. and Y.Ogura,1972 - Numerical simulation of the development of the intermediate-scale cyclone in a moist model atmosphere - J.Atmos.Sci,29, 1011-1024

Ooyama,K.,1969 - Numerical simulation of the life cycle of tropical cyclones. J.Atmos.Sci.,26,3-40

Orlansky,I.,1968 - Instability of frontal waves. J.Atmos.Sci., 25, 178-200

Orlansky,I.,1986 - Localised baroclinicity: a source for meso-alpha cyclones. J.Atmos.Sci., 43, 2857-2885

Pedlosky,J.,1964 - The stability of currents in the atmosphere and ocean: Part I. J.Atmos.Sci.,21,201-219

Pedlosky,J.,1979 - Geophysical Fluid Dynamics. Springer Verlag

Pettersen,S.,D.L.Bradbury and K.Pedersen,1962 - The Norwegian cyclone models in relation to heat and cold sources. Geofys.Publ.,24,243-280

Pettersen,S. and S.Smebye,1971 - On the development of extratropical cyclones. Quart.J.Roy.Meteor.Soc., 97, 457-482

Phillips,N.A.,1951 - A simple three-dimensional model for the study of large-scale extratropical flow patterns. J.Meteor.,8,381-394

Pyke,C.B.,1965 - On the role of air-sea interaction in the development of cyclones. Bull.Amer.Meteor.Soc.,46,4-15

Rasmussen,E.,1979 - The polar low as an extratropical CISK disturbance. Quart.J.Roy.Meteor.Soc.,105,531-550

Rasmussen,E. and M.Lystad,1987 - The Norwegian Polar Low project: a summary of the international conference on Polar Lows, 20-23 May 1986, Oslo, Norway. Bull.Amer.Meteor.Soc.,68,810-816

Reed,R.J.,1979 - Cyclogenesis in polar air streams. Mon.Wea.Rev.,107,38-52

Reed,R.J. and M.D.Albright,1986 - A case study of explosive cyclogenesis in the Eastern Pacific. Mon.Wea.Rev.,114,2297-2319

Roebber,P.J.,1984 - Statistical analysis and updated climatology of explosive cyclones. Mon.Wea.Rev.,112,1577-1589

Rotunno,R. and K.A.Emanuel,1987 - An air-sea interaction theory for tropical cyclones. Part II: Evolutionary study using a nonhydrostatic axisymmetric numerical model. J.Atmos.Sci.,44,542-561

Rotunno,R, and J.Klemp,1985 - On the rotation and propagation of simulated supercell thunderstorms. J.Atmos.Sci, 42, 271-292

Sanders,F.,1986 - Explosive cyclogenesis in the west-central North Atlantic Ocean 1981-1984. Part I: composite structure and mean behavior. Mon.Wea.Rev., 114,1781-1794

Sanders,F. and J.R.Gyakum,1980 - Synoptic-dynamic climatology of the 'bomb'. Mon.Wea.Rev.,108,1589-1606

Sardie,J.M. and T.T.Warner,1983 - On the mechanism for the development of polar lows. J.Atmos.Sci.,40,869-881

Satyamurty,P., V.B.Rao and A.D.Moura,1982 - Subsynoptic-scale baroclinic instability. J.Atmos.Sci.,39,1052-1061

Smagorinsky,J.,1956 - On the inclusion of moist adiabatic processes in numerical prediction models. Bericht des Deutchen Wetterdienst,38,82-90

Soong,S.-T. and Y.Ogura,1972 - Numerical simulation of warm rain development in an axisymmetric cloud model. J.Atmos.Sci.,31,1262-1285

Staley,D.O. and R.L.Gall,1977 - On the wavelength of maximum baroclinic instability. J.Atmos.Sci.,34,1679-1688

Stone,P.H.,1966 - On non-geostrophic baroclinic stability. J.Atmos.Sci., 23, 390-400

Stone,P.H.,1972 - Comments on 'Ageostrophic effects on baroclinic instability'. J.Atmos.Sci.,29,986-987

Tang,C.-M. and G.H.Fichtl,1983 - The role of latent heat release in baroclinic waves - without beta-effect. J.Atmos.Sci.,40,53-72

Thorpe,A.J. and K.A.Emanuel,1985 - Frontogenesis in the presence of small stability to slantwise convection. J.Atmos.Sci,42,1809-1824

Tokioka,T.,1970 - Non-geostrophic and non-hydrostatic stability of a baroclinic fluid. J.Meteor.Soc.Japan,48,503-520

Tracton,M.S.,1973 - The role of cumulus convection in the development of extratropical cyclones. Mon.Wea.Rev.,101,573-593

Wang,B. and A.Barcilon,1986 - Moist stability of a baroclinic zonal flow with conditionally unstable staratification. J.Atmos.Sci.,43,705-719

Wash,C.H.,J.E.Peak,W.E.Calland and W.A.Cook,1988 - Diagnostic study of explosive cyclogenesis during FGGE - Mon.Wea.Rev.,116,431-451

Weng,H.Y. and A.Barcilon,1987 - Favorable environments for explosive cyclogenesis in a modified two-layer Eady model. Tellus,39A,202-214

Winston,J.S.,1955 - Physical aspects of rapid cyclogenesis in the Gulf of Alaska. Tellus,7,481-500

LIST OF FIGURES

Fig.2.1 - Structure of the 2-level model and levels where variables are defined ...pag.31

Fig.2.2 - Subdivision of the model in a 'moist' and a 'dry' region. Horizontal coordinate X is defined separately in each region. Soutions are matched at points A=B and C ...pag.31

Fig.2.3 - Growth rate σ versus half-width of the downdraft L_2 for different values of r; r=1 is the dry model; r=0 is obtained asymptotically and confirmed numerically for $r \sim 10^{-6}$ ...pag.42

Fig.2.4 - As 2.3 but σ vs. total wavelength $L_{TOT} = 2L_2(1+\lambda)$; dashed lines join points of constant L_2, i.e. points that lay on vertical lines in fig.2.3, thus showing the reduction of total wavelength due to the narrow updraft ...pag.43

Fig.2.5 - Top: Dimensionless $w^* \equiv \psi_x$ and θ as function of the geostrophic coordinate X, for the most rapidly growing mode when r=0.08. Bottom: same but for meridional velocity v and modified geopotential $\phi \equiv p'/\rho_0 + v^2/2$ at upper and lower level ...pag.48

Fig.2.6 - Same as 2.5 but in physical space when the maximum low-level vorticity is $10 f_0$ ...pag.49

Fig.2.7 - Contours of constant σ on the r - Ro plane for fixed L2 = 1.8 ...pag.60

Fig 2.8 a) - Growth rate σ (solid) and ratio of updraft to downdraft width λ (dashed) for various values of Ro at fixed r = 0. Ro = 0 is the GM approximation ...pag.61

Fig.2.8 b) - same as a) but for r = .1 ...pag.62

Fig.2.9 - Domain and arrangement of dependent variables on the staggered grid covering the domain. All the thermodynamic variables are located at v points (adapted from Rotunno and Emanuel,1987) ...pag.78

Fig.2.10 - u,v,w, θ, θ' ,p' fields for exp. A0 at times 100,150,170,180, 190,200 hrs. Note that contour spacing is not the same for perturbation fields at different times ...pag.79

Fig.2.11 - Growth rate σ vs. time for exp. A0 and for the two-level analytic models with the same parameters as A0 ...pag.81

Fig.2.12 - v and w fields for exp. A1 from 10 to 50 hrs ...pag.82

Fig.2.13 - same as 2.11 but for exp. A1 ...pag.83

Fig.2.14 - same as 2.10 but for exp. A1 from 100 to 150 hrs ...pag.84

Fig.2.15 - q_v', rh, θ_e, M, q_d', q_e for exp. A1 at 100 and 150 hrs ...pag.86

Fig.2.16 - same as 2.11 but for exp. A2 ...pag.87

Fig.2.17 - same as 2.10 but for exp. A2 from 280 to 300 hrs ...pag.88

Fig.2.18 - Growth rate σ vs. time for exp.s A1 and A3 ...pag.89

Fig.2.19 - same as 2.10 but for exp. A3 from 130 to 150 hrs ...pag.90

Fig.2.20 - same as 2.11 but for exp. B ...pag.91

Fig 2.21 - same as 2.11 but for exp. C ...pag.92

Fig.2.22 - same as 2.12 but for exp. C at 160,180,200 hrs ...pag.93

Fig.2.23 - Growth rate σ vs. time for exp.s D,E,F and for the two-level PE analytic model with the same parameters ...pag.94

Fig.2.24 - same as 2.11 but for exp. H ...pag.95

Fig.2.25 - same as 2.12 but for exp. G at 20 and 50 hrs ...pag.96

Fig.2.26 - same as 2.12 but for exp. H at 20,50 and 100 hrs ...pag.97

Fig.3.1 - Eigenvalues σ, λ, u_0 of the SG 2-level model with heat flux from the lower boundary vs. heating parameter Γ_0 for r=.1, L2=1.8. Solid:most unstable $\delta_A = \delta_C = 0$, dashed: least unstable $\delta_A = \delta_C = 1$ pag.115

Fig.3.2 - Eigenvalues σ, λ, u_0 vs. L2 for various values of the heating parameter Γ_0 for the most unstable case $\delta_A = \delta_C = 0$ (see text). Solid: growth rate σ ; long dash: ratio of the width of the updraft to downdraft λ ; short dash: relative phase speed u_0. ...pag.116

Fig.3.3 - Form of the eigensolution for L2=1.8, r=.1, Γ_0 =2., $\delta_A = \delta_C = 0$. Eigenvalues for this mode are σ =1.5, λ =.17, u_0=.23. Pressure is known only from it derivative v, so that an arbitrary constant can be added to both p1 and p2. ...pag.117

Fig.3.4 - Contours of constant growth rate σ for L2=1.8, $\delta_A = \delta_C = 0$, on the Γ_0 ,r plane. ...pag.118

Fig.3.5 - growth rate σ vs. time for exp. I ...pag.129

Fig.3.6 - same as fig.3.5 but for exp. FI2 ...pag.130

Fig.3.7 - u,v,w, θ, θ' ,p' fields for exp.I, shown every 10. hours from 50. hrs to 130. hrs. Contour interval is not constant with time. ...pag.131

Fig.3.8 - same as fig.3.7 but for exp. FI2 ...pag.134

Fig.3.9 - equivalent potential temperature θ_e and perturbation potential vorticity q_d' for exp. FI2 at 100. hrs and 130. hrs ...pag.137

Fig.3.10 - difference in meridional wind field v between exp. FI2 and exp. I at 90,100,110 hrs. The graph shows FI2 minus I ...pag.138

Fig.3.11 - Location of the two 0.m/s isotach of meridional wind, at the lowest resolved level (500. m height), for exp. FI2, versus time, showing the westward displacement of the disturbance in the frame of reference in which the zonal basic wind is zero at mid-level ...pag.139

Fig.3.12 - growth rate σ vs. time for exp.s I,FI2,FI3,FI4 ...pag.140

Fig.3.13 - minimum surface pressure vs. time for exp.s I (C_e=0), FI0 ($\overline{\Delta\vartheta}$=0 K), FI1,FI2,FI3,FI4 ...pag.141

Fig.3.14a - relative humidity, equivalent potential vorticity q_e and buoyancy for saturated vertical motions $B_{sat}=\left(\vartheta_z+\frac{L}{c_p\bar{\pi}}q^{sat}_{v_z}\right)\frac{g}{\vartheta_{z0}}$, for exp. I at 60.,90.,100. hrs ...pag.142

Fig.3.14b - same as a) but for exp. FI2 ...pag.143

Fig.3.15 - same as fig.3.12 but for exp.s L,FL1,FL2,FL3 ...pag.144

Fig.3.16 - same as fig.3.13 but for exp.s L,FL1,FL2,FL3 ...pag.145

Fig.3.17 - same as fig.3.7 but for exp. FL2 between 30 hrs and 130. hrs ..pag.146

Fig 3.18 - minimum surface pressure vs. time for experiments similar to FI2 but with varying horizontal length of the domain. Exp. FI2 has a 3000 Km wavelength ...pag.150

LIST OF TABLES

Table 2.1 - comparision of exact and approximate eigenvalues of the 2-level SG model ...pag.41

Table 2.2 - eigenvalues of 2L PE model for various r and Ro ...pag.55

Table 2.3 - cut-off L2 for various Ro in the 2L PE model ...pag.57

Table 2.4 - total wavelength of eigensolutions of 2L PE model for various Ro ...pag.59

Table 2.5 - base state thermodynamic variables for exp. A1 ...pag.75

Table 2.6 - parameters of the numerical model ...pag.76

Table 2.7 - summary of experiments presented in sect.2.3 ...pag.77

Table 3.1 - summary of experiments presented in sect.3.2 ...pag.128

E non pur io qui piango bolognese:
anzi n'e' questo loco tanto pieno
che tante lingue non son ora apprese
a dicer millibar tra Savena e Reno

adapted from: Inferno,XVIII,58-61